

***In Vivo* Characterization of RIF-1 Tumors *via* Diffusion and Fluorine-19 NMR Methods**

by

Michael Rudolf Meiler

A Dissertation
Submitted to the faculty
of the

WORCESTER POLYTECHNIC INSTITUTE
in partial fulfillment of the requirements for the
Degree of Doctor of Philosophy
in
Biomedical Engineering

June 1999

Approved:

Karl G. Helmer, Ph.D.
Research Assistant Professor, Major Advisor
Biomedical Engineering Department
Worcester Polytechnic Institute

Christopher H. Sotak, Ph.D.
Professor, Co-Advisor
Biomedical Engineering Department
Worcester Polytechnic Institute

Robert A. Peura, Ph.D.
Professor and Head
Biomedical Engineering Department
Worcester Polytechnic Institute

T. J. Fitzgerald, M.D.
Oncologist
The University of Massachusetts - Memorial
Cancer Center

Acknowledgements

Looking back on the time spent to accumulate the knowledge presented in this dissertation, there have been many people who contributed directly or indirectly to this work. To all of them, named or unnamed, I like to express my gratitude and deepest appreciation.

First I like to thank my advisor, mentor and colleague Dr. Karl Helmer, who shaped my career as a scientist and taught me my first steps in nuclear magnetic resonance. He has been a constant source of advice and inspiration. The many discussions we had concerning experiments deepened my knowledge of the subject and shaped many aspects of my academic life.

I wish to thank Professor Christopher Sotak, who was my co-advisor and an integral part in shaping of my scientific career. He provided an environment in which I was free to explore my ideas. His thorough scientific approach and his knowledge have been an endless source of encouragement.

I would like to thank Turgut Tatlisumak, for his friendship and advice. He has taught me the higher art of animal surgery and care and was a constant source of medical knowledge and encouragement.

I would like to thank Fuhai Li, for his friendship and the contributions he had made to my research. He had brought endless medical expertise and enthusiasm to our joint experiments.

I would like to thank, Ken Takano, Katsumi Irie, Züluf Onal, Wolf Schäbitz and Tsuyoshi Omae, for their friendship and medical advice.

I like to thank Rick Carano, Sam Han, Matt Silva, Jeremy Wellen, Mark Kazemi, Orna Mayzel-Oreg and Alica Briggs for their friendship, technical advice and their contribution for making the NMR group an enjoyable place to work.

I would like to thank Dr T. J. Fitzgerald for finding the time to serve on the graduation committee and for insights into cancer therapy.

I would like to thank Professor Robert Peura for his guidance during my graduate years at WPI.

I would like to thank Gail Boulienne of the University of Massachusetts Medical Center for her excellent H&E staining and Professor David S. Adams of the Biology and Biotechnology Department at WPI, for the use of his imaging system to digitize the tumor histological sections.

Finally, I would like to thank my family for their love and support during all my endeavors. Anything I have accomplished is due to them and their support, which I will never be able to repay.

Most especially, I would like to thank my wife, Yolanda Meiler, for her unlimited love, encouragement, support and the many hardships she had to endure for me during the completion of this work, as well as my now eight month old baby-daughter, Ilse Meiler, who gave me some time to write this dissertation while I was caring for her.

Preface

This dissertation is the product of the efforts to characterize radiation induced fibrosarcoma (RIF-1) tumors via diffusion and fluorine-19 (^{19}F) nuclear magnetic resonance *in vivo*.

The first stage of experiments concentrated on the spectroscopic characterization of water diffusion in RIF-1 tumors. New theories developed to understand the diffusion behavior of water molecules in porous media were applied to water diffusion in solid tumors. Studies conducted by my predecessors verified the theory in model systems such as rocks and glass beads. Later, slight modifications were undertaken to account for differences between porous media and biological systems. The validity of the application in biological systems was then tested on red blood cells and murine tumors.

The studies in this dissertation are a continuation of their efforts and the application of these tools to characterize RIF-1 tumors *in vivo*. Chapter 3 shows that the return-to-the-origin (RTO) probability and the apparent diffusion coefficient (ADC), as measured by diffusion-weighted magnetic resonance spectroscopy, are sensitive to structural changes as induced by the development of tumor necrosis. Since spectroscopic measurements do not provide spatial information of these changes, diffusion-weighted magnetic resonance imaging was employed to measure the RTO probability and the ADC on a pixel-by-pixel basis (Chapter 4). Several technical problems needed to be overcome. For example, with imaging the signal-to-noise ratio was reduced due to fewer spins being interrogated in the

imaging slice and the lengthened echo time (TE) needed to accommodate the imaging acquisition time. Several adjustments to the imaging procedure were necessary and needed to be verified.

The imaging experiment showed the ability of both the apparent diffusion coefficient (ADC) and RTO to detect necrotic tumor tissue. In spite of differences in slice thickness between magnetic resonance imaging (MRI) and histological analysis, regions of histologically-defined necrosis were spatially correlated with specific regions of the ADC and RTO maps. The study suggested that the ADC and RTO could be used to monitor tumor structural changes in response to chemo- or radiation therapy.

Chapter 5 deals with the effects of changing the diffusion gradient duration in diffusion-weighted magnetic resonance imaging on the measured ADC. Most of the clinical systems have limited diffusion gradient strength and compensate for it by lengthening the diffusion gradient duration and with it the MRI echo-time. This increase in gradient duration is a direct violation of the " δ -function pulse width criterion" in which the diffusion gradient pulse width is much smaller than the diffusion gradient separation and causes the resulting measurement to be similar to the constant-gradient variant of the diffusion experiment. With significant diffusion occurring during the long diffusion-gradient pulse, we investigated the extent to which the measured diffusion coefficient is altered by working in the constant-gradient regime rather than the δ -function regime.

Chapter 6 deals with the assessment of tumor oxygen status in RIF-1 tumors during treatment using the perfluorocarbon (PFC) perfluoro-15-crown-5-ether. Experiments conducted by my predecessors produced promising results, but required a large imaging slice thickness. Since changes in oxygen tension during therapy were expected to occur on cellular level, the imaging slice thickness had to be reduced as much as possible. The injection procedure was modified to increase the concentration of PFC within the tumor and modifications to the NMR pulse sequence allowed the imaging slice thickness to be reduced to a value that provided acceptable spatial resolution. The second problem was the clearance of the PFC from the tumor during therapeutic intervention. Multiple PFC injections allowed the tumor oxygen status to be monitored after chemotherapy administration.

Abstract

Diffusion-weighted nuclear magnetic resonance has gained widespread use in the characterization of various diseases. Developments in the area of porous media theory have been successfully transferred and adapted for the use in biological tissue. Measurement of the displacement of diffusing water molecules can reveal structural information about the environment in which the molecules translate. The return-to-the-origin (RTO) probability and the apparent diffusion coefficient (ADC) are based on the diffusion behavior of water molecules in a restricted environment. Water molecules in restricted space have smaller displacements, for a given diffusion time, than water molecules diffusing in bulk solution.

The cell membranes and organelles in healthy biological tissue impart more restrictions on diffusing water molecules as compared to necrotic tumor tissue. In necrotic tissue the degradation of cellular structures by auto- and/or heterolysis allows water molecules to diffuse over larger distances without encountering restrictions. The spectroscopic measurement of the RTO probability and the RTO enhancement in RIF-1 tumors showed that the RTO probability is sensitive to these changes in structure. The study showed that smaller tumors, which are less necrotic, have a larger RTO probability and enhancement than larger RIF-1 tumors with a higher fraction of necrotic tumor tissue.

Extension of the methodology to NMR imaging was used to answer the question if the RTO probability can provide spatial information about the necrotic area within RIF-1

tumors. The necrotic area measured by the ADC and histology were compared. While neither ADC or RTO could show its superiority over the other, both methods showed a good correlation between their mean values and the necrotic area fraction as measured by histology. The mean ADC and the mean RTO enhancement had a correlation with the necrotic tumor fraction, as determined by histology, of $r = 0.86$ and $r = -0.82$, respectively. Conventional T₂-weighted images of the same tumor slice showed a poorer correlation ($r = 0.62$) with the necrotic fraction and no visual agreement with the histology. The general features of the ADC and RTO enhancement were in agreement with histology, however, more exact comparisons were not possible due to the large differences in slice thickness between the two techniques.

Structural changes similar to those caused by tumor tissue necrosis can be induced by chemo- and radiation therapy and ADC and RTO enhancement were used to monitor these changes non-invasively. RIF-1 tumors were grown on the hind leg of C3H mice and monitored daily by diffusion-weighted MRI. ADC and RTO-enhancement maps were created using data acquired from control animals and animals treated with 100 mg/kg 5-Fluorouracil. Both ADC and RTO proved to be useful in the early detection of the efficacy of treatment as well as for monitoring the progress of therapy.

Diffusion measurements by pulsed-field-gradient (PFG) MRI have become an important tool for detecting of pathophysiological changes caused by cancer and stroke. The increasing popularity of diffusion measurements has initiated their use on clinical MRI systems that have limited magnetic-field-gradient strength. These limitations make it

necessary to lengthen the diffusion-gradient duration to ensure sufficient signal attenuation for calculating the ADC. Unfortunately, increasing of the diffusion-gradient duration to a large extent violates the theoretical model used in the ADC calculation. The diffusion measurements are not performed in the finite pulse width regime, but rather in the constant gradient regime, requiring a different interpretation of the results. Examination of the differences in the measured diffusion coefficient showed that increasing both the diffusion-gradient duration and the echo time have a significant impact on the results of a diffusion measurement.

A different way to assess changes in RIF-1 tumors as a function of treatment is the measurement of the tissue oxygen status. Cell hypoxia has long been linked with treatment resistivity and reoccurrence in cancers, where the oxygen status is a determining factor of treatment outcome. Perfluorocarbons (PFC's) have been used successfully to assess the tumor oxygen status in the past, but required a large MRI slice thickness due to compensate for the low PFC concentration. The tissue oxygen status of the tumor is assessed by intravenous injection of a PFC that is subsequently sequestered in the tumor. The measurement of the T_1 -relaxation time of the PFC allows the calculation of the oxygen content, which is linearly related to the relaxivity and the temperature. Fluorine-19, multiple-slice, inversion-recovery echo-planar imaging (EPI) allowed high spatial resolution assessment of the tissue oxygen status over the entire tumor. The results demonstrated that there is a large variation in tissue oxygenation between adjacent slices. Comparison of the oxygen distribution between various tumors

also showed that there is no common pattern in the spatial distribution of oxygen within the tumor.

Monitoring of the oxygen status during chemotherapy showed an increase in hypoxic tissue and a reduction in tumor size in response to the toxicity of the chemotherapeutic agent. As the effects of the treatment subsided, rapid cell proliferation caused the tumor to regrow and a subsequent decrease in tissue oxygen tension was observed. The study clearly demonstrated the changes in oxygen tension in response to chemotherapy and the need for multi-slice MRI acquisition at high spatial resolution to detect these changes.

Table of Contents

Acknowledgments	i
Preface	iv
Abstract	vii
Table of Contents	xi
List of Figures	xiv
List of Tables	xvii
1. Nuclear Magnetic Resonance Theory	1
1.0 Nuclear Magnetic Resonance Theory.....	2
1.1 The Magnetic Field.....	3
1.2 Physical Principles.....	5
1.2.1 Properties of the Spin.....	5
1.2.2 The Nuclear Angular Momentum.....	6
1.2.3 The Nuclear Magnetic Dipole Moment.....	8
1.2.4 The Nuclei in a Magnetic Field.....	9
1.2.5 Bulk Magnetization.....	12
1.3 Radio Frequency Pulses and The Rotating Frame of Reference.....	15
1.4 Nuclear Relaxation.....	20
1.4.1 T_1 Relaxation (Longitudinal or Spin-Lattice Relaxation).....	21
1.4.2 T_2 Relaxation (Transverse or Spin-Spin Relaxation).....	22
1.5 The Free-Induction Decay.....	24
1.6 Fourier Transformation.....	25
2. Spin Manipulation	31
2.0 Spin Manipulation.....	32
2.1 T_1 Measurement.....	32
2.2 T_2 Measurement.....	35
2.3 Molecular Diffusion.....	38
2.3.1 Diffusion Theory.....	38

2.3.2	Stejskal-Tanner Diffusion Measurement	41
2.3.3	Diffusion-Weighted Stimulated-Echo	45
2.4	Magnetic Resonance Imaging	47
2.4.1	Frequency Encoding	47
2.4.2	Phase Encoding	49
2.4.3	Slice Selection	50
2.4.4	<i>k</i> -Space and Imaging	54
2.4.4.1	Spin-Echo Imaging	56
2.4.4.2	Echo-Planar Imaging	59
3.	The Return-to-the-Origin Probability and the ADC of Water as Indicators of RIF-1 Tumor Necrosis	61
3.0	The Return-to-the-Origin Probability and the ADC of Water as Indicators of RIF-1 Tumor Necrosis	62
3.1	Introduction	62
3.2	Experimental Methods	82
3.2.1	Animal Preparation	82
3.2.2	NMR Measurements	84
3.2.3	Histology	86
3.2.4	Data Analysis	87
3.3	Results	89
3.4	Discussion and Conclusion	101
4.	Return-to-the-Origin Probability and ADC Mapping of Water as Early Indicators of the Efficacy of Chemotherapy in RIF-1 Tumors	111
4.0	Return-to-the-Origin Probability and ADC Mapping of Water as Early Indicators of the Efficacy of Chemotherapy in RIF-1 Tumors	112
4.1	Introduction	113
4.2	Experimental Methods	115
4.2.1	Animal Preparation	115
4.2.2	Chemotherapy	115
4.2.3	Dose Response Study	116
4.2.4	NMR Measurements	116
4.2.5	Data Analysis	118
4.3	Results	121
4.4	Discussion and Conclusion	135

5.	The Diffusion Coefficient Measurement as a Function of the Diffusion Gradient Duration	144
5.0	The Diffusion Coefficient Measurement as a Function of the Diffusion Gradient Duration	145
5.1	Introduction	146
5.2	Experimental Methods	154
5.2.1	Animal preparation	154
5.2.2	NMR measurements	155
5.2.3	Data Analysis	158
5.3	Results	159
5.4	Discussion and Conclusion	165
6.	Murine Tumor Oxygen Mapping	168
6.0	Murine Tumor Oxygen Mapping	169
6.1	Introduction	169
6.2	Experimental Methods	173
6.2.1	Animal Preparation	173
6.2.2	Experimental Protocol	174
6.2.3	NMR Measurements	175
6.2.4	Data Analysis	176
6.3	Results	178
6.4	Discussion & Conclusion	185
7.	Summary	189
8.	Bibliography	194
9.	Appendix	207
9.0	Curriculum Vitae	208

List of Figures

Chapter 1

1.2.1.1	Model of the nuclear magnetic moment	5
1.2.2.1	Angular momentum of a spin- $\frac{1}{2}$ system	7
1.2.4.1	Interaction between the magnetic field and the nuclear dipole moment	9
1.2.5.1	Random orientation of individual nuclear magnetic moments in the absence of a magnetic field	12
1.2.5.2	Precession of nuclei about the magnetic field	12
1.2.5.3	Distribution of magnetic moments between energy states	13
1.2.5.4	Sum of net magnetization	15
1.3.1	Components of the net magnetization vector, M	16
1.3.2	Effective magnetization vector	17
1.3.3	Rotating frame of reference	19
1.4.1.1	Distribution of spin population at equilibrium and after RF excitation	21
1.5.1	Free induction decay (FID) and its decay envelope	24
1.6.1	Single-frequency sine-wave and its Fourier transform	26
1.6.2	Time domain signal of three sine-waves with different frequencies and their Fourier transform	26
1.6.3	Commonly used Fourier pairs in NMR	28
1.6.4	The free-induction decay (FID) and its Fourier transform	29
1.6.5	The sinc-function and its Fourier transform	30

Chapter 2

2.1.1	T_1 -relaxation curve	32
2.1.2	Inversion-recovery pulse sequence	33
2.1.3	Signal intensity versus inversion time for the inversion-recovery experiment	34
2.2.1	Hahn spin-echo pulse sequence	36
2.2.2	Spin behavior during the Hahn spin-echo pulse sequence	37
2.2.3	Signal from the Hahn spin-echo pulse sequence	38
2.3.2.1	Stejskal-Tanner pulsed-field-gradient spin-echo pulse sequence	42
2.3.3.1	Diffusion-weighted stimulated-echo pulse sequence	46
2.4.1.1	Spatial position as a function of the relative field strength	48
2.4.1.2	Relation between spatial position and frequency	49
2.4.3.1	The sinc-function and its Fourier transform	51
2.4.3.2	Effects of the gradient slope and frequency bandwidth on the slice thickness	53
2.4.4.1.1	Conventional imaging of k -space	57
2.4.4.1.2	Spin-echo imaging pulse sequence	58
2.4.4.2.1	k -space trajectory for echo-planar imaging	59
2.4.4.2.2	Spin-echo echo-planar imaging pulse sequence	60

Chapter 3

3.1.1	Illustration of unrestricted diffusion	65
3.1.2	Stejskal-Tanner pulsed-field-gradient pulse sequence	66
3.1.3	Attenuation curves for freely diffusing water and water diffusing in the interstitial space of a bead pack	68
3.1.4	Illustration of restricted diffusion	69
3.1.5	Time dependence of the measured diffusion coefficient in a tumor	70
3.1.6	Diffraction peak	74
3.1.7	Diffusion in the presence of barriers	75
3.1.8	Signal attenuation of a Cutbank 26 mudstone rock core	78
3.1.9	Absolute RTO probability, F , of a Cutbank 26 mudstone rock core and freely diffusing water at different diffusion times	80
3.1.10	RTO enhancement, R , of a Cutbank 26 mudstone rock core	82
3.2.2.1	Modified pulsed-field stimulated-echo pulse sequence	85
3.3.1	Signal attenuation of diffusing water in a RIF-1 tumor	90
3.3.2	Absolute RTO probability, F , measured in a RIF-1 tumor	91
3.3.3	RTO enhancement, R , measured in a RIF-1 tumor	92
3.3.4	RTO enhancement of four RIF-1 tumors at different diffusion times	93
3.3.5	Signal attenuation curves of freely diffusing water and water diffusing in viable and necrotic RIF-1 tumor tissue	94
3.3.6	T_2 , ADC, RTO enhancement maps and histology of three tumors	96
3.3.7	ADC and RTO enhancement histograms of three RIF-1 tumors	97
3.3.8	Plot of the mean T_2 versus necrotic tumor fraction	98
3.3.9	Plot of the mean ADC versus necrotic tumor fraction	99
3.3.10	Plot of the mean RTO enhancement versus necrotic tumor fraction	100

Chapter 4

4.3.1	Tumor growth curves of RIF-1 tumors	121
4.3.2	ADC, RTO enhancement and T_2 maps from a control animal	124
4.3.3	ADC, RTO enhancement and T_2 maps from a treated animal	125
4.3.4	ADC, RTO enhancement and T_2 histograms of a control animal	129
4.3.5	ADC, RTO enhancement and T_2 histograms of a treated animal	130
4.3.6	Mean ADC, RTO enhancement and T_2 of a control and treated animal	132
4.3.7	Mean \pm standard deviation of mean ADC, RTO enhancement and T_2 of control and treated animals	133

Chapter 5

5.1.1	NMR pulse sequences with constant and pulsed diffusion gradient	146
5.2.2.1	Pulse sequences for the assessment of the diffusion coefficient	156
5.3.1	Measured diffusion coefficient of 1.6 cm ³ RIF-1 tumor	161
5.3.2	Measured diffusion coefficient of 2.6 cm ³ RIF-1 tumor	162
5.3.3	Measured diffusion coefficient of 3.0 cm ³ RIF-1 tumor	163
5.3.4	Measured diffusion coefficient of 0.7 cm ³ RIF-1 tumor	164

Chapter 6

6.2.2.1	Experimental protocol for pO ₂ monitoring of RIF-1 tumors.....	175
6.3.1	Calculated pO ₂ map and raw image of a RIF-1 tumor slice.....	179
6.3.2	Plot of a pixel at the noise level versus the inversion-time.....	179
6.3.3	Plot of pixel producing a good fit versus the inversion-time.....	180
6.3.4	Oxygen maps of each slice and day from a RIF-1 tumor.....	181
6.3.5	Oxygen tension maps and their histograms of a RIF-1 tumor.....	182
6.3.6	Graph of the mean pO ₂ for each slice at all imaging days.....	183
6.3.7	Plot of the mean tumor pO ₂ versus time.....	184

List of Tables

Chapter 1

1.2.1.1 Gyromagnetic ratios for nuclei commonly observed by *in vivo* NMR.....6

Chapter 4

4.3.1 Tumor doubling times of RIF-1 tumors.....122

Chapter 1

Nuclear Magnetic Resonance Theory

1.0 Nuclear Magnetic Resonance

The phenomenon of nuclear magnetic resonance (NMR) has come a long way since its discovery by Bloch (Block, Hansen and Packard, 1946) and Purcell (Purcell, Torrey and Pound, 1946). NMR is a methodology to study the behavior of assemblies of large numbers of atomic nuclei in a magnetic field. The nuclear property that is of interest in NMR is its angular momentum or spin. The placement of atomic nuclei with spin in a constant magnetic field will result in the separation of a single energy level into multiple energy levels. The energy difference between states is proportional to the applied magnetic field strength. This splitting of energy levels is known as the Zeeman effect. At thermal equilibrium, the number of nuclei in lower energy states is slightly higher than the number of nuclei in higher energy states. Nuclei can move from a lower energy state to a higher by absorbing energy or relax from a higher to a lower energy state by transferring energy to the molecular lattice.

In NMR we are interested in the angular momentum or spin of the nuclei. Since nuclei are positively charged, the spins can be modeled as a current loop with a resulting magnetic moment. At equilibrium, in the absence of an external magnetic field, the net magnetic moment of an ensemble of nuclei is zero. Exposing the nuclei to an external magnetic field leads to the splitting of a single energy level into multiple energy levels with different occupancy and hence a non-zero net magnetic moment. Following radiofrequency (RF) excitation the magnetic moment precesses around the direction of the applied magnetic field and induces a signal in a RF receiver coil that is proportional to the magnitude of the net magnetic moment of an ensemble of nuclei. As the spins

return to their equilibrium position, the net magnetic moment decreases toward zero. The rate of the return to equilibrium is dependent upon the environment of the nuclei and analysis of the decaying signal contains information about that environment.

For many years NMR was used as a spectroscopic tool, before its use for imaging was proposed (Lauterbur, 1973). The number of different imaging techniques has increased since Lauterbur's proposal and advances in technology have significantly improved the quality of NMR images. Today, magnetic resonance imaging (MRI) is a widely accepted tool in the clinical environment for the detection and diagnosis of various diseases.

To understand the formation of NMR spectra and images one needs to have an understanding of the underlying physics governing the formation of the signal. This chapter gives a brief introduction into the fundamentals, origin, generation, acquisition, and processing of the NMR signal and discusses only the relevant principles for the work in this dissertation. For a more detailed description of the physics and principles of NMR the reader may consult numerous references (Abragam, 1962; Morris, 1986; Smith and Lange, 1998; Salib and Brown, 1998).

1.1 The Magnetic Field

Between the two poles - north and south - of a magnet is a force field. The same force field produced by a permanent magnet can also be produced by an electrical current

flowing through a conductor. The magnetic field strength induced by a current, I , through an n -turn circular conductor of radius, r , is given by:

$$H(r) = \frac{2\pi nl}{r} \quad [1.1.1]$$

The magnetic field strength and the magnetic induction or flux density, B , have the same orientation in a vacuum and are related through the magnetic field constant, μ_0 .

$$B_0 = \mu_0 H \quad [1.1.2]$$

Introduction of material into the magnetic field changes the magnetic flux density in the material from B_0 to B since the material can be polarized and contribute to the magnetic field strength, H , over the magnetic field constant, μ_0 , and the dimensionless proportionality factor known as the susceptibility constant, χ .

$$B = \mu_0(1 + \chi)H \quad [1.1.3]$$

A examination of Eq. [1.1.3] shows that a sample in a magnetic field can alter the magnetic flux density to values larger or smaller than the values generated from the magnetic field strength, since χ can be either negative or positive. This phenomenon is

of great importance in NMR since a change in the magnetic induction influences the NMR signal.

1.2 Physical Principles

The basic physical principles governing the NMR phenomenon are described by the behavior of nuclei exposed to an applied magnetic field. The following sections are a short description of these physical principles.

1.2.1 Property of the Spin

An important characteristic of the nucleus is the nuclear spin, which is the fundamental requirement for NMR. Spin is an inherent property of all protons and neutrons but only nuclei with a non-zero spin can be observed with NMR. The movement of protons, a small spherical positive charge distribution, and neutrons with their associated mass generates an orbital angular momentum, P . The rotation of the charge distribution around its center axis produces a small magnetic field. Even neutrons with

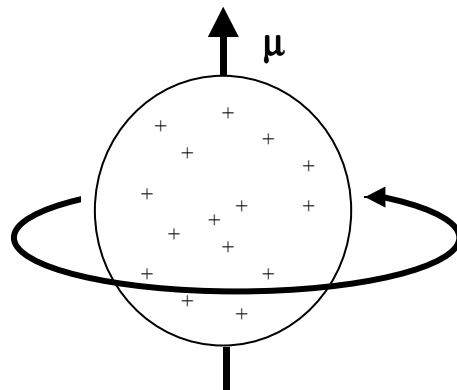


Fig. 1.2.1.1: A way to model the nuclear magnetic moment of a proton is to consider it as a spherical charge distribution rotating around its axis.

their unevenly distribution of positive and negative charges generate small magnetic fields. These small magnetic fields are called the nuclear magnetic dipole moment, μ .

The relation between μ and the nuclear angular momentum, P , is given by

$$\mu = \gamma P \quad [1.2.1.1]$$

where γ , the gyromagnetic ratio, is the proportionality constant for a given nucleus. The gyromagnetic ratio is a unique value for each nucleus and is proportional to the charge-to-mass ratio of the nucleus. Table 1.2.1.1 shows the gyromagnetic ratios for nuclei commonly observed by *in vivo* NMR.

Nucleus	¹³ C	²³ N	³¹ P	¹⁹ F	¹ H
$\gamma/2\pi$ (MHz/T)	10.71	11.27	17.25	40.08	42.58

Table 1.2.1.1: Gyromagnetic ratios, γ , for nuclei commonly observed by *in vivo* NMR.

1.2.2 The Nuclear Angular Momentum

Classically the angular momentum, P , could be oriented in any direction and has an arbitrary magnitude. Quantum mechanically, however, the angular momentum can only have discrete (quantized) values given by:

$$P = \sqrt{I(I+1)} \quad [1.2.2.1]$$

where \hbar is Planck's constant, h , divided by 2π , and I is the spin quantum number ($I = 0, 1/2, 1, 3/2, \dots$), which depends on the internal structure of the nucleus. Individual protons and neutrons have a spin quantum number of

$I = 1/2$ and form pairs (one spin up and one spin down) causing a cancellation of their respective nuclear angular momenta. Nuclei with an odd number of protons and/or neutrons have unpaired spins resulting in a non-zero nuclear spin quantum number, I . In

addition to the magnitude, the angular momentum has a direction, which can also be

shown to be quantized. Allowed directions for the vector are limited to values corresponding to the values of P_z given by

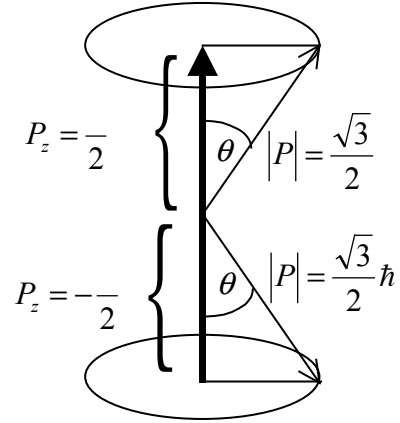


Figure 1.2.2.1: The angular momentum of a spin-1/2 system and its possible orientations.

$$P_z = m_I \hbar \quad \text{with } m_I = -I, -I+1, \dots, I-1, I \quad [1.2.2.2]$$

where m_I is referred to as the directional (or magnetic) spin quantum number. For a spin-1/2 nucleus, m_I can only have the values of $+1/2$ and $-1/2$ yielding only two possible

orientations of P (as represented in Fig. 1.2.2.1) with $\theta = \cos^{-1}\left(\frac{P_z}{|P|}\right) = 54^\circ 44'$, $P_z = \pm \frac{1}{2}$

and $|P| = \frac{\sqrt{3}}{2}$.

1.2.3 The Nuclear Magnetic Dipole Moment

The nuclear magnetic dipole moment, μ , is related to the angular momentum, P , by the gyromagnetic ratio, γ , as defined by Eq. [1.2.1.1]. Since P is quantized (Eq. 1.2.2.1), then μ must also possess discrete values by association through Eq. [1.2.1.1]. Combining Eq. [1.2.1.1] and Eq. [1.2.2.1] the nuclear magnetic dipole moment is given by

$$\mu = \gamma \sqrt{I(I+1)} \quad I = 0, 1/2, 1, 3/2, \dots \quad [1.2.3.1]$$

The orientation of the nuclear magnetic dipole moment, μ , is always parallel or anti-parallel to the angular momentum, P , and zero if the angular momentum, P , is zero. The energy levels associated with these states are therefore the same and are said to be degenerate. In the absence of a polarizing magnetic field the energy of a magnetic nucleus is independent of the orientation of μ .

1.2.4 The Nuclei in a Magnetic Field

In the presence of an external magnetic field, B_0 , the degeneracy is removed. The potential energy, E , of the interaction between the magnetic field, B_0 , and the magnetic dipole moment, μ , is:

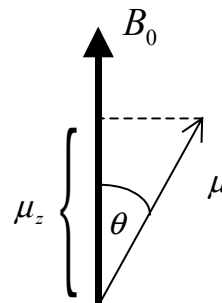


Figure 1.2.4.1: Interaction between the magnetic field and the magnetic dipole moment

$$E = \mu \bullet B_0 = -\mu B_0 \cos(\theta) = \mu B_0 \frac{m_l}{\sqrt{I(I+1)}} \quad [1.2.4.1]$$

where θ is the angle between the orientation of the magnetic field and the nuclear magnetic dipole moment. For a magnetic field, B_0 , along the z-axis, the potential energy of the z-component of the magnetic dipole moment, μ_z , is

$$E = -\mu_z B_0 \quad [1.2.4.2]$$

where the z-component of the nuclear magnetic dipole moment given by

$$\mu_z = \gamma \mathcal{P}_z = \gamma m \quad \text{where } m_l = -I, -I+1, \dots, I-1, I \quad [1.2.4.3]$$

as defined in Eq. [1.2.2.2].

For a spin- $\frac{1}{2}$ nucleus with $m_I = +\frac{1}{2}$ and $m_I = -\frac{1}{2}$ there are only two possible orientations of the nuclear magnetic dipole moment, μ , and hence the z-component can only be parallel or anti-parallel with respect to the magnetic field B_0 . The energy levels associated with each orientation are given by:

$$E_1 = -\mu_z B_0 = -\mu_z B_0 = -\frac{\gamma B_0}{2} \quad \text{for } m_I = \frac{1}{2} \quad [1.2.4.4]$$

and

$$E_2 = -\mu_z B_0 = -\mu_z B_0 = +\frac{\gamma B_0}{2} \quad \text{for } m_I = -\frac{1}{2} \quad [1.2.4.5]$$

Consequently, the difference in energy between the two different states is:

$$\Delta E = E_2 - E_1 = \frac{\gamma B_0}{2} - \left(-\frac{\gamma B_0}{2} \right) = \gamma B_0 \quad [1.2.4.6]$$

In order for a proton to change from one energy state to the other one it needs to emit or absorb the energy difference, ΔE , in the form of a photon which can be found by Bohr's relation:

$$\Delta E = h\nu \quad [1.2.4.7]$$

Combination of Eq. [1.2.4.6] and [1.2.4.7] yields:

$$\frac{\gamma h B_0}{2\pi} = h\nu \quad [1.2.4.8]$$

and can be simplified to

$$\nu = \frac{\omega_0}{2\pi} = \frac{1}{2\pi} \gamma B_0 \quad [1.2.4.9]$$

Equation [1.2.4.9] indicates that resonance absorption, inducing the transition from one energy state to the other, occurs at the Larmor frequency which is directly proportional to the magnetic flux density by the gyromagnetic ratio.

Classical physics provides a different way to visualize the behavior of the magnetic dipole moment in an external magnetic field. Viewing the magnetic dipole moment, μ , as a small magnet that is oriented at an angle, θ , with respect to the magnetic field, B_0 , a torque is applied to the magnetic dipole moment, μ , causing it to precess around, B_0 . The precession can be described by the Larmor frequency:

$$\omega = \gamma \mu \times B_0 \quad [1.2.4.10]$$

1.2.5 Bulk Magnetization

Up to this point we have only considered the behavior of a single isolated proton exposed to an applied magnetic field. The NMR signal arises, however from the vector sum of a large number of nuclear magnetic dipole moments, μ . In the absence of a magnetic field, the magnetic dipole moments are randomly oriented (Fig. 1.2.5.1) within the sample and

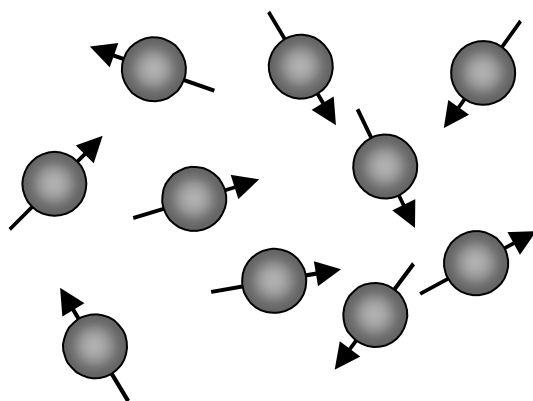


Figure 1.2.5.1: Random orientation of the individual magnetic moments in a bulk sample in the absence of a magnetic field. The resulting magnetic moment of the sample is zero.

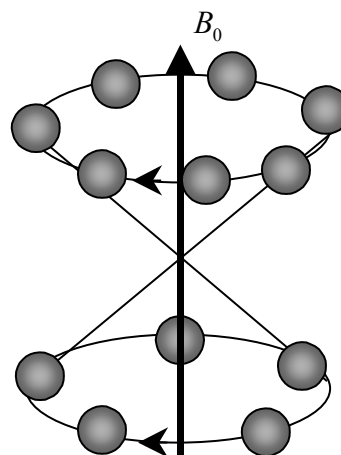


Figure 1.2.5.2: The spin- $\frac{1}{2}$ nuclei of a bulk sample in a magnetic field precess about B_0 in two cones corresponding to the parallel and anti-parallel state.

the resulting net magnetic moment is zero. The application of a magnetic field, B_0 , causes the nuclei to precess about z-axis at the Larmor frequency at an angle θ_0 . Depending on their state, some nuclei precess about the -z-axis and the other nuclei about the +z-axis, forming two cones of precession (Fig. 1.2.5.2). In most materials at room temperature more protons precess in the upper cone than in the lower resulting in a net

magnetization, M_0 . The phase distribution of the nuclei in the upper and lower cone are randomly distributed and cancel, so there is no net transverse magnetization.

The distribution of the magnetic dipole moments between the lower energy state (parallel), α , and the higher energy state (anti-parallel), β , is shown in Fig. 1.2.5.3. For a spin- $1/2$ system, the spins will be distributed between the energy levels according to the Boltzmann distribution. The ratio of the populations is given by

$$\frac{N_\beta}{N_\alpha} = \frac{e^{-\frac{E_\beta}{kT}}}{e^{-\frac{E_\alpha}{kT}}} = e^{-\frac{\Delta E}{kT}} \quad [1.2.5.1]$$

where N_α and N_β are the number of nuclei in the respective energy levels E_α and E_β , $\Delta E = E_\beta - E_\alpha$ is the energy difference between the two levels, $k = 1.28 \times 10^{-23} \frac{J}{K}$ is the Boltzmann constant, T is the temperature in Kelvin and

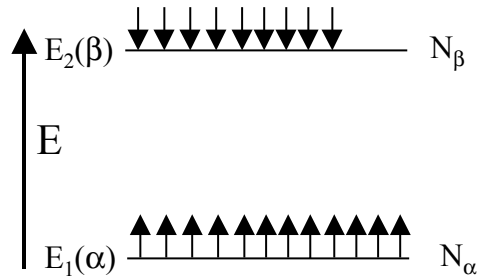


Figure 1.2.5.3: The two energy states α and β for a spin- $1/2$ system with spin population according to the Boltzmann distribution.

$$N_T = N_\alpha + N_\beta \quad [1.2.5.2]$$

is the total number of nuclei. NMR measures the population difference, Δn , between the energy states, which is given by:

$$\Delta n = N_{\alpha} - N_{\beta} = \frac{1 - e^{-\frac{\Delta E}{kT}}}{1 + e^{-\frac{\Delta E}{kT}}} \quad [1.2.5.2]$$

Using the high "temperature approximation", where $\frac{\Delta E}{kT} \ll 1$, and approximating an exponential using a Taylor's series expansion leads to:

$$\Delta n = N_{\alpha} - N_{\beta} \cong N_T \frac{\Delta E}{2kT} \quad [1.2.5.3]$$

Equation [1.2.5.3] represents an estimate of the population difference between the number of nuclei aligned with or against the externally applied magnetic field. The magnetization, M_0 , is a result of the vector sum of the individual magnetic moments and can be represented by

$$M_0 = \mu_z(\Delta n) = \frac{1}{2} \gamma (\Delta n) = \frac{\gamma^2 \hbar^2 B_0}{4kT} \quad [1.2.5.4]$$

or if we return to the classical approach, the net magnetization can be represented as the sum of the individual dipole moments (Fig. 1.2.5.4). Summation over the individual dipole moments (magnets) yields Eq. [1.2.5.5].

$$\vec{M}_0 = \frac{d\vec{\mu}}{dt} = (\gamma\vec{\mu} \times B_0) \quad [1.2.5.5]$$

Examination of the Eqs. [1.2.5.4] and [1.2.5.5] reveals that the net magnetization increases in magnitude proportional to the applied magnetic field.

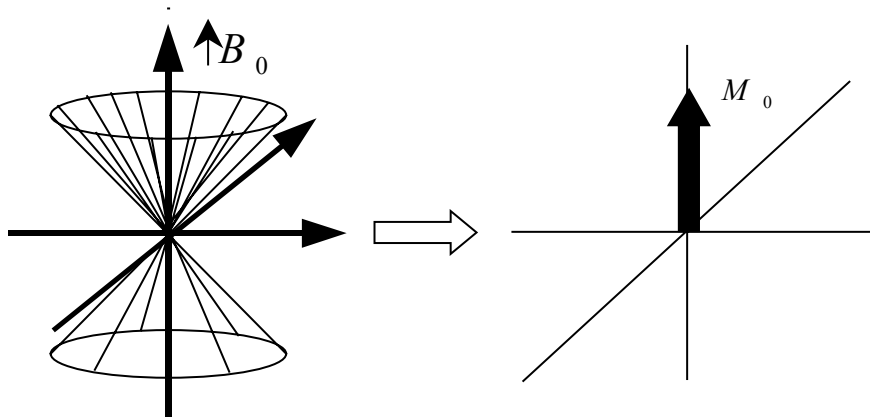


Figure 1.2.5.4: The individual nuclear magnetic dipole moments exposed to a magnetic field sum up to the net magnetization, M_0 , since more magnetic dipole moments are aligned parallel rather than anti-parallel to the field.

1.3 Radio-Frequency Pulses and the Rotating Reference Frame

Bloch (1946) developed a set of differential equations to describe the behavior of the macroscopic magnetization, M_0 , in the presence of a magnetic field. The full Bloch equations in the laboratory frame reference are given by

$$\frac{dM_x}{dt} = \gamma B_0 M_y + \gamma B_1 \sin(\omega t) M_z - \frac{M_x}{T_2} \quad [1.3.1]$$

$$\frac{dM_y}{dt} = -\gamma B_0 M_x + \gamma B_1 \cos(\omega t) M_z - \frac{M_y}{T_2} \quad [1.3.2]$$

$$\frac{dM_z}{dt} = -\gamma B_1 [\sin(\omega t) M_x + \cos(\omega t) M_y] - \frac{M_z - M_0}{T_1} \quad [1.3.3]$$

where B_0 is the static magnetic field, B_1 is the magnetic field induced by the RF field, M_x , M_y , M_z , the x-, y- and z- components of the magnetization vector, respectively, T_1 the longitudinal-relaxation time and T_2 the transverse-relaxation time. The Bloch equations can predict the behavior of the net magnetization during a NMR experiment, but the calculations are laborious. The Bloch equations are easier to solve in a coordinate system rotating around B_0 at the

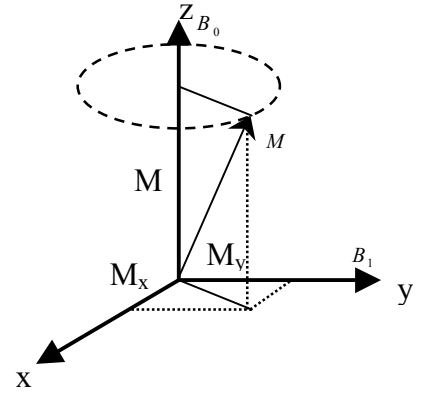


Figure 1.3.1: The net magnetization vector, M , and its components.

Larmor frequency, ω_0 . In this frame the equation of the motion of the net magnetization can be rewritten as

$$\left. \frac{dM}{dt} \right|_{\text{rotating}} = \gamma \mathcal{M} \times B_{\text{eff}} \quad [1.3.4]$$

with the effective magnetic field, B_{eff} , the vector sum of the static magnetic field, B_0 , the magnetic field from the applied RF pulse, B_1 , and the fictitious field, $\frac{\omega}{\gamma}$, in the rotating frame of reference (Fig. 1.3.2).

$$B_{eff} = B_0 + B_1 + \frac{\omega}{\gamma} \quad [1.3.5]$$

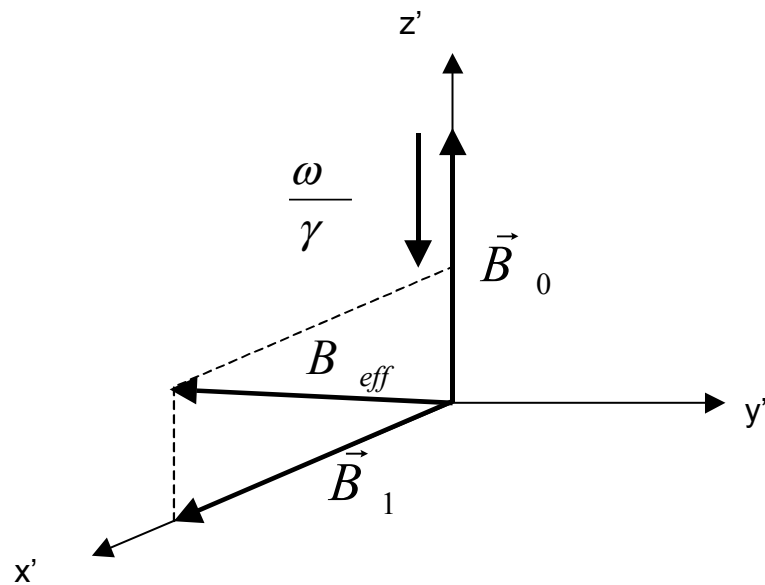


Figure 1.3.2: The effective magnetic field, B_{eff} , is the resulting vector sum of the static magnetic field, B_0 , the magnetic field from the applied RF pulse, B_1 , and the fictitious field, $\frac{\omega}{\gamma}$, in the rotating frame of reference.

In the absence of the magnetic field, B_1 , and by setting of the rotating frame frequency, ω , equal to the Larmor frequency (Eq. 1.2.4.9), ω_0 , the effective field B_{eff} , becomes

zero.

$$B_{eff} = B_0 + \frac{\omega_0}{\gamma} = 0 \quad [1.3.6]$$

Therefore, the motion equation of the net magnetization in the rotating frame (Eq. [1.3.4]) is also zero and the net magnetization, M , appears to be stationary.

$$\left. \frac{dM}{dt} \right|_{rotating} = \gamma \mathcal{M} \times B_{eff} = \gamma \mathcal{M} \times \left(B_0 + \frac{\omega_0}{\gamma} \right) = 0. \quad [1.3.5]$$

In the presence of the magnetic field, B_1 , from the applied RF pulse and with the rotating frame frequency, ω , equal to the Larmor frequency, ω_0 , Eq. [1.3.4] simplifies to:

$$\left. \frac{dM}{dt} \right|_{rotating} = \gamma \mathcal{M} \times B_1 \quad [1.3.6]$$

Thus an RF field oscillating at the Larmor frequency in a plane perpendicular to B_0 generates a static B_1 field in the rotating frame of reference that is orthogonal to B_0 and the spins precess around B_1 at a frequency of

$$\omega_1 = -\gamma B_1. \quad [1.3.7]$$

Rewriting the Bloch equations in the rotating frame of reference (Figure 1.3.3) results in:

$$\frac{du}{dt} = (\omega_0 - \omega)v - \frac{u}{T_2} \quad [1.3.8]$$

$$\frac{dv}{dt} = -(\omega_0 - \omega)u - \frac{v}{T_2} + \gamma B_1 M_z \quad [1.3.9]$$

$$\frac{dM_z}{dt} = -\left(\frac{M_z - M_0}{T_1}\right) - \gamma B_1 v \quad [1.3.10]$$

with

$$u = M_x \cos(\omega t) - M_y \sin(\omega t) \quad [1.3.11]$$

$$v = M_x \sin(\omega t) + M_y \cos(\omega t) \quad [1.3.12]$$

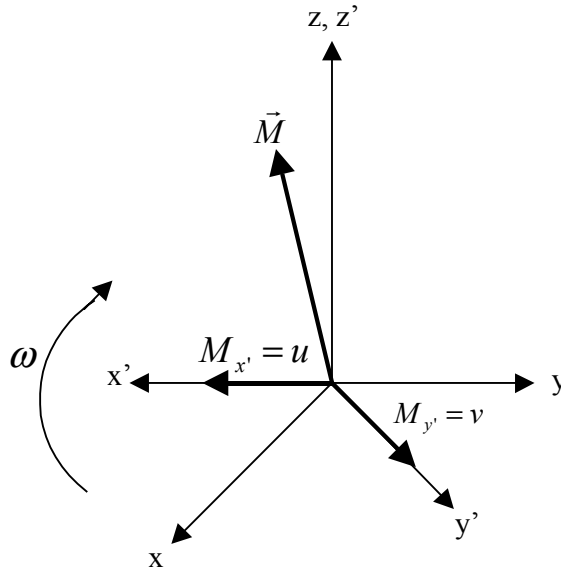


Figure 1.3.3: Relation between the laboratory frame of reference and the rotating frame of reference.

A closer look at Eq. [1.3.7] shows that control of the RF field duration allows the magnetization vector to precess or tip an angle θ_{ip} around the orthogonal axis. The tip angle, θ_{ip} , can be calculated by

$$\theta_{ip} = \gamma B_1 t_{RF} \quad [1.3.12]$$

where t_{RF} is the duration of the RF field pulse, B_1 the magnetic field generated by the applied RF field, and θ_{ip} the flip angle. Varying either the RF field duration or the magnitude of the B_1 field allows the flip angle to be controlled.

1.4 Nuclear Relaxation

Relaxation is the process by which the magnetization returns to its equilibrium configuration. Introduction of a sample into a magnetic field, B_0 , causes the nuclei to precess about B_0 at an angle, θ_0 , to the axis along the field. Excitation by an RF pulse forces the magnetic moments into phase unity, while simultaneously precessing about B_1 increasing the angle between the magnetization vector and the B_0 field. The recovery of the magnetization along the longitudinal axis of the B_0 field is termed T_1 relaxation and the loss of phase coherence in the transverse plane is described by T_2 relaxation.

1.4.1 T_1 Relaxation (Longitudinal or Spin-Lattice Relaxation)

Spin-lattice relaxation is the process by which the spins return to their equilibrium distribution following energy absorption imparted by an RF pulse. Absorption of energy by nuclei allows them to migrate from the lower energy state (E_1) to the higher energy state (E_2). The number of nuclei undergoing the transition from one energy state to the other energy state depends on the duration and magnitude of the imparted energy. Figure 1.4.1.1 shows the population distribution after the excitation of the nuclei by a 90° and 180° RF pulse.

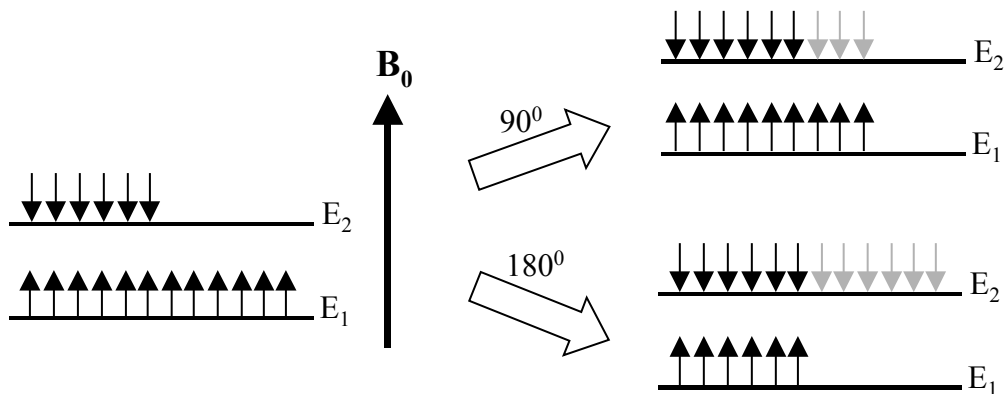


Figure 1.4.1.1: Distribution of the spin population at equilibrium (left side) and after excitation by a 90° and 180° RF pulse. Once excited the spins return to their equilibrium distribution by the longitudinal relaxation process. The resulting magnetization along the z axis is zero and $-M_0$ for the 90° and 180° RF pulse, respectively. The shaded arrows represent spins that have absorbed energy and changed their orientation with respect to the main magnetic field.

The relaxation process by which the spins return to their thermal equilibrium deposits energy into the molecular lattice of which the spins are part. Fluctuating electromagnetic field components of other magnetic dipole moments in the lattice can interact with the spins in the same way that the fluctuating magnetic field from an applied RF pulse interacts with the spins. The components at the Larmor and twice the Larmor frequency can exchange energy with the spins and give rise to relaxation. The longitudinal relaxation can be described by

$$\frac{dM_z}{dt} = -\frac{M_z - M_0}{T_1} \quad [1.4.1.1]$$

where T_1 is the time constant governing the relaxation process and M_0 the equilibrium magnetization. Solving of the differential Eq. [1.4.1.1] leads to

$$M_z(t) = M_0 \left(1 - e^{-\frac{t}{T_1}} \right) \quad [1.4.1.2]$$

for the case where a 90° RF pulse is used to excite the nuclei.

1.4.2 T_2 Relaxation (Transverse or Spin-Spin Relaxation)

Transverse or spin-spin relaxation is a process by which the magnetization in the transverse plane loses its phase coherence. Excitation of the net magnetization by a 90°

RF pulse, flips the magnetization, M_0 , into the transverse plane. The spins are now oriented along the same axis and therefore their phase difference is zero. The observable NMR signal in the transverse plane is the vector sum of the magnetization of the individual spins, precessing at the Larmor frequency about the longitudinal axis. Motion of other particles in the lattice - especially other nuclei - causes variations in the local magnetic field. Nuclei interacting with these particles see either a stronger local magnetic field causing them to precess faster or a weaker magnetic field causing them to precess slower than the Larmor frequency. This fluctuation, which can be transient as well as random, causes the coherent signal to de-phase (i.e., lose its coherence), as the spins exchange energy, until there is no net transverse magnetization remaining and the spins have again assumed their random phase distribution.

The difference in the precessional frequency of individual nuclei results in a loss of phase coherence which is quantified by the relaxation time constant, T_2 . Mathematically, the effect of the T_2 relaxation can be expressed as

$$M_{xy}(t) = M_0 e^{-\frac{t}{T_2}} \quad [1.4.2.1]$$

where M_{xy} is the transverse magnetization at the time, t , and M_0 is the magnetization following a 90° RF pulse for a system that was initially at the Boltzmann equilibrium.

Magnetic field inhomogeneity, molecular diffusion and magnetic susceptibility are other

external factors that can cause additional differences in the local magnetic field experienced by individual spins resulting in additional loss of the coherence. All these contributions are combined in the transverse relaxation time constant, T_2^* , given by:

$$\frac{1}{T_2^*} = \frac{1}{T_2} + \frac{1}{T_{2(\text{diffusion})}} + \frac{1}{T_{2(\text{field inhomogeneity})}} + \frac{1}{T_{2(\text{susceptibility})}} \quad [1.4.2.2]$$

1.5 The Free-Induction Decay

The net magnetization can be flipped into the transverse plane by the applied B_1 field produced by an RF pulse. After removal of the B_1 field, the transverse magnetization, M_{xy} , rotates in the xy-plane at the Larmor frequency. According to the law of Faraday, this time-varying magnetic field can induce a current in a receiver coil placed in the same plane. The sinusoidal signal induced by the transverse magnetization, M_{xy} , is referred as the free-induction decay (FID) as shown in Fig. 1.5.1. Since we observe the signal from

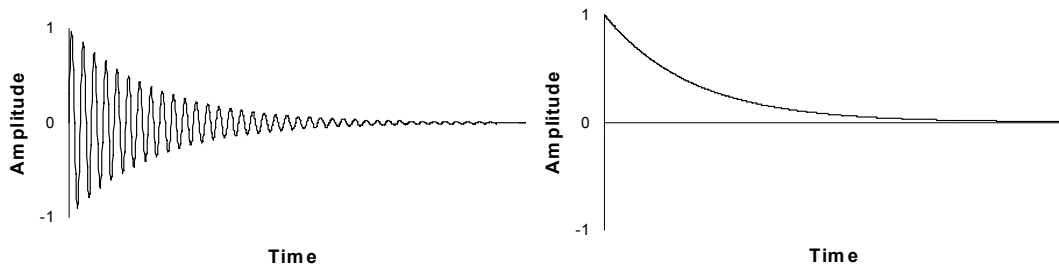


Figure 1.5.1: The left side shows the free-induction decay (FID) generated by the precessing magnetization in the transverse plane. The decay envelope is characterized by the T_2^* relaxation constant. The right side shows the same FID seen from the rotating-reference frame with the rotating-frame frequency equal to the Larmor frequency.

the rotating frame of reference, the frequency components contained in the FID are the differences between the rotating frame frequency and the precession frequency of the nuclei. The decaying envelope enclosing the FID in Fig. 1.5.1 is caused by the loss of phase coherence in the xy-plane due to T_2^* -relaxation effects and the FID can be described as

$$M_{xy}(t) = M_0 e^{-\frac{t}{T_2^*}} \quad [1.5.1]$$

where M_{xy} is the transverse magnetization at time, t , and M_0 the initial amplitude of the generated signal in the transverse plane following a 90° RF pulse applied to a system at the Boltzmann equilibrium.

1.6 Fourier Transform

The FID signal is detected in the time domain and characterized by its amplitude over time. The Fourier transform (FT) of the signal is a Lorentzian-shaped peak in the frequency domain described by its center frequency and its amplitude. Both the time-domain and frequency-domain signals contain the same information, but the FT facilitates the extraction of multiple frequency components within a signal. The FT of a sine-shaped signal is a δ function (Fig. 1.6.1) at the frequency of the sine wave. In NMR, spins usually have different resonance frequencies due to differences in their

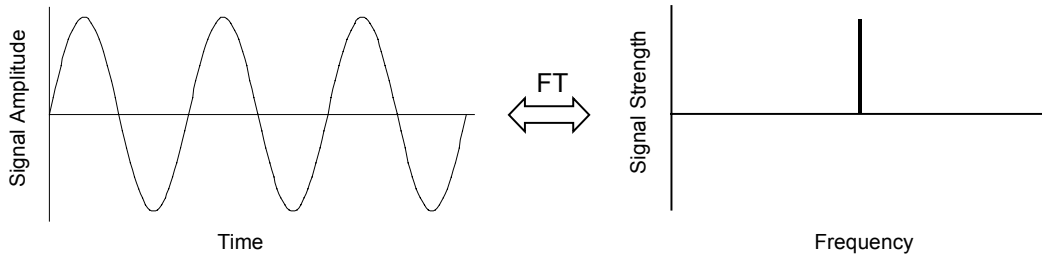


Figure 1.6.1: Single frequency sine-wave in the time domain and its Fourier transform in the frequency domain.

microenvironment. This results in a composite time-domain signal that is the summation of sine waves at different frequencies. Fig. 1.6.2 shows the time-domain signal for three different sine waves and their Fourier transform in the frequency domain.

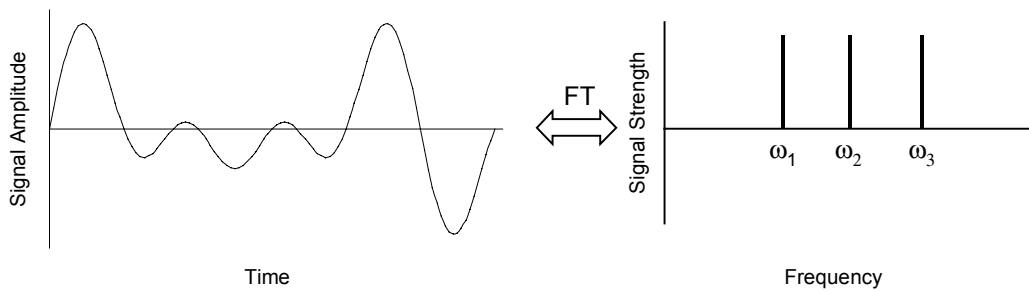


Figure 1.6.2: Time domain signal of three sine waves with different frequencies, $\omega_1 = 0.6\omega_2$, ω_2 , $\omega_3 = 1.4\omega_2$ and their Fourier transform in the frequency domain. Note that all three sine waves have the same amplitude, which is not apparent in the time domain.

The mathematical relation between the time-domain signal, $f(t)$, and the frequency-domain signal, $F(\omega)$ is given by the FT

$$F(\omega) = \int_{-\infty}^{\infty} f(t)e^{-i\omega t} dt \quad [1.6.1]$$

and the inverse Fourier transform (IFT)

$$f(t) = \frac{1}{2\pi} \int_{-\infty}^{\infty} F(\omega) e^{i\omega t} d\omega. \quad [1.6.2]$$

Since the FT and IFT are reciprocal representation of their domain, a simple multiplication in one domain is equivalent to a convolution in the other domain. This is expressed in the convolution theorem.

$$F(\omega) = F_1(\omega)F_2(\omega) \Leftrightarrow f(t) = f_1(t) \otimes f_2(t) \quad [1.6.3]$$

$$f(t) = f_1(t)f_2(t) \Leftrightarrow F(\omega) = F_1(\omega) \otimes F_2(\omega) \quad [1.6.4]$$

where \otimes denotes the convolution. Figure 1.6.3 summarizes the most commonly used Fourier pairs in NMR.

One of the most important functions in NMR is the exponentially decaying sine wave of frequency, ω_0 , with an envelope that is characterized by the transverse relaxation time constant, T_2^* . The FID can be written as

Commonly Used Fourier Pairs in NMR

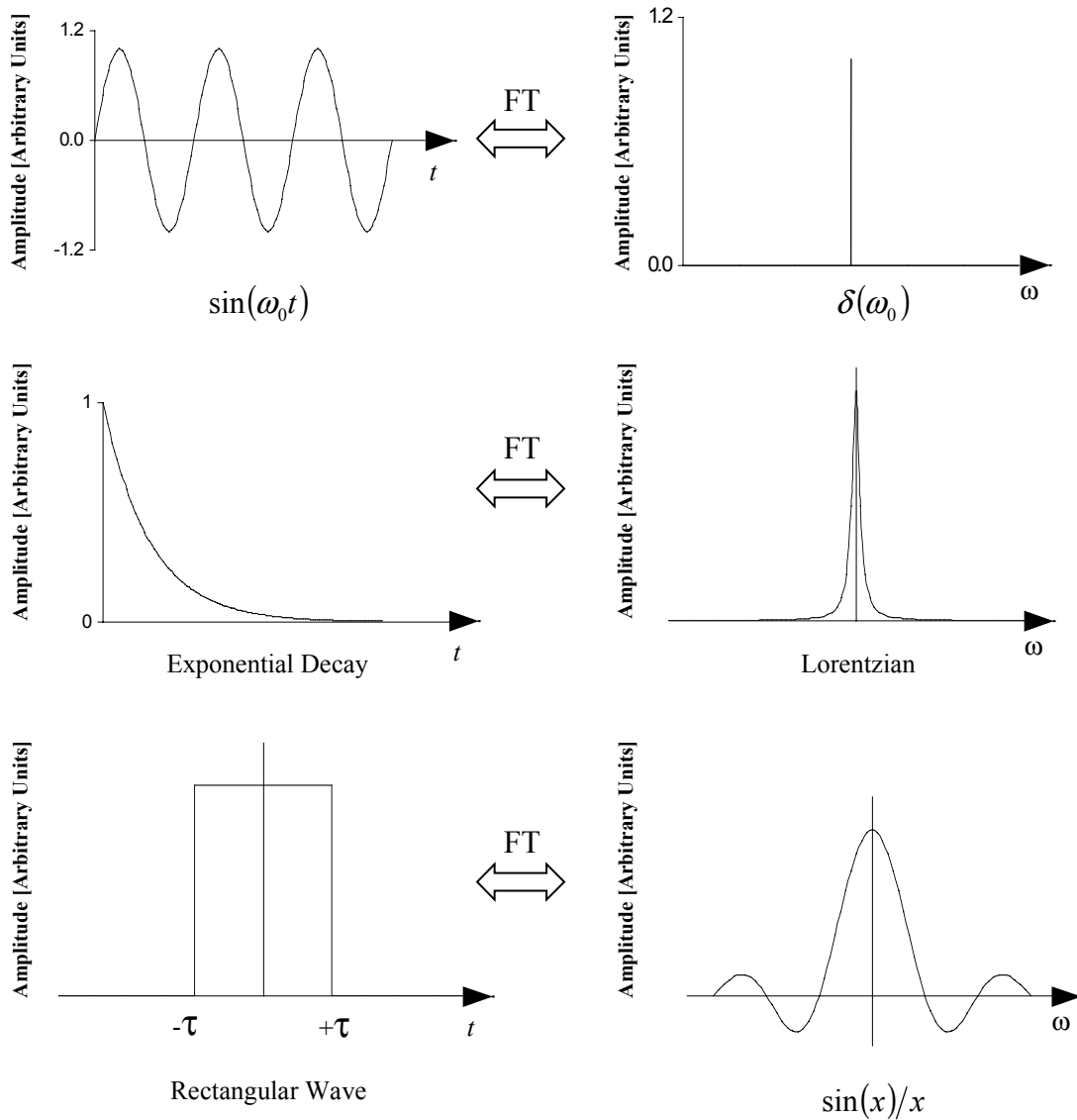


Figure 1.6.3: Commonly used Fourier pairs in NMR.

Top: The FT of a sine wave is a δ function at the frequency of the sine wave.

Center: The FT of an exponential decay is a Lorentzian function at zero frequency

Bottom: The FT of a rectangular wave from $\pm\tau$ centered around zero is a sinc function

$$\frac{\sin(x)}{x}$$

$$f(t) = \sin(\omega_0 t) e^{-\frac{t}{T_2^*}} \quad [1.6.5]$$

The FT of the FID is a Lorentzian centered around ω_0 and has a full-width at half-maximum (FWHM) of

$$FWHM = \frac{1}{\pi T_2^*} \quad [1.6.6]$$

as shown in Figure 1.6.4.

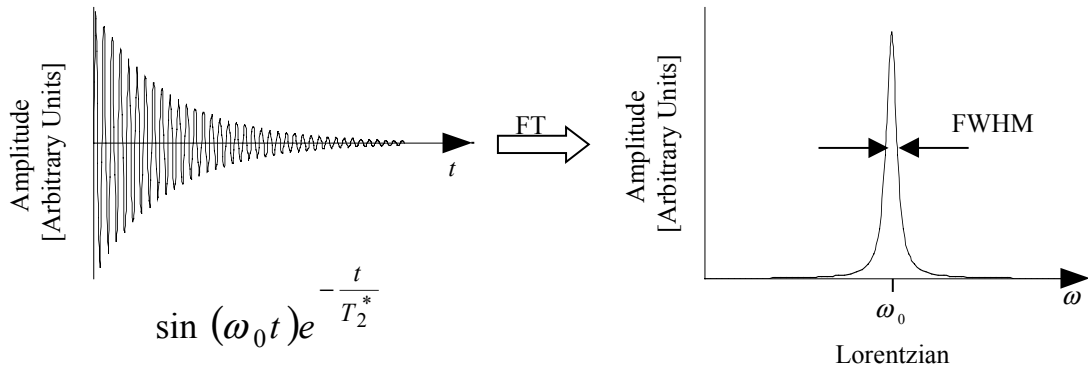


Figure 1.6.4: The FID and the Fourier transform of the FID. The frequency of the sine wave within the envelope determines the center frequency of the Lorentzian and the transverse relaxation constant, T_2^* , determines the full-width at half-maximum (FWHM) of the Lorentzian given by $\frac{1}{\pi T_2^*}$.

Another function of importance is the sine wave with an envelope of a sinc function

$\frac{\sin(x)}{x}$. Convolution of the sinc function with a sine wave of frequency, ω_0 , results in a

rectangular wave centered around, ω_0 , after the FT (Fig. 1.6.5). This will be discussed further in the section describing magnetic resonance imaging.

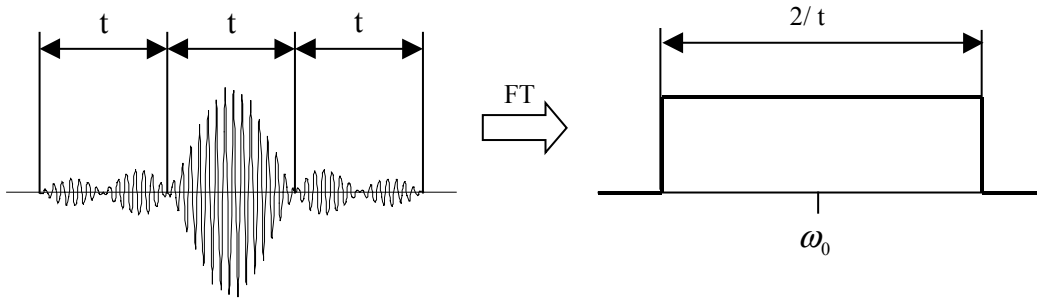


Figure 1.6.5: A sine wave of frequency, ω_0 , with an envelope of a sinc function and its FT. The rectangular function is centered around the frequency ω_0 of the sine wave and its width is determined by the sinc function, $\frac{\sin(x)}{x}$.

Chapter 2

Spin Manipulation

2.0 Spin Manipulation

The previous chapter discussed the relevant underlying physical and mathematical principles of NMR. This chapter deals with the manipulation of the net magnetization to extract information from the sample. Most of the methods discussed in this chapter are based on the evaluation of the amplitude, phase and frequency of the received signal after excitation by RF energy.

2.1 T_1 Measurement

The T_1 or spin-lattice relaxation time, as discussed in the previous chapter, is the time

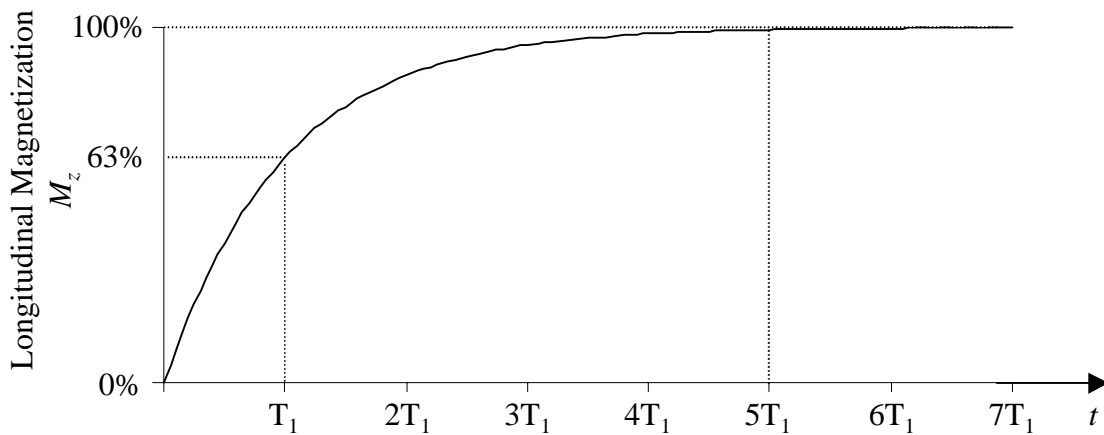


Figure 2.1.1: T_1 relaxation curve following excitation by a 90° RF pulse. After a time, $t = T_1$, 63% of the longitudinal magnetization is recovered and after a time, $t = 5T_1$, the longitudinal magnetization can be considered fully recovered for all practical purposes.

necessary to recover 63% of the equilibrium magnetization along the longitudinal axis after excitation by RF. Following a 90° RF pulse, recovery of the longitudinal magnetization is mathematically expressed by Eq. [1.4.1.2]. Figure 2.1.1 shows the

relaxation of the longitudinal magnetization following excitation by a 90° RF pulse. After a time period of $5T_1$, the longitudinal magnetization is considered to have fully recovered to the equilibrium state.

The T_1 relaxation time can be determined by conventional NMR in a number of ways. One of the most popular is the inversion-recovery (IR) pulse sequence (Fig. 2.1.2). The IR sequence consists of a 180° RF pulse, which inverts the magnetization along the $-z$

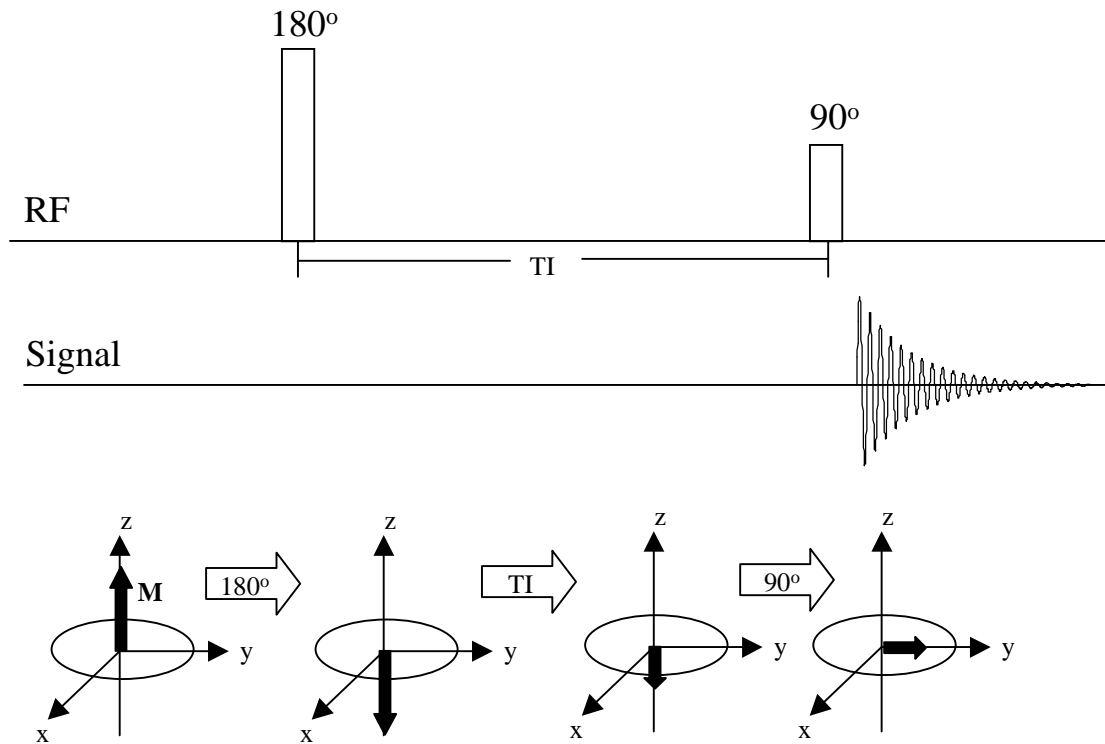


Figure 2.1.2: Inversion-recovery (IR) pulse sequence. The 180° RF pulse inverts the net magnetization vector, M . In the following time interval (TI) the magnetization is allowed to recover along the longitudinal axis towards equilibrium. After the inversion time, TI , a 90° RF pulse flips the residual magnetization into the transverse plane, where the signal can be measured.

direction, from where it recovers to its equilibrium state by T_1 (spin-lattice) relaxation.

Following inversion, the net magnetization vector has no transverse component and hence is not influenced by the (usually much faster) transverse relaxation, T_2^* . Following the 180° pulse, the magnetization recovers during an inversion time (TI) of variable length. The extent of the recovery is assessed by applying a 90° RF pulse, which tips the residual magnetization from the $-z$ direction into the xy -plane, where the signal is acquired. The magnitude of the residual signal (Fig. 2.1.3) depends on TI according to:

$$M_{xy} = M_0 \left(1 - 2e^{-\frac{TI}{T_1}} \right) \quad [2.1.1]$$

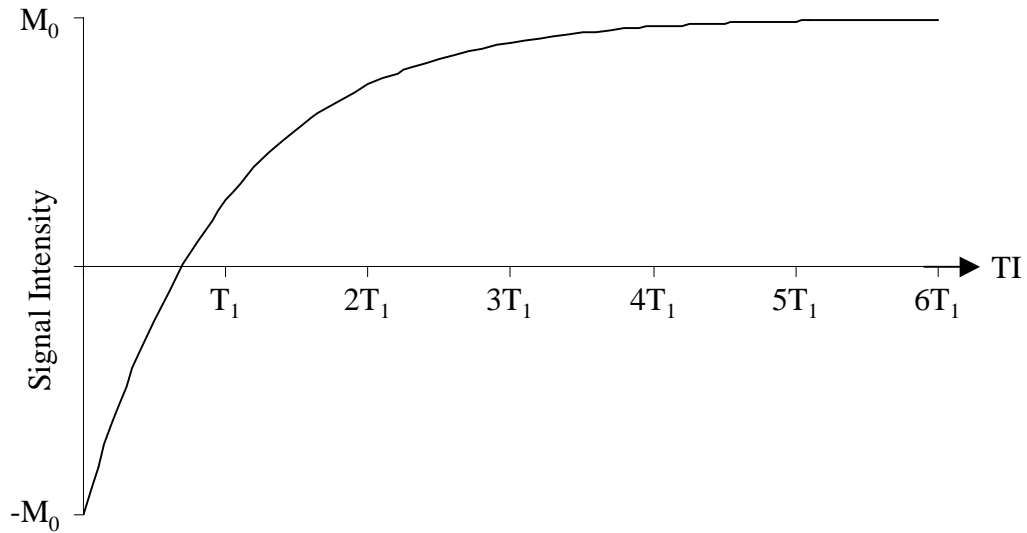


Figure 2.1.3: Signal intensity versus TI for an inversion-recovery experiment. The signal amplitude is dependent on the inversion time, TI , according to Eq. [2.1.1]. The longitudinal magnetization recovers to its equilibrium state after $5T_1$.

By varying TI over a suitable time range, the T_1 relaxation time can be found by fitting the acquired data to Eq. [2.1.1]. Alternatively the data can be fitted to the slope of $\ln(M_{xy}/M_0)$ versus TI in a logarithmic plot or to the exponential curve itself. In the case where the inversion pulse is not exactly 180° , Eq. [2.1.1] can be modified to

$$M_{xy} = A \left(1 - B e^{-\frac{TI}{T_1}} \right) \quad [2.1.2]$$

where A is some fraction of M_0 and B is the inversion efficiency.

2.2 T_2 Measurement

The loss of phase coherence in the transverse plane is not due to T_2 relaxation effects alone, but rather the cumulative results of many factors such as magnetic field inhomogeneities, molecular diffusion, and magnetic susceptibility. For the purposes of many NMR experiments it would be advantageous to eliminate the coherent effects of susceptibility to assess only the spin-spin relaxation time, T_2 . One of the first methods to measure the T_2 relaxation value was the Hahn spin-echo method (Hahn, 1950), which is based on the property that dephasing due to magnetic field inhomogeneities can be inverted.

Fig. 2.2.1 shows the Hahn spin-echo pulse sequence. The initial magnetization along the z axis is flipped into the transverse plane by a 90° RF pulse and the spins start to dephase.

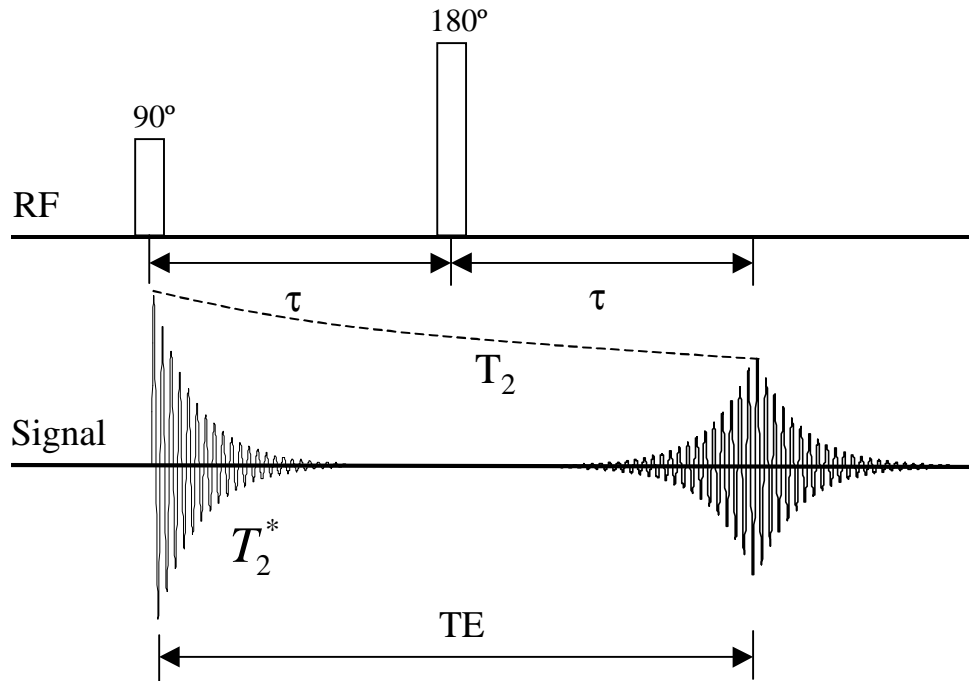


Figure 2.2.1: Hahn spin-echo (SE) pulse sequence. After excitation by a 90° RF pulse, spins dephase during the time interval, τ . A 180° RF pulse reverses the order of the precessing spins allowing them to refocus at the time $TE = 2\tau$. Only spins dephased by coherent processes (such as magnetic field inhomogeneities) will refocus at TE , while incoherent processes, such as T_2 relaxation, have a residual phase shift causing signal attenuation.

A 180° RF pulse applied along the x axis after the time, τ , reverses the order of the precessing spins. The spins continue to move in their original direction and refocus after another time period, τ . Phase gained due to incoherent processes, such as T_2 relaxation, cannot be refocused and manifests itself in the attenuation of the detected signal (Fig. 2.2.2). The refocused echo is known as the Hahn spin-echo and the attenuation of the signal at $TE = 2\tau$ is only a function of the intrinsic properties of T_2 relaxation. The magnitude of the refocused signal depends on the time, TE , (Fig. 2.2.3) according to:

$$M_{xy} = M_0 e^{-\frac{TE}{T_2}} \quad [2.2.1]$$

where $TE = 2\tau$ is the echo time and M_0 is the initial amplitude of the transverse magnetization following a 90° RF pulse applied to magnetization at the Boltzmann equilibrium. By varying TE over a suitable time range, the T_2 relaxation time can be found by fitting the acquired data to Eq. [2.2.1].

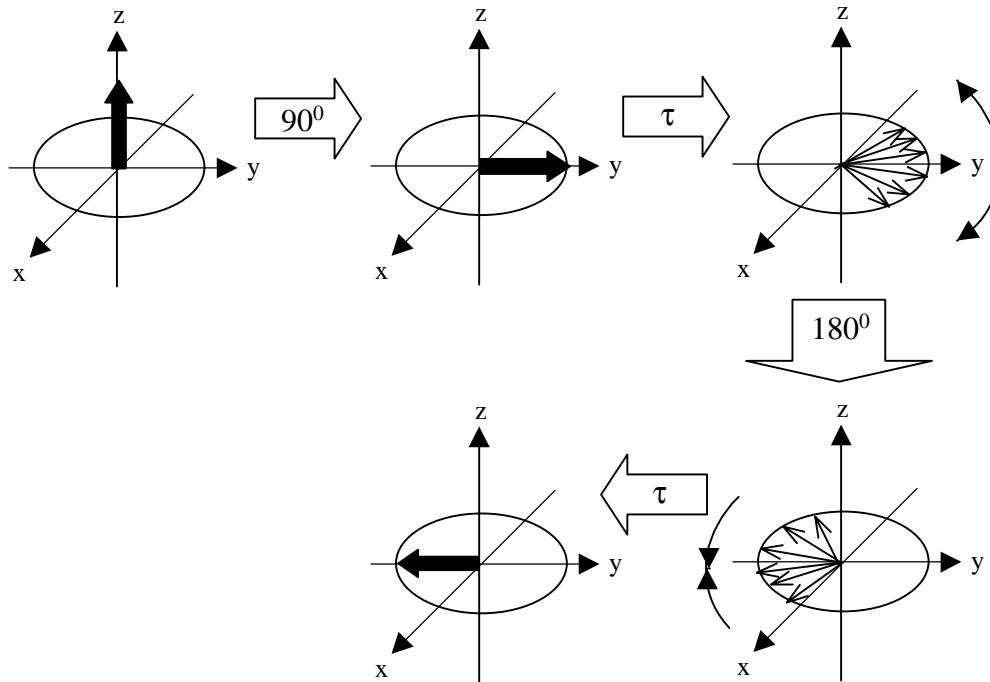


Figure 2.2.2: Spin behavior during the Hahn spin-echo sequence. The 90° RF pulse flips the magnetization into the transverse plane where it dephases during the time period, τ . The subsequent 180° RF pulse inverts the phase and dephased spins refocus after the second time interval τ to form the Hahn spin-echo.

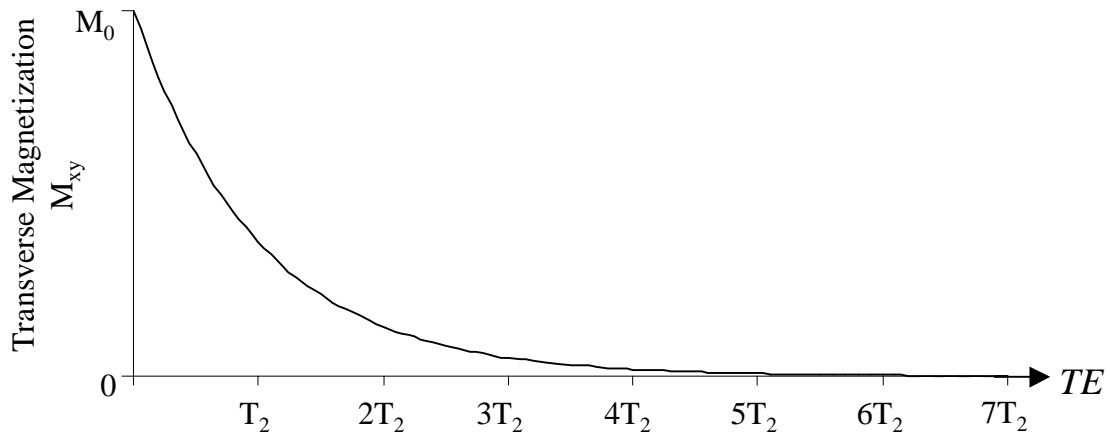


Figure 2.2.3: Transverse magnetization (signal) versus echo time (TE) for a Hahn spin-echo pulse sequence. The signal amplitude is dependent on the echo time, TE , according to Eq. [2.2.1].

2.3 Diffusion

This section is intended to provide the reader with an introduction to the theory of diffusion. It briefly discusses the underlying mechanism and theories important for understanding the following chapters. For a more detailed description and deeper insights into the theory of diffusion, the reader is referred to publications by Berg (1993) and Crank (1975).

2.3.1 Diffusion Theory

The self-diffusion coefficient, D , is a measurement of the net displacement of molecules caused by thermal energy (Brownian motion). A molecule in a system at temperature, T , has an average thermal energy of

$$E_T = \frac{nkT}{2} \quad [2.3.1.1]$$

where k is the Boltzmann constant and n is the number of degrees of freedom. The thermal energy of the particle is independent of its size, but the average velocity due to thermal energy associated with this particle is dependent upon its mass by

$$v_T = \sqrt{\frac{nkT}{m}} \quad [2.3.1.2]$$

In an isotropic solution, the diffusion coefficient, D , of a molecule is not only dependent on its mass, but also on the viscosity and temperature of the medium. This relationship can be quantitatively expressed by the Stokes-Einstein equation

$$D = \frac{kT}{f} = \frac{kT}{6\pi\eta R_h} \quad [2.3.1.3]$$

where k is the Boltzmann constant, T is the temperature in Kelvin and f is the frictional coefficient of the particle undergoing motion. The second equality assumes a spherical particle with a hydrodynamic radius, R_h , moving in a medium with a temperature-dependent viscosity, η .

The probability of finding a molecule originally at point \vec{r}_0 to be at position \vec{r} some time later can be measured by the root-mean-squared (RMS) displacement, $\langle x^2 \rangle$

$$\langle x^2 \rangle = \left\langle (\vec{r} - \vec{r}_0)^2 \right\rangle^{\frac{1}{2}} = \int_{-\infty}^{\infty} (\vec{r} - \vec{r}_0)^2 \rho(\vec{r}_0) P(\vec{r}_0 | \vec{r}, t) d\vec{r}_0 d\vec{r} \quad [2.3.1.4]$$

where $\rho(\vec{r}_0)$ is the spin density at location \vec{r}_0 , and $P(\vec{r}_0 | \vec{r}, t)$ the conditional probability for a particle to move from \vec{r}_0 to \vec{r} in the time, t . For an isotropic system, the solution to Fick's second law,

$$\frac{\partial P(\vec{r}_0 | \vec{r}, t)}{\partial t} = D \nabla^2 P(\vec{r}_0, \vec{r}, t) \quad [2.3.1.5]$$

yields the Gaussian displacement profile,

$$P(\vec{r} | \vec{r}_0, t) = \frac{1}{\sqrt{4\pi Dt}} e^{-\frac{(\vec{r} - \vec{r}_0)^2}{4Dt}} \quad [2.3.1.6]$$

Substituting Eq. [2.3.1.6] into Eq. [2.3.1.4] yields

$$\langle x^2 \rangle = \left\langle (\vec{r} - \vec{r}_0)^2 \right\rangle = 2Dt \quad [2.3.1.7]$$

which is known as Einstein's relation (in one dimension). For diffusion in more than one dimension, Einstein's relation is given by

$$\langle x^2 \rangle = 2nDt \quad [2.3.1.8]$$

where $\langle x^2 \rangle$ is the root-mean-squared displacement, and n is the number of degrees of freedom (number of dimensions) in which the spin can move. For isotropic, non-restricted diffusion, a plot of the root-mean-squared displacement $\langle x^2 \rangle$ versus \sqrt{t} is linear, while for anisotropic or restricted diffusion, the plot would deviate from its linear behavior.

2.3.2 Stejskal-Tanner Diffusion Measurement

The classical method of measuring diffusion with NMR is the pulsed-field gradient spin-echo (PFGSE) of Stejskal-Tanner (Stejskal and Tanner, 1965). Figure 2.3.2.1 shows the PFGSE pulse sequence, where magnetic field gradients are used to encode the molecular displacement by phase labeling the spins undergoing diffusion following a 90° RF pulse. The first gradient pulse imparts a phase shift of

$$\Phi_1 = \gamma \int_0^{\delta} G_z(t) p_1 dt \quad [2.3.2.1]$$

on the transverse magnetization, where γ is the gyromagnetic ratio, δ is the gradient pulse duration, G_z is the applied gradient strength of the diffusion-sensitizing gradient along the z-direction, and p_1 is the position of the spin along the z-axis during the first

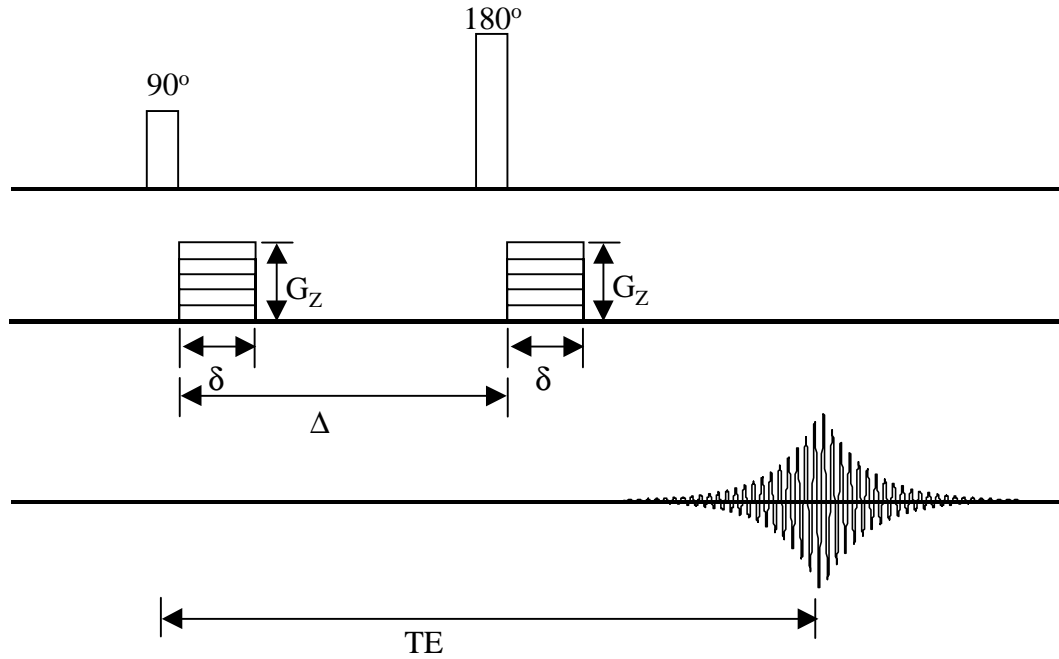


Figure 2.3.2.1: Stejskal-Tanner pulsed-field gradient spin-echo (PFGSE) sequence. The first gradient imparts a phase to the spins while the second gradient removes the phase. Spins undergoing diffusion between the two pulses will not refocus completely and have a residual phase which results in signal attenuation.

diffusion-gradient pulse. It should be noted that any gradient direction could have been chosen. A 180° RF pulse inverts the phase of the spins to $-\Phi_1$ in the transverse plane, before the second diffusion gradient imparts another phase of

$$\Phi_2 = \gamma \int_0^{\delta} G_z(t) p_2 dt \quad [2.3.2.2]$$

on the spins where p_2 is the position of the spin along the z-axis during the second diffusion-gradient pulse. The resulting phase shift after the two gradient pulses is therefore

$$\Phi_2 - \Phi_1 = \gamma \int_0^{\delta} G_z(t)(p_2 - p_1)dt \quad [2.3.2.3]$$

For stationary spins, $p_1 = p_2$, and there is no residual phase accumulation, while for moving spins ($p_1 \neq p_2$) there is a net residual phase shift. For an assembly of incoherently moving spins, the sum of the residual phase shifts will attenuate the spin-echo amplitude with respect to that of non-moving spins. The accumulated phase and magnitude of the attenuated signal is dependent on the phase difference the spins acquire during the observation period and can be written as

$$\frac{S}{S_0} = \int_{-\infty}^{\infty} e^{i\gamma G(\delta)(\Phi_2 - \Phi_1)\delta} \times P(p_2 | p_1, \tau) dp_1 dp_2 \quad [2.3.2.4]$$

where $P(p_2 | p_1, \tau)dp_2$ is the conditional probability that a spin starting at position p_1 will be found after a time, τ , between position p_2 and $p_2 + dp_2$, S_0 is the spin-echo amplitude without diffusion gradients, and S is the echo amplitude of the attenuated signal.

The signal attenuation for a Stejskal-Tanner spin-echo diffusion experiment with finite pulse width is given by (Stejskal and Tanner, 1964)

$$\frac{S}{S_0} = e^{-\gamma^2 \delta^2 G^2 D \left(\Delta - \frac{\delta}{3} \right)} \quad [2.3.2.5]$$

where S is the measured signal, S_0 is the signal amplitude with no diffusion gradient applied, δ is the diffusion gradient duration, γ is the gyromagnetic ratio, D is the diffusion coefficient, and Δ the time separation between the applied diffusion gradients.

The above equation can be re-written as (LeBihan et. al., 1991)

$$\frac{S}{S_0} = e^{-bD} \quad [2.3.2.6]$$

where

$$b = \gamma^2 G^2 \delta^2 \left(\Delta - \frac{\delta}{3} \right) \quad [2.3.2.7]$$

represents the gradient terms. For non-rectangular gradient pulses b must be modified to reflect the shape of the gradient pulses (Price and Kuchel, 1990). For half-sine-shaped diffusion gradient pulses, b is:

$$b = \gamma^2 \left(\frac{2}{\pi} \right)^2 G^2 \delta^2 \left(\Delta - \frac{\delta}{4} \right) \quad [2.3.2.8]$$

2.3.3 Diffusion-Weighted Stimulated-Echo

In order to measure the NMR signal at long diffusion times one has not only to deal with the signal attenuation due to diffusion (Eq. 2.3.2.5) but also with the simultaneously occurring signal attenuation due to T_1 and T_2 relaxation. This becomes a particular problem when the T_2 of the sample is much shorter than the diffusion time, since the signal attenuates due to T_2 relaxation by

$$S \propto e^{-\frac{TE}{T_2}} . \quad [2.3.3.1]$$

Since T_1 in biological systems is usually much longer than T_2 , it is possible to store the net magnetization for some part of the experiment along the longitudinal axis where it is only influenced by the slower T_1 relaxation.

The stimulated-echo (STE) pulse sequence (Hahn, 1950) is an example of how this can be accomplished. Fig. 2.3.3.1 shows a diffusion-weighted STE pulse sequence with added diffusion gradients (Tanner, 1970). The first 90° RF pulse puts the magnetization into the transverse plane and the second 90° RF pulse stores half of the transverse magnetization along the longitudinal axis. During the time, T_M , the stored magnetization

is only affected by T_1 relaxation and the crusher gradient completely dephases any magnetization that remained in the transverse plane after the second 90° RF pulse. This deliberate dephasing of the residual transverse magnetization during the TM period

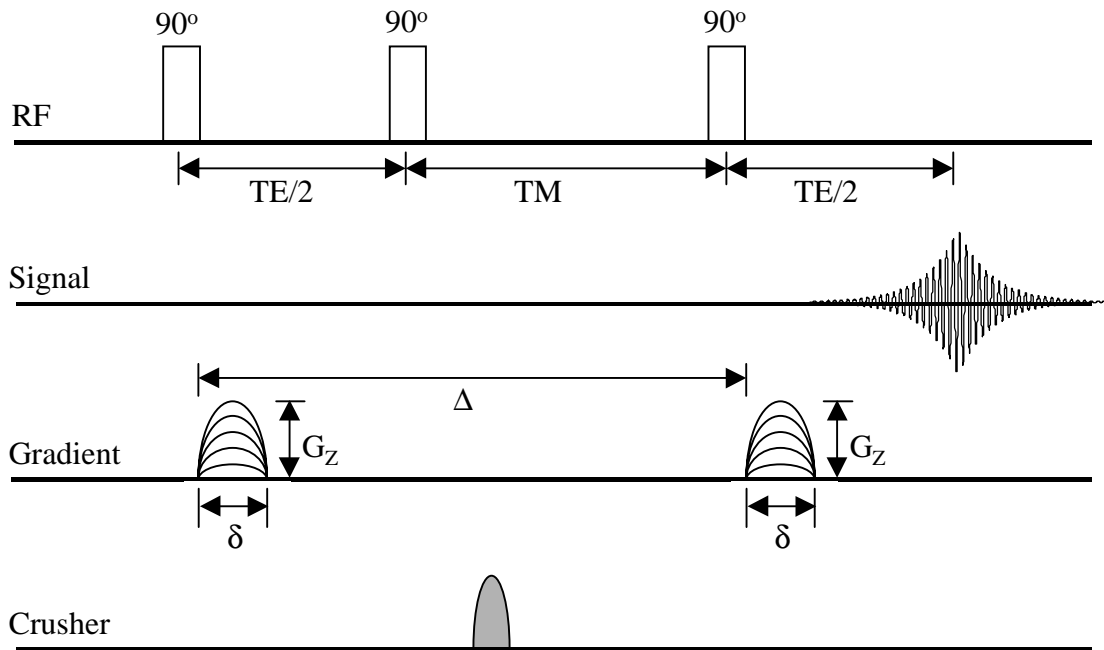


Figure 2.3.3.1: Diffusion-weighted stimulated-echo pulse sequence. The first 90° RF pulse flips the net magnetization in the transverse plane and the diffusion gradient is applied. The second 90° RF pulse stores half of the transverse magnetization along the longitudinal axis. The third 90° RF pulse returns the magnetization to the transverse plane after the time, TM. The second diffusion gradient pulse removes the phase imparted by the first diffusion gradient pulse. The crusher gradient during the TM period destroys any residual magnetization in the transverse plane and any spurious echoes.

results in a signal reduction by a factor of two. The third 90° RF pulse returns the longitudinal magnetization into the transverse plane for measurement. It is important to note that an echo is formed by any combination of two or more RF pulses. Depending on the timing within the pulse sequence, these spurious echoes can interfere with the desired

stimulated echo. One way to eliminate these spurious echoes without disturbing the stimulated echo is to insert a crusher gradient in the TM period. The crusher will dephase all residual transverse magnetization not stored along the longitudinal axis following the second 90° RF pulse.

2.4. Magnetic Resonance Imaging

2.4.1. Frequency Encoding

The basis of magnetic resonance imaging is the dependence of the precessional frequency on the magnetic field strength as expressed by the Larmor equation

$$\omega_0 = \gamma B_0. \quad [2.4.1.1]$$

In a uniform magnetic field, B_0 , all spins in a sample will precess at the same frequency, ω_0 . Inspection of the Larmor equation (Eq. [2.4.1.1]) shows that the precessional frequency can be altered by changing the magnetic field strength the spins are experiencing. If we add a magnetic field of magnitude, G , to the static magnetic field, B_0 , the precessional frequency is then

$$\omega = \gamma(B_0 + G). \quad [2.4.1.2]$$

Adding of a linear magnetic field gradient onto the static magnetic field will result in a

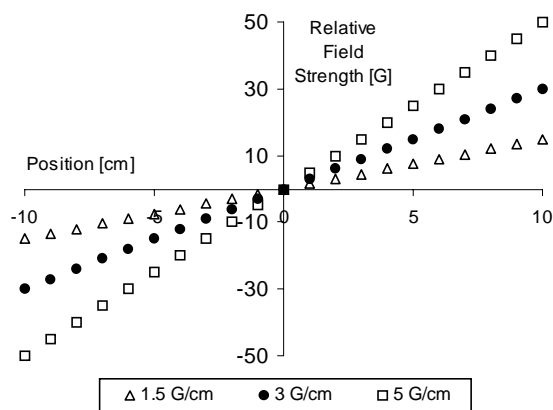


Figure 2.4.1.1: Spatial position as a function of the relative magnetic field strength. Application of a linear magnetic field gradient causes spins at different locations to precess at a frequency proportional to the field strength at their location.

change in the precessional frequency that is directly proportional to the magnetic field gradient. Since the field strength for a linear gradient is directly proportional to the spatial location, the resulting frequency can be related to a spatial location (Fig. 2.4.1.1). Hence spins at different locations along the direction of the gradient will precess at different frequencies. Data acquisition during

the application of the gradient results in a FID containing a range of frequencies which are related to the spatial location along the gradient orientation by

$$Location = \frac{Frequency}{\frac{\gamma}{2\pi} \times Gradient\ Slope} . \quad [2.4.1.3]$$

A Fourier transform of the FID reveals the different frequency components and allows the calculation of their spatial origin by Eq. [2.4.1.3] while the magnitude of the

frequency represents the relative contribution of the spins at this frequency to the signal (Fig. 2.4.1.2).

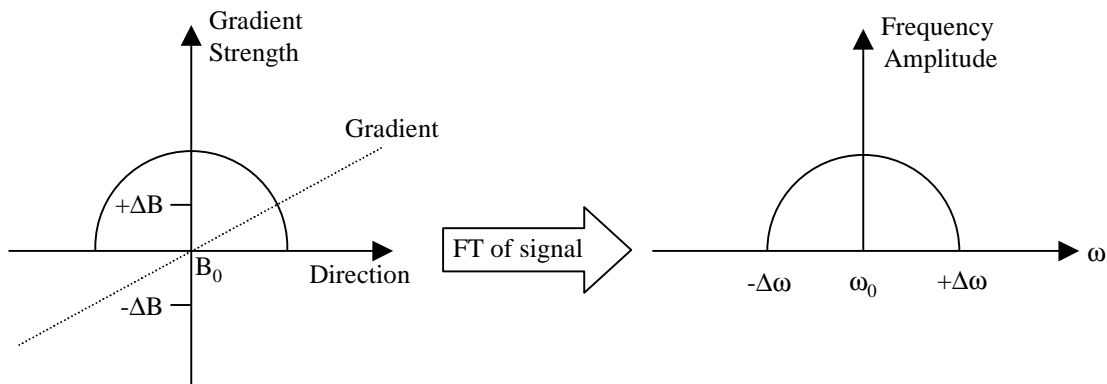


Figure 2.4.1.2: Placing a half spherical object in a magnetic field with a gradient causes spins in the center of the sphere to resonate at ω_0 and spins at the outer limits of the object to resonate at $\omega_0 - \Delta\omega$ and $\omega_0 + \Delta\omega$. The Fourier transform of the measured FID yields a frequency which corresponds to their spatial location and the magnitude of the frequency corresponds to the number of spins at that location which are contributing to the signal.

2.4.2. Phase Encoding

The NMR signal consists of an amplitude, frequency and phase. Since the magnitude contains information about the spin density and the frequency the spatial information in one dimension (Section 2.4.1) there is only the phase left to encode the second dimension with spatial information necessary for image reconstruction.

The application of a linear magnetic field gradient will cause the spins to precess at a frequency proportional to the field strength at their location. This behavior can be used to impart a phase to the spins which is proportional to their location in space. Application of a magnetic field gradient for a time, t_{phase} , will cause spins to precess at a higher or lower frequency than the Larmor frequency, ω_0 . During this time period, the spins accumulate a phase, Φ_r , with respect to ω_0 , which is dependent on the gradient strength, G_{phase} at their spatial location \vec{r} , and the time, t_{phase} , the gradient is applied, by

$$\Phi_{\vec{r}} = \gamma \int_0^{t_{phase}} [G_{phase}(t_{phase}) \vec{r}] dt_{phase} \quad [2.4.2.1]$$

where γ is the gyromagnetic ratio and the maximum phase accumulation, Φ_{max} , is then determined by the duration of the gradient.

The gradient used to impart the phase on the spins is known as the phase-encoding gradient and provides the spatial information in the second dimension necessary to reconstruct the image.

2.4.3 Slice Selection

In the above sections it was shown how a signal can be generated that contains all the

spatial information needed to create an image. Since we are seldom interested in an image of the entire sample, but rather a part of it, it becomes necessary to excite only the portion of the sample under investigation. The basic method in MRI used to select a certain part of the sample is based on the Fourier relationship between the time domain and frequency domain. By amplitude modulating the RF pulse in the time domain, it is possible to selectively excite specific locations in the frequency domain. In MRI we are commonly interested in a section with a rectangular slice profile. To excite such a section in the frequency domain the RF pulse in the time domain must be a sinc function (Fig. 1.6.5). A sine wave with a sinc envelope allows us to give the rectangular function in the frequency domain an offset equal to the frequency of the sine wave (see Section 1.6). Hence, in order to excite a rectangular profile of bandwidth $\Delta\omega$ in the frequency domain,

a RF pulse with a sinc envelope of $\frac{1}{2\Delta\omega}$ needs to be applied (Fig. 2.4.3.1).

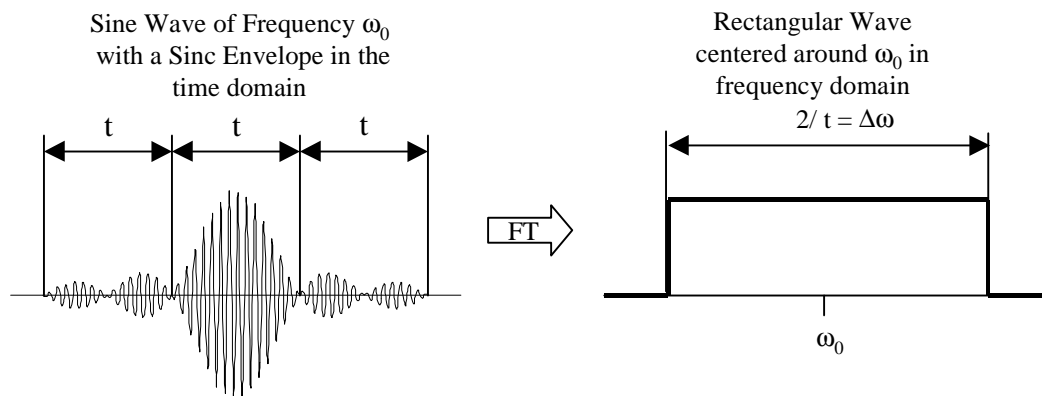


Figure 2.4.3.1: Fourier relationship between sinc function and rectangular function. The frequency of the sine wave contained in the sinc function (time domain) determines the offset of the rectangular function in the frequency domain. The bandwidth of the rectangular function is given by the sinc envelope.

For a sinc wave modulated with an RF frequency of ω_0 the excited bandwidth is

$$\omega_0 \pm \frac{\Delta\omega}{2}.$$

To achieve a perfect rectangular excitation profile, a sinc pulse with an infinite number of side lobes is necessary. Practical limitations prohibit such a sinc pulse and an approximation with three to five lobes is commonly used. The Fourier transform of such a truncated sinc pulse is a rectangular profile with ripples at the edges. These ringing artifacts are a direct result of the truncation of the high frequency components and can be neglected in most imaging experiments.

To achieve slice selection, a linear magnetic field gradient is applied at the same time as the sine wave with the sinc envelope. From Eq. [2.4.1.2], the superposition of a magnetic field gradient, G , onto the static magnetic field, B_0 , influences the Larmor frequency by

$$\omega = \omega_0 + \omega_G = \gamma(B_0 + G) \quad [2.4.3.1]$$

or we can express the change in frequency around ω_0 in terms of the change in field strength

$$\Delta\omega = \gamma\Delta G \quad [2.4.3.2]$$

Since the slice thickness is directly related to the frequency profile and the frequency is directly related to the gradient field strength, the slice thickness can be adjusted by simply varying the strength of the superimposed gradient, G , according to

$$\text{Slice Thickness} = \frac{\text{Frequency}}{\frac{\gamma}{2\pi} \times \text{Gradient Slope}} \quad [2.4.3.3]$$

Figure 2.4.3.2. illustrates the dependence of the slice thickness on the frequency profile (left side) and on the gradient strength (right side).

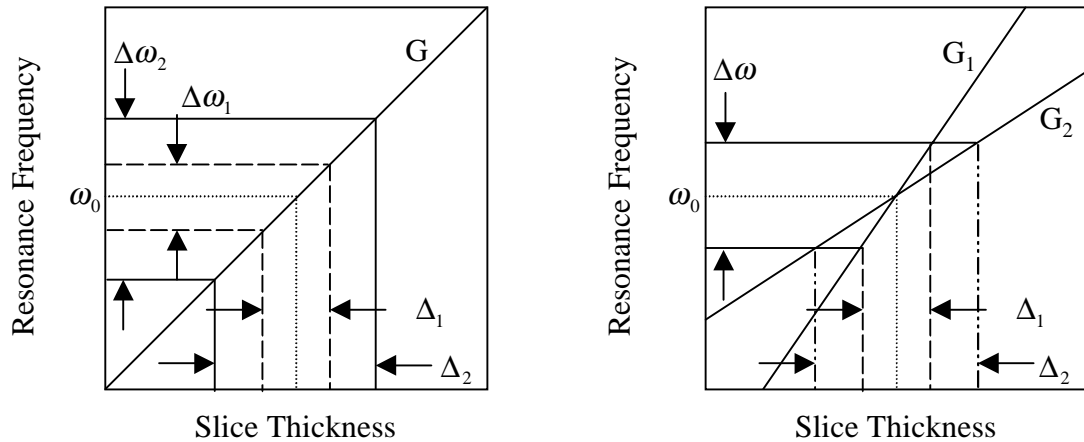


Figure 2.4.3.2: Effects of gradient strength and frequency bandwidth on the slice thickness. The left side shows the effects of the frequency bandwidth on the slice thickness. At a constant gradient strength, an increase in bandwidth results in a thicker slice. The right side illustrates the influence of the gradient strength on the slice thickness at a constant frequency bandwidth. As the gradient strength decreases the slice thickness increases.

A slice offset can be achieved by convolution of the RF sinc function with a sine wave of frequency, ω , while simultaneously applying a magnetic field gradient. Only spins along the magnetic field gradient precessing at a frequency that corresponds to the frequency of the sine wave contained in the RF sinc function will be excited. A change in slice offset is accomplished by changing the frequency of sine wave contained in the sinc function. The needed change of the RF center frequency can be calculated by

$$\Delta\omega = \gamma G \Delta x \quad [2.4.3.4]$$

where $\Delta\omega$ is the change of the sine wave frequency contained in the RF pulse, γ is the gyromagnetic ratio, G is the linear magnetic field gradient and Δx is the slice offset with respect to the isocenter of the magnet. This can be done by changing the transmitter frequency, ω_0 , to $\omega = \omega_0 + \Delta\omega$, or by a modulation of a sinc function containing a sine wave at the Larmor frequency, ω_0 , with a linear phase ramp in the time domain, where the maximum phase determines the slice offset.

2.4.4 *k*-Space and Imaging

Consider that the spins occupying a small volume element, dV , at position \vec{r} , and possess a spin density, $\rho(\vec{r})$, then the NMR signal arising from this volume element, dV , can be written as

$$dS(\vec{G}, t) = \rho(\vec{r}) dV e^{i\gamma(B_0 + \vec{G} \cdot \vec{r})t} \quad [2.4.4.1]$$

with \vec{G} is the applied magnetic field gradient for frequency encoding. Setting our receiver at the Larmor frequency, the so-called "on resonance" condition, we extract only the resulting the frequency difference imparted by the frequency-encoding gradient

$$\omega = \gamma \vec{G} \cdot \vec{r} \quad [2.4.4.2]$$

Integration over the volume element leads to the NMR signal in time domain

$$S(t) = \iiint_{dV} \rho(\vec{r}) e^{i\gamma \vec{G} \cdot \vec{r} t} d\vec{r} \quad [2.4.4.3]$$

which has the form of a Fourier transform. To make the Fourier relation more obvious the concept of a reciprocal space by a vector, \vec{k} , was introduced (Mansfield, 1975) where the space vector, \vec{k} , is defined as

$$\vec{k} = \frac{1}{2\pi} \gamma \vec{G} t \quad [2.4.4.4]$$

and has units of inverse space. The k space can be transversed by changing either the time or the gradient magnitude. Using Eqs. [2.4.4.3] and [2.4.4.4], the Fourier transform and the inverse Fourier transform of the imaging signal can be written, respectively, as

$$S(\vec{k}) = \iiint \rho(\vec{r}) e^{i2\pi\vec{k} \cdot \vec{r}} d\vec{r} \quad [2.4.4.5]$$

and

$$\rho(\vec{r}) = \iiint S(\vec{k}) e^{-i2\pi\vec{k} \cdot \vec{r}} d\vec{k} \quad [2.4.4.6]$$

Data acquisition in imaging mode is equivalent to a Fourier transform of the spin density, $\rho(\vec{r})$, and results in the measured signal, $S(\vec{k})$. An inverse Fourier transform (Eq. [2.4.4.6]) of the detected signal, $S(\vec{k})$, returns the spin density, $\rho(\vec{r})$, and allows the reconstruction of the image.

2.4.4.1 Spin-Echo Imaging

The conventional method to sample k space makes use of the phase- and frequency-encoding capabilities of the applied magnetic field gradients. The proportionality of the k -space vector, \vec{k} , with the gradient vector, \vec{G} , allows to move along one direction of the Cartesian k space, by simply incrementing the phase-encoding gradient. Application of

the frequency-encoding gradient orthogonal to the phase-encoding gradient allows encoding of a single line in k space. Repeating this process while simultaneously increasing the strength of the phase-encoding gradient, the two-dimensional k space can be traversed line by line (Figs. 2.4.41.1 and 2.4.4.1.2).

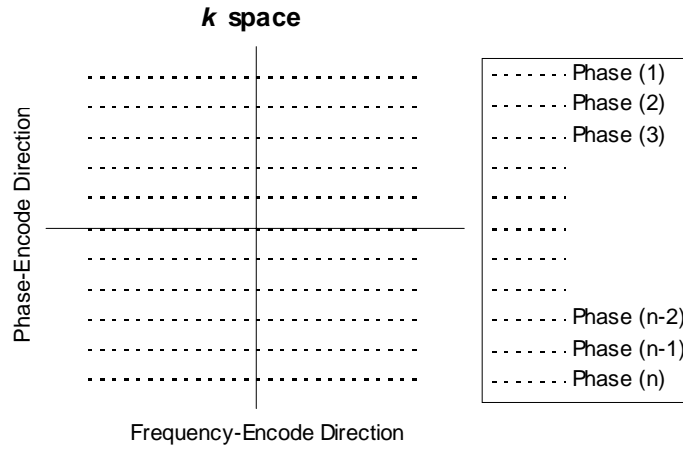


Figure 2.4.4.1.1: Conventional imaging of the k space. The phase-encoding gradient moves the k -space vector in one direction (vertical) and the frequency-encoding gradient sweeps across the horizontal line at the position of the phase-encoding gradient. By incrementing the phase-encoding gradient and repeating the frequency sweep along the horizontal line, the entire k space can be sampled.

The k -space signal acquired by such a MRI sequence is

$$S(k_x, k_y) = \int_{-\infty}^{\infty} \int_{-\infty}^{\infty} \rho(x, y) e^{i2\pi(k_x x + k_y y)} dx dy \quad [2.4.4.1.1]$$

where x is the location along the frequency-encoding direction, k_x , y is the location along the phase-encode direction, k_y , and $\rho(x, y)$ the spin density of the excited slice at the spatial location (x, y) . Image reconstruction is done by a two-dimensional Fourier transform of the data collected in k space.

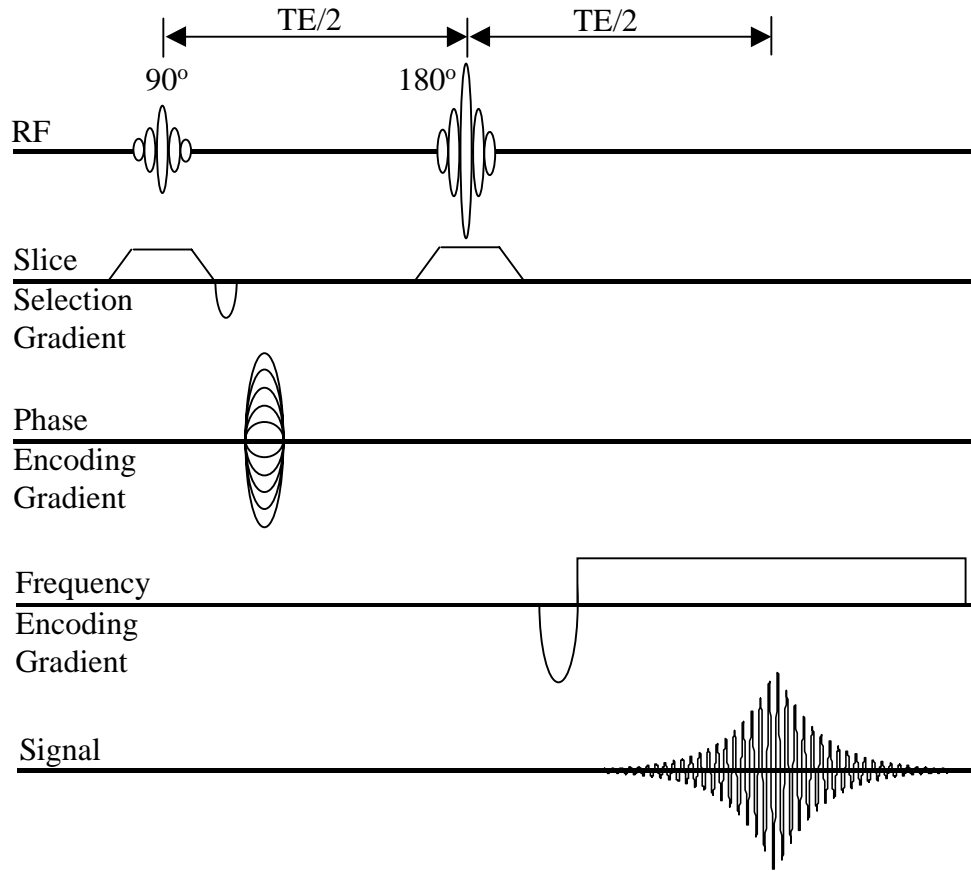


Figure 2.4.4.1.2: Spin-echo (SE) imaging pulse sequence. The RF sinc pulses are used to excite a rectangular slice profile and the slice select gradient determines the thickness of the imaging slice. The phase-encoding gradient imparts a phase to the excited spins and encodes spatial information into the signal in one dimension. The entire k space is sampled by incrementing the phase-encoding gradient for each line in k space and acquiring of the signal in the presence of the frequency-encoding gradient. Reconstruction of the image is done by a two-dimensional Fourier transform of the collected data.

2.4.4.2 Echo-Planar Imaging

A more time efficient technique than the line-by-line sampling of k space is known as echo-planar imaging (EPI). The simultaneous application of a broadening gradient, with an alternating gradient orthogonal to the broadening gradient, allows the sampling of the

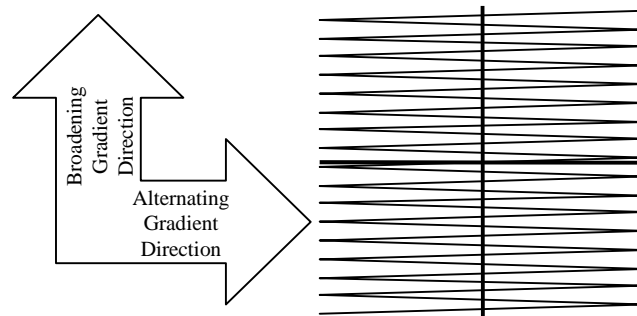


Figure 2.4.4.2.1: K -space trajectory for echo-planar imaging. The broadening gradient moves the wave vector linearly in the vertical dimension while the alternating gradient moves the wave vector horizontally in the second dimension.

two-dimensional k space in a single acquisition (Mansfield, 1977). The broadening gradient acts similar to the phase-encoding gradient in one dimension and the alternating gradient samples k space using a zig-zag pattern (Fig. 2.4.4.2.1).

Figure 2.4.4.2.2 shows a typical spin-echo EPI sequence and illustrates the simultaneous application of the gradients. The zig-zag sampling of the k space is a result of the concurrent application of the broadening gradient and the alternating gradient. Since the sweeping of the k space alters in direction, it becomes necessary to reverse the data in each alternating sweep before conventional, two-dimensional Fourier transform

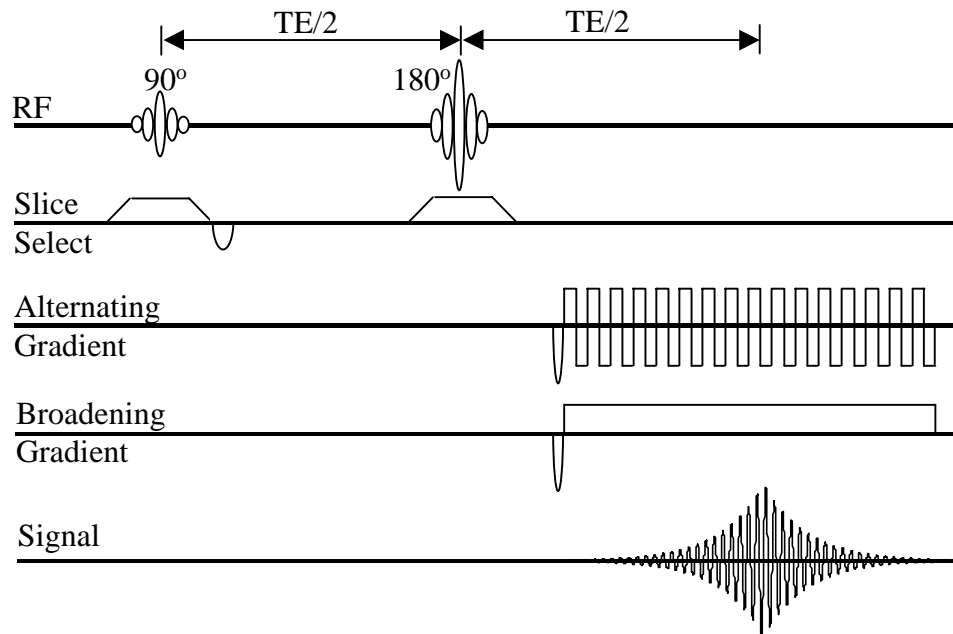


Figure 2.4.4.2.2: Spin-echo echo-planar imaging (SE-EPI) pulse sequence.

processing is performed. It should be noted, that only the data in the center of the acquisition window are T_2 weighted, while the remaining data have some T_2^* weighting.

Chapter 3

**The Return-to-the-Origin Probability and the ADC
of Water as Indicators of RIF-1 Tumor Necrosis**

3.0 The Return-to-the-Origin Probability and the ADC of Water as Indicators of RIF-1 Tumor Necrosis.

The objective of these experiments was to study structural changes in murine RIF-1 tumors in response to changes in necrotic volume, using two different NMR measures of water molecule displacement. One of the problems in this study was the immobilization of animals to avoid motion during the acquisition of the diffusion-weighted images. A new stereotaxic device, with an integrated headpiece for the administration of an inhalation anesthetic, was designed and built to ensure adequate immobilization of the animal during the NMR procedure. My contributions to the experiments were the design of the study, inoculation of the animal with tumor cells, data acquisition, and data analysis.

3.1 Introduction

The objective of this study was to compare the return-to-the-origin (RTO) probability and the apparent diffusion coefficient (ADC) of endogenous water molecules for their ability to detect tumor hypoxia and necrosis. Diffusion of water *in vivo* is highly influenced by the presence of local restrictions, such as cell membranes and organelles, and is therefore sensitive to changes in tissue structure and membrane permeability. This sensitivity has made diffusion-weighted MRI an early and reliable predictor of cerebral ischemia (Moseley, 1990). Recent studies of the diffusion coefficient in tumors (Zhao et al., 1995,

1996a) suggest that the diffusion coefficient is also sensitive to pathophysiological and structural changes in tumors.

Tumor vasculature consists of blood vessels recruited from the host vasculature and from angiogenesis in response to tumor cell growth (Jain, 1988). The distribution of nutrients and oxygen through the vasculature is governed by the flow rate (Less et al., 1991) and the vascular morphology (geometric arrangement, diameter, length, and number). Despite the similarities in the underlying mechanism of angiogenesis between the host vessel and the tumor (Patan et al., 1996), they are completely different with respect to organization. The vascular architecture of tumors differs significantly from the host organ and the flow rate of red blood cells is no longer dependent on the vessel diameter but is also orders of magnitudes lower (Jain, 1996). In normal healthy tissue, cell proliferation is coupled to angiogenic processes to ensure an adequate supply of oxygen and nutrients to the cells as well as the removal of cellular waste. The rapid cell proliferation in tumors causes the outgrowth of the vasculature and is often accompanied by defective angiogenesis. Cells in poorly vascularized and/or inadequately supplied regions of the tumor become oxygen deprived and subsequently necrotic.

Usually two types of hypoxia, which can be characterized by the underlying physiological processes, can be found in tumors and their occurrence in solid tumors has been confirmed by other researchers (Guichard et al., 1980; Moulder and Rockwell, 1984; Chapman, 1984). Chronic or "diffusion limited" hypoxia results from the limited distance that oxygen diffuses through tissue before it is metabolized. Thomlinson and

Gray (1955) have determined that the average distance oxygen diffuses in tissue before it is metabolized is approximately 150 μm and cells beyond this distance are generally poorly oxygenated. Since rapid cell proliferation in tumors can exceed the output of angiogenic processes, some population of cells within the tumor will become hypoxic as their distance from the vascular supply increases.

Acute or "perfusion limited" hypoxia is a result of impaired vasculature. Tumor cells suffering acute hypoxia are in close proximity to blood vessels which have transiently impaired blood flow due to stasis, flow reversal or collapsed vessels (Jain, 1988). The lack of oxygen results in decreased aerobic ATP synthesis due to reduced oxidative phosphorylation. For a short duration of time, anaerobic glycolysis can substitute for aerobic ATP synthesis with lactic acid as a byproduct. Anaerobic glycolytic ATP production can only be sustained over short periods of time before ATP synthesis ceases. Reduced ATP availability leads to decreased Na^+/K^+ -pump activity accompanied by the slow influx of Na^+ and Ca^{++} as well as efflux of K^+ . In response to the breakdown of the ion homeostasis, the cell tries to reduce the intracellular Na^+ concentration by allowing the influx of extracellular water. Loss of osmoregulation, therefore, results in cell swelling, dilation of endoplasmatic reticulum, mild swelling of the mitochondria, loss of microvilli, blebs, disaggregation of polysomes and aggregation of condensed chromatin around the nuclear periphery (Wyllie et al., 1980). Most of these changes are reversible if the cell is supplied with sufficient oxygen. Dying cells cross this "point of no return" and enter the second stage defined by severe swelling of mitochondria, nuclear pyknosis, cytoplasmic swelling, dissolution of cytoplasmic organelles and ruptured plasma

membranes (Wyllie, 1981). The necrotic cells are degraded by autolysis or immigrating leukocytes through lysosomal activity (heterolysis). This reduced oxygenation of tumor regions is of major importance in the treatment of cancer and has long been recognized as a determining factor in cancer therapy outcome (Thomlinson and Gray, 1955) as well as associated with therapeutic failure and reoccurrence (Horseman et al., 1986).

Diffusion-weighted NMR measures the net displacement of diffusing molecules caused by thermal energy (Brownian motion). The net displacement of molecules diffusing from

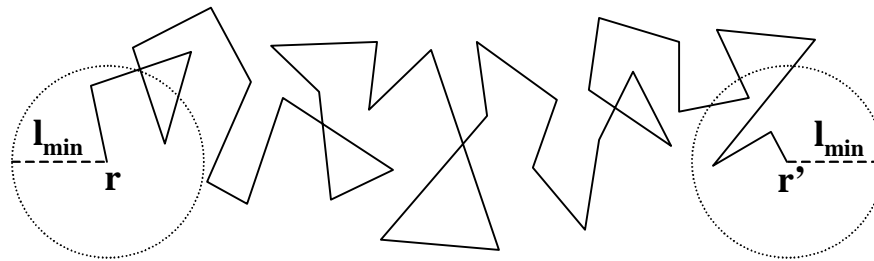


Fig. 3.1.1: Illustration of unrestricted diffusion due to thermal energy (Brownian motion). A molecule diffuses during the diffusion time, t_{diff} , from location r to location r' . The net displacement of the molecule during the diffusion time can be related to the self-diffusion coefficient by the Einstein relation. The dotted circles with radius l_{min} around the start- and endpoint are the uncertainty of the measured locations. The uncertainty is determined by the time needed to encode the initial and final positions.

location, r , to location, r' , (Figure 3.1.1) is related to the self-diffusion coefficient, D_0 ,

by the Einstein relation:

$$\langle (r - r')^2 \rangle = 2nD_0t \quad [3.1.1]$$

where $\langle (r - r')^2 \rangle$ is the ensemble averaged mean-squared displacement, n is the number of dimensions for which the displacement is measured and t is the time allowed for diffusion. The mean-squared displacement of an ensemble of diffusing molecules can be

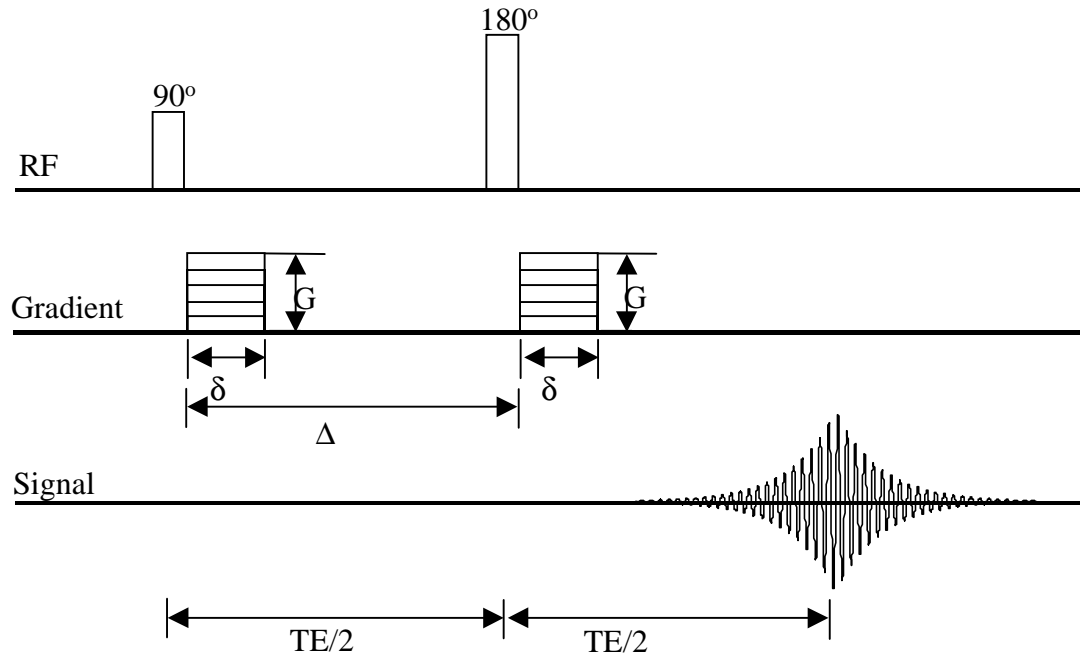


Figure 3.1.2: Stejskal-Tanner pulsed-field gradient spin-echo (PFGSE) pulse sequence where G is the applied gradient strength, δ is the gradient pulse duration, Δ is the diffusion-gradient separation time, and $TE/2$ is half of the echo time.

measured with the Stejskal-Tanner (1965) pulsed-field-gradient (PFG) pulse sequence (Fig. 3.1.2). Diffusing molecules are tagged at their initial position with a diffusion-gradient pulse and untagged at their endpoint by a second, equal diffusion-gradient pulse. Stationary molecules refocus after the echo time and do not attenuate the detected signal, since they do not gain any phase during the diffusion measurement. Molecules displaced by diffusion from their initial position will not refocus after the echo time, due to the random nature of the diffusion process, and thus have a residual phase. The acquired

phase manifests itself in an attenuation of the spin echo. For unrestricted diffusion the signal magnitude can then be written in accordance with Eq. [2.3.2.5] to be

$$M(\vec{k}, t) = M_0 e^{-\vec{k}^2 D_0 t} \quad [3.1.2]$$

where

$$\vec{k} = \gamma \vec{G} \delta, \quad [3.1.3]$$

M_0 is the signal measured without the presence of the diffusion gradient, D_0 is the self-diffusion coefficient, γ is the gyromagnetic ratio, δ is the diffusion-gradient pulse duration, \vec{G} is the applied diffusion-gradient strength, $t = (\Delta - \delta/3)$ is the diffusion time for rectangular diffusion gradients, and Δ is the diffusion-gradient separation. As Eq. [3.1.2] shows, measurement of the signal attenuation, at various values of the gradient strength allows the extraction of the self-diffusion coefficient from the linear slope of the $\ln(M/M_0)$ versus $k^2 t$ plot.

Because molecules can diffuse during the finite time used for tagging and untagging, their displacement has to be larger than the distance l_{min} (Fig. 3.1.1) to be detectable. The length of the distance, l_{min} , the uncertainty in the initial and final position, is inversely proportional to the gradient duration, δ , the gradient strength, \vec{G} , and therefore, \vec{k} .

$$l_{\min} = \frac{1}{k} = \frac{1}{\gamma \vec{G} \delta} \quad [3.1.4]$$

Early in the evolution of NMR diffusion measurements it was realized that in systems with barriers to diffusion or internal structures the measured diffusion coefficient deviates from that of bulk water (Woessner, 1963; Stejskal and Tanner, 1968). An example of this is shown in Fig. 3.1.3. The deviation from the diffusion coefficient, D_0 , of bulk water

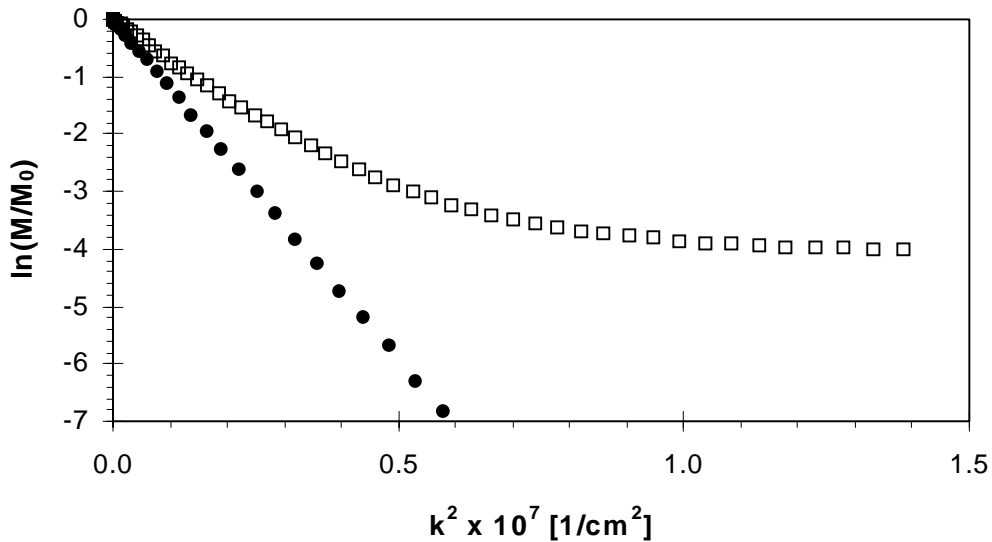


Figure 3.1.3: Plot of the attenuation curves $\ln(M/M_0)$ versus k^2 for freely diffusing water (●) and water diffusing in the interstitial space of a polystyrene bead pack (□) (from Helmer et al., 1995). The data were acquired using a Stejskal-Tanner pulse sequence with $\Delta = 50$ ms, $\delta = 1.5$ ms and a maximum applied diffusion-gradient strength, G , of 72.8 G/cm.

depends on the amount of restrictions diffusing water molecules encountered during the diffusion time, t . As the diffusion time increases, more molecules will experience some kind of restriction thereby reducing the ensemble average of the mean-squared displacement (Fig. 3.1.4) with respect to freely diffusing water. Equation [3.1.2] no

longer strictly applies (Tanner and Stejskal, 1978) in the restricted case since the measured diffusion coefficient depends upon the number of barriers encountered and hence upon the diffusion time. To indicate this deviation from the bulk diffusion coefficient the measured diffusion coefficient is now written with an explicit dependence upon the diffusion time and is also referred to as the apparent diffusion coefficient

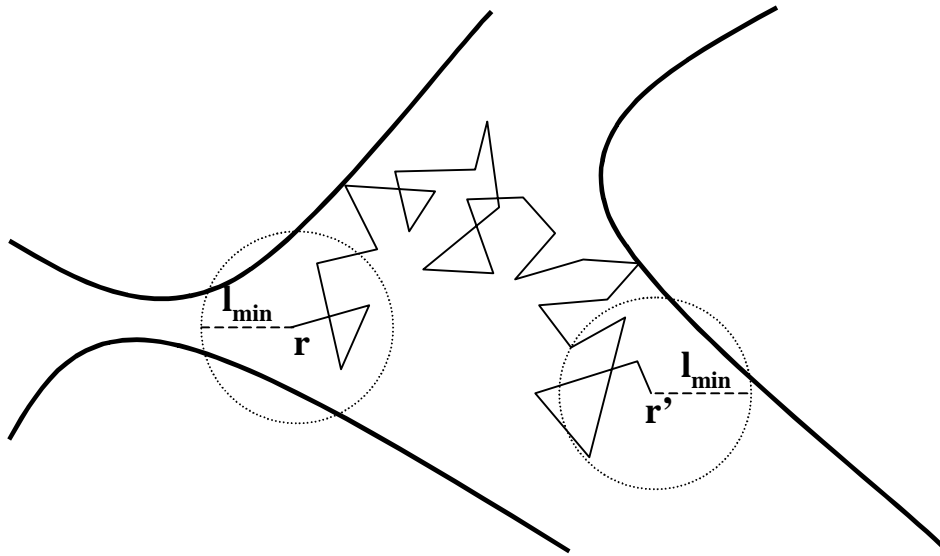


Fig. 3.1.4: Illustration of diffusion in the presence of diffusion barriers. The diffusion barriers encountered during the movement from location r to location r' reduce the net displacement of the diffusing molecule. The dotted circles with radius l_{min} around the start and endpoint are the uncertainties in r and r' which are determined by the time needed to encode the initial and final positions.

(ADC). For very short diffusion times, only molecules within a distance shorter than the diffusion length

$$l_d \sim \sqrt{D_0 t} \quad [3.1.5]$$

will experience diffusion barriers and hence are sensitive to restrictions (Latour et al.,

1993). These will be few in number and other molecules will not experience any restrictions. The measured diffusion coefficient, $D(t)$, will therefore be close to the bulk diffusion coefficient, D_0 . In this case, for small k values, Eq. [3.1.2] can still be used by assuming that the diffusion coefficient, D , is now a function of the diffusion time, t (Woessner, 1963). Modification of Eq. [3.1.2] to account for the time-dependent diffusion coefficient yields

$$M(k, t) = M_0 e^{-k^2 D(t) t}. \quad [3.1.6]$$

In this regime, the time-dependent diffusion coefficient, $D(t)$, reflects the local properties

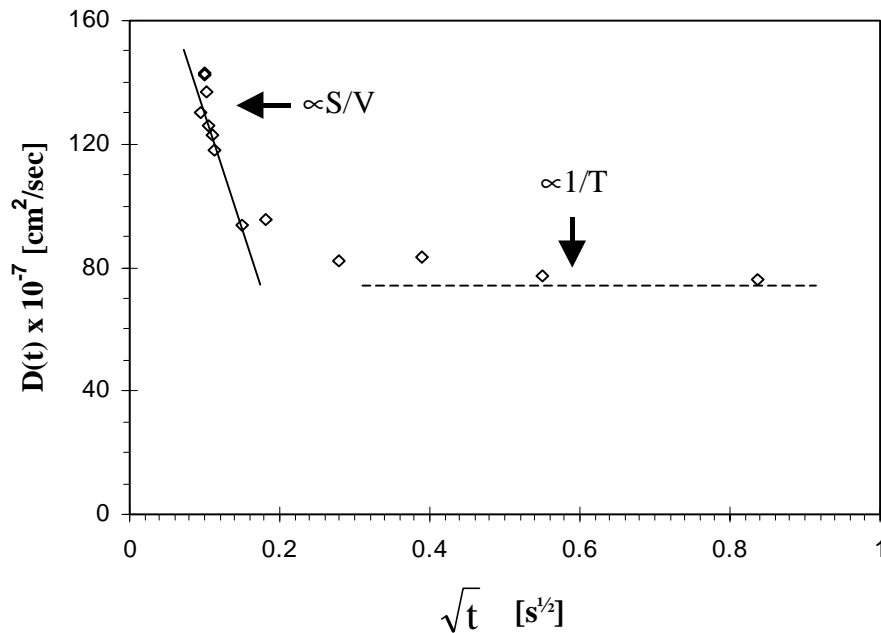


Figure 3.1.5: Plot of the measured diffusion coefficient versus the square-root of the diffusion time for a RIF-1 tumor with a volume of 1.5 cm³ (Helmer, 1999). The surface-area to volume ratio, S/V , can be calculated from the initial slope of the curve and the tortuosity, T , can be extracted from the plateau region of the curve.

of the sample, such as the average surface-area to volume ratio (Mitra et al., 1992; Mitra et al., 1993; Latour et al., 1993). The initial slope of the time-dependent diffusion coefficient, $D(t)$, versus the square-root of the diffusion time curve (Fig. 3.1.5), is related to the average surface-area to volume ratio, S/V , by (Mitra et al., 1992)

$$\frac{D(t)}{D_0} = 1 - \frac{4}{9\sqrt{\pi}} \frac{S}{V} \sqrt{D_0 t} + \vartheta(t). \quad [3.1.7]$$

As the diffusion time increases, more diffusing molecules will encounter restrictions, reducing the average displacement. One way to explain the behavior of the time-dependent diffusion coefficient, $D(t)$, in the long time regime is the use of a common morphology (Calaghan, 1991). By dividing the diffusion space into subregions, each of the individual regions would display a diffusion coefficient at short diffusion times according to

$$\frac{M(k, t)}{M_0} = e^{-k^2 D(t)t} \quad [3.1.8]$$

and the measured magnetization is the superposition of the individual subregions, n , with their diffusion coefficient, $D_n(t)$ and weighting p_n .

$$\frac{M(k, t)}{M_0} = \sum_n \frac{M_n(k, t)}{M_{0n}} = \sum_n e^{-k^2 D_n(t)t} \quad [3.1.9]$$

Increasing the diffusion time will allow more molecules to diffuse into restricting boundaries thereby reducing their diffusion coefficient with respect to the bulk value. If the diffusion time is sufficiently long to allow all the molecules to probe the entire diffusion space, they would all encounter the same number of diffusion barriers and hence their mean-squared displacement will be equal. The equal mean-squared displacement of the subregions yields a similar diffusion coefficient, $D_n(t) = D_{eff}$, for all regions and Eq. [3.1.9] can be rewritten to be

$$\frac{M(k,t)}{M_0} \Big|_{t \rightarrow \infty} = e^{-k^2 D_n(t)t} \Big|_{t \rightarrow \infty} = e^{-k^2 D_{eff} t} \quad [3.1.10]$$

where D_{eff} is the effective diffusion coefficient of the sample characterizing the average or "effective" properties of the medium in which the molecules are diffusing.

The application of some ideas from porous media theory to biological samples can provide a model to extract structural information from the time-dependent diffusion coefficient (Latour et al., 1994). At long diffusion times the bulk diffusion coefficient, D_0 , of water molecules diffusing in the pore space of a porous medium is reduced by the tortuosity, T , of the medium (Johnson et al., 1982; Haus and Kehr, 1987; Nicholson and Rice, 1991) to D_{eff} as described by the relation

$$D_{eff} = \frac{D_0}{T}. \quad [3.1.11]$$

In biological tissue, with intra- and extracellular compartments, the diffusing molecules can diffuse across the cell membrane separating the intra- and extracellular space. To account for this additional pathway the definition of the tortuosity has to be modified to include the membrane permeability. The validity of these ideas has been successfully shown in packed erythrocytes (Latour et al., 1994) and applied to biological systems such as rodent tumors (Helmer et al., 1994, 1995).

Crick (1970) derived the membrane permeability of cells from the effective diffusion coefficient using a simplified model, with a large concentration gradient over many cells with equal diameter, and found the following relationship:

$$\frac{1}{D_{eff}} = \frac{1}{D_0} + \frac{1}{\kappa a}, \quad [3.1.12]$$

where D_0 is the diffusion coefficient of freely diffusing water, D_{eff} is the effective diffusion coefficient at long diffusion times, κ is the permeability, and a the length of each cell in the direction of diffusion. Equation [3.1.12] demonstrates how structural properties such as cell membrane permeability and geometrical properties like cell dimensions, can alter the effective diffusion coefficient. However, this model is incomplete since it does not account for the compartments with different diffusion coefficients, parallel diffusion pathways around diffusion barriers, and differences in the water concentration between different compartments. A more complete model has been put forth by Latour et al. (1994) that accounts for these parameters.

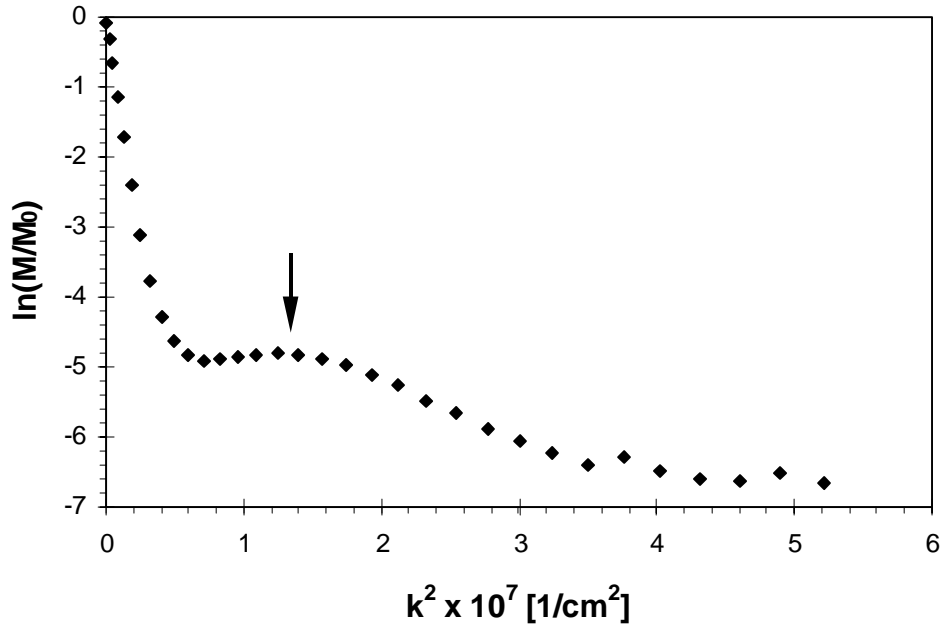


Figure 3.1.6: Plot of the signal attenuation $\ln(M/M_0)$ versus k for a monosized sphere pack acquired at a $\Delta = 100$ ms and a bead diameter of $15.8 \mu\text{m}$ (Helmer 1999). The displayed diffraction peak marked by the arrow.

In samples with well-defined periodic geometries and connections between different sample regions, diffusing molecules can move to adjacent regions. For a certain value of k , molecules moving to an adjacent region will have acquired the same phase as those molecules that started in the initial region. This phase coherence will manifest itself as a peak in the measured signal (Fig. 3.1.6), which is often termed a "diffraction peak" in analogy to light scattering. The location of the diffraction peak is determined by the magnitude of \vec{k} (Eq. 3.1.3), and the structural length, a , (Callaghan et al., 1991, 1992) as given by:

$$ka = 2\pi \quad [3.1.13]$$

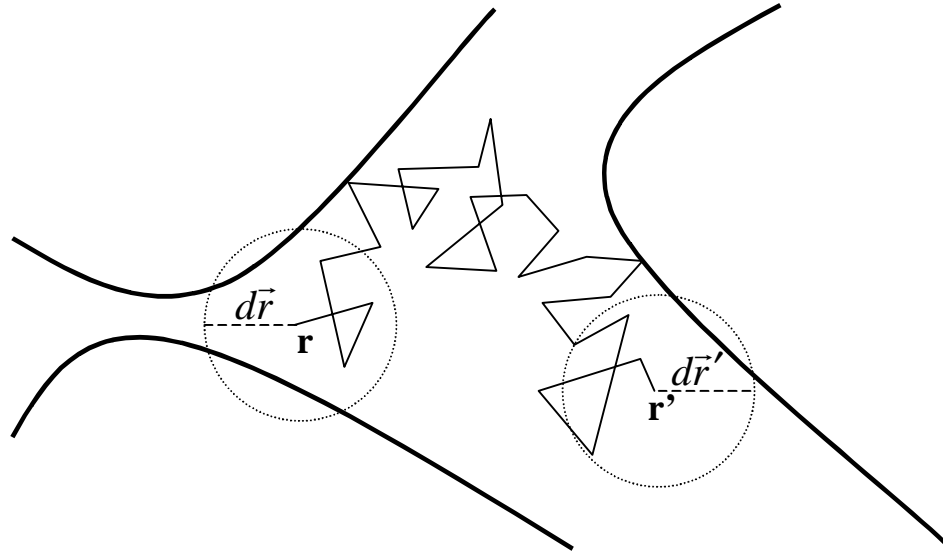


Figure 3.1.7: Illustration of diffusion in the presence of barriers. The barriers encountered during movement from location \vec{r} , to \vec{r}' decrease the mean-squared displacement but increase the probability that the molecule will be found within the sphere of radius $d\vec{r}'$, after diffusing for a time, t .

In systems consisting of many different structures of varying length scales, no diffraction peaks can be observed, since there is no repeating geometrical structure (Mitra et al., 1995) and the information contained in the diffraction peaks are no longer obtainable. However, structural information can still be extracted from this type of data by calculation of the return-to-the-origin probability.

The return-to-the-origin (RTO) probability measures the probability that a diffusing water molecule starting within a sphere of radius $d\vec{r}$ around \vec{r} will be found in the same sphere of radius $d\vec{r}'$ around \vec{r}' (Fig. 3.1.7) after diffusing for a time, t . The radius dr is equal to l_{\min} as defined in Eq. [3.1.14] and is the minimum resolution of the RTO measurement.

To calculate the RTO probability in a pulsed-field-gradient NMR experiment, we start with the measured signal, which can be expressed in terms of the diffusion propagator:

$$M(\vec{k}, t) = \int_V e^{i\vec{k} \cdot (r-r')} G(\vec{r}, \vec{r}', t) \rho(\vec{r}') d\vec{r} d\vec{r}' \quad [3.1.14]$$

where $\rho(\vec{r}')$ is the proton density at \vec{r}' , $G(\vec{r}, \vec{r}', t)$ is the diffusion propagator, $M(\vec{k}, t)$ is the measured signal which depends on the diffusion time and \vec{k} . The diffusion propagator (Mitra et al., 1992) has to satisfy the diffusion equation

$$\frac{\partial G(\vec{r}, \vec{r}', t)}{\partial t} = D_0 \nabla^2 G(\vec{r}, \vec{r}', t) \quad \text{for } t > 0 \quad [3.1.15]$$

where D_0 is the bulk diffusion coefficient and

$$G(\vec{r}, \vec{r}', t = 0^+) = \delta(\vec{r} - \vec{r}') \quad [3.1.16]$$

starts at position \vec{r} , moves to position \vec{r}' during the time, t , larger than zero.

The probability that a diffusing molecule starting within a sphere of radius $d\vec{r}$ around \vec{r} , will be found in a sphere of radius $d\vec{r}'$ centered around \vec{r}' , after diffusing for a time, t , can be mathematically expressed by the conditional probability, $P(\vec{r} | \vec{r}', t)$. The

conditional probability, $P(\vec{r} | \vec{r}', t)$, can be expressed in terms of the diffusion propagator, $G(\vec{r}, \vec{r}', t)$, and the spin density, $\rho(\vec{r})$, as

$$P(\vec{r} | \vec{r}', t) = G(\vec{r}, \vec{r}', t) \rho(\vec{r}') d\vec{r} d\vec{r}'. \quad [3.1.17]$$

and it can be seen that the measured signal, Eq. [3.1.14], is therefore a function of the conditional probability. Substituting Eq. [3.1.17] into Eq. [3.1.14] and integrating over all initial and final positions yields the RTO probability

$$P(t) = \frac{1}{(2\pi)^3} \int M(\vec{k}, t) d\vec{k} \quad [3.1.18]$$

with

$$P(t) = \int P(\vec{r} | \vec{r}', t) d\vec{r}' = \int G(\vec{r}, \vec{r}', t) \rho(\vec{r}') d\vec{r}' \quad [3.1.19]$$

for the RTO probability averaged over all positions. For molecules diffusing in homogeneous media, Eq. [3.1.18] can be rewritten to be

$$P(t) = \frac{1}{(2\pi)^2} \int_0^\infty M(k, t) k^2 dk. \quad [3.1.20]$$

Since it is not possible to have an infinitely large k , the data are integrated up to the largest possible value of k , k_{max} , and the RTO probability becomes a function of time and k_{max} .

$$P(t, k_{max}) = \frac{1}{(2\pi)^2} \int_0^{k_{max}} M(k, t) k^2 dk \quad [3.1.21]$$

The RTO probability is proportional to the area under the attenuation curve (Fig. 3.1.8) $\ln(M/M_0)$ versus k . Figure 3.1.8 shows examples of the measured signal for the calculation of the RTO probability obtained from a Cutbank 26 mudstone rock core at varying diffusion times (Helmer, 1999). For small values of k , the signal is comprised from restricted and unrestricted water molecules, while at large values of k the signal arises from only from highly restricted water molecules. At large k values, the measured

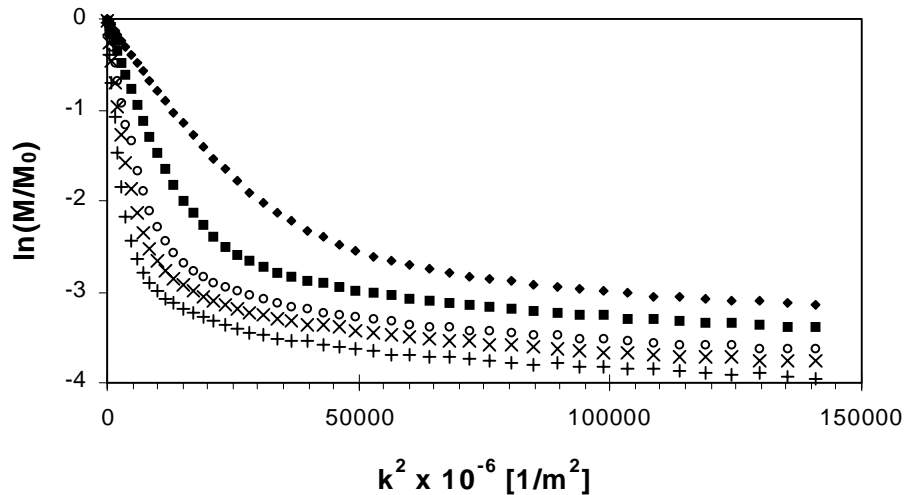


Figure 3.1.8: Plots of the magnetization $\ln(M/M_0)$ versus k for a Cutbank 26 mudstone rock core at varying diffusion times of 25 (◆), 75 (■), 175 (○), 275 (×) and 275 (+) ms (Helmer, 1999).

signal arises from restricted spins, whose diffusion coefficient is low. Inspection of Eq. [3.1.21] shows that the measured signal is weighted by k^2 and therefore the RTO probability is most sensitive to the signal arising from restricted water molecules.

For the case of unrestricted diffusion, analytical solution of Eq. [3.1.20] yields

$$P_0(t) = \frac{1}{(4\pi D_0 t)^{3/2}}. \quad [3.1.22]$$

Normalizing the RTO probability to the volume of the sphere results in the dimensionless probability,

$$F(t, \vec{k}_{\max}) = \frac{3}{k_{\max}^3} \int_0^{k_{\max}} M(\vec{k}, t) \vec{k}^2 d\vec{k}, \quad [3.1.23]$$

which is independent of the length scale. The normalized RTO probability, $F(t)$, is denoted as the absolute RTO probability to distinguish it from the RTO probability, $P(t)$, which is expressed in units of the inverse length scale. Figure 3.1.9 shows a plot of the absolute probability, F , versus $1/k$ calculated for the data in Fig. 3.1.8. It is apparent from Fig. 3.1.9, that for a sphere of large radius in which the diffusing spins never leave the sphere around their initial position the probability, F , is 1. As the radius of the sphere decreases, the probability that diffusing molecules will be found within the sphere or have never left their sphere of origin also decreases. Therefore, the set of curves all

decrease as l_{min} ($=1/k$) decreases in Fig. 3.1.9. As the diffusion time increases, molecules are allowed to move larger distances thereby decreasing their probability to be found near the initial position. This latter behavior can be seen in Fig. 3.1.9 as F decreases with

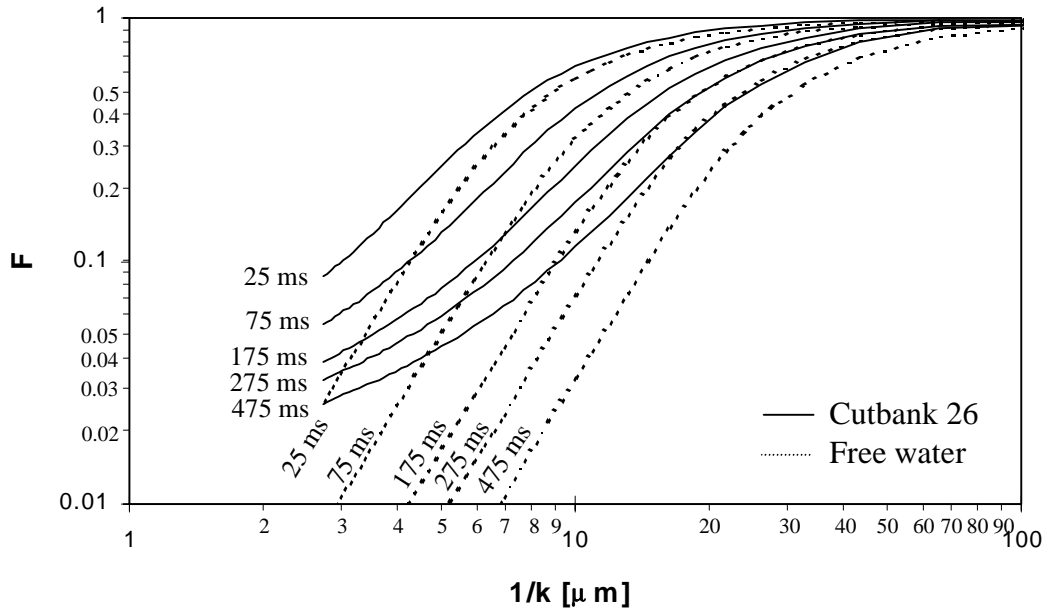


Figure 3.1.9: Plot of the absolute RTO probability, F , versus $1/k$ for water diffusing in the pore space of a Cutbank 26 mudstone rock core (—) calculated from the data shown in Fig. 3.1.8 and free water (.....) for varying diffusion times of 25, 75, 175, 275 and 475 ms (Helmer, 1999).

increasing diffusion times. The curves of freely diffusing water (dashed line in Fig. 3.19) shows a lower absolute RTO probability than the curves of the Cutbank 26, at the same diffusion time. This enhancement of restricted diffusion over bulk diffusion is expressed by the RTO enhancement.

The RTO enhancement is the normalization of the RTO probability by that of free diffusion and, like the absolute RTO probability, is dimensionless and not dependent on

the length scale of the measurement

$$R(t) = \frac{P(t)}{P_0(t)} = (4\pi D_0 t)^{3/2} P(t). \quad [3.1.24]$$

Using the maximum value of $\vec{k} = \vec{k}_{\max}$, the RTO enhancement can also be written as

$$R(t, \vec{k}_{\max}) = \frac{P(t, \vec{k}_{\max})}{P_0(t, \vec{k}_{\max})} = \frac{\frac{1}{(2\pi)^2} \int_0^{k_{\max}} M(\vec{k}, t) \vec{k}^2 d\vec{k}}{4\pi \int_0^{k_{\max}} e^{-D_0 \vec{k}^2 t} \vec{k}^2 d\vec{k}} \quad [3.1.25]$$

which describes how much more probable it is that a diffusing molecule encountering restricting barriers returns to its sphere of origin as compared to a molecule diffusing in a bulk, unrestricted solution. Figure 3.1.10 shows the RTO enhancement over freely diffusing water for the data shown in Figs 3.1.8 (signal magnitude) and 3.1.9 (absolute RTO probability, F). The plot demonstrates that there is no enhancement for a sphere with a very large radius, since water molecules cannot leave the sphere origin. For a sphere of small radius, molecules diffusing in a restricted environment are more likely to be found with the sphere after diffusing for a time, t , than water molecules diffusing in a bulk solution. Therefore, the RTO enhancement increases with decreasing sphere radius. For long diffusion times, there is an increase in the RTO probability since the RTO probability of free diffusing water molecules decreases faster than the RTO probability of

highly restricted spins, with their limited displacement.

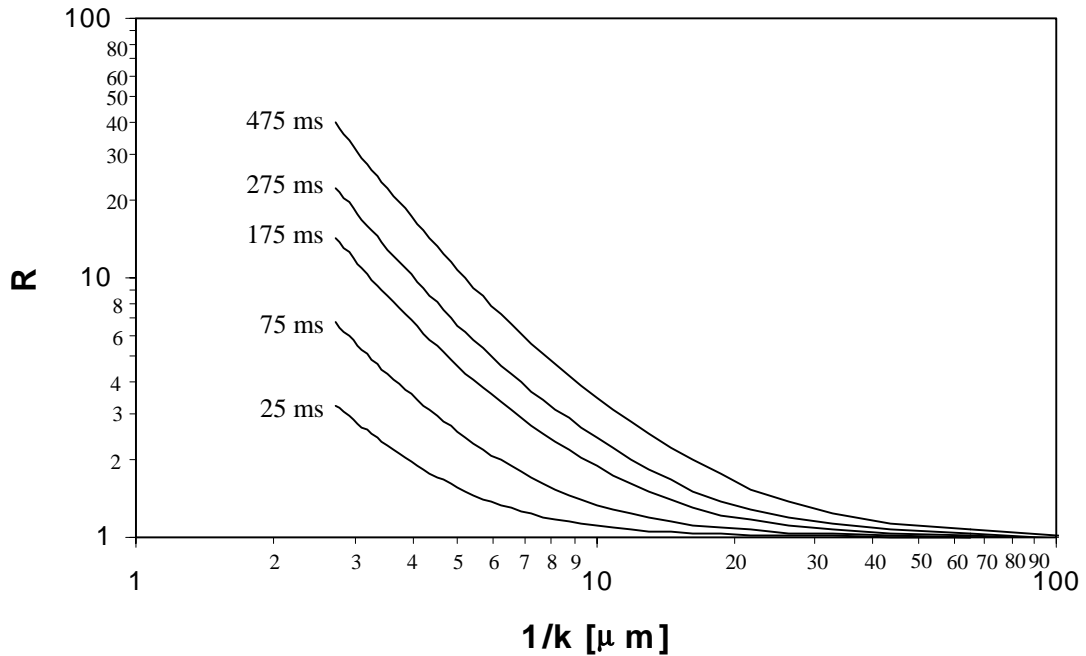


Figure 3.1.10: Plot of the RTO probability enhancement, R , versus $1/k$ of water diffusing in the pore space of a Cutbank 26 mudstone rock core (raw data shown in Fig. 3.1.8) at diffusion times of 25, 75, 175, 275 and 475 ms (Helmer, 1999). The enhancement is the quotient of the RTO probabilities of the rock sample and free water.

3.2 Experimental Methods

3.2.1 Animal Preparation

All experiments and procedures were approved by the Animal Research Committee (ARC) of the University of Massachusetts Medical School. Animals were housed under diurnal lighting conditions and allowed free access to food and water before and after

imaging. Eight-week old, female C3H mice (Taconic Farms, Germantown, NJ) were anesthetized by intraperitoneal injection of 60 mg/kg sodium pentobarbital (Abbott Laboratories, Chicago, IL). For the spectroscopy and imaging NMR experiments, the lower back and right hind leg were shaved and the remaining hair removed with a commercial hair remover (NAIR, Carter Wallace Inc., New York, NY).

Radiation-induced-fibrosarcoma, RIF-1 (Twentyman et al., 1980), cells from a second passage, suspended in Waymouth's medium supplemented with 15 % v/v fetal bovine serum (FBS) and 10 % v/v glycerol, were stored in liquid nitrogen. Prior to inoculation, the frozen cells were defrosted at room temperature and 0.15 ml of the suspension containing $\sim 1 \times 10^5$ cells were subcutaneously injected in the lower back or right hind leg with a 30-gauge hypodermic needle. RIF-1 tumors were allowed to grow to a range of volumes (0.4 to 2.1 cm³) in order to obtain varying necrotic volumes. The tumor volume was determined by measuring the three major orthogonal axes with slide calipers. The volume was calculated to be

$$Volume = \frac{\pi}{6} \times Length \times Width \times Height \quad [3.2.1.1]$$

assuming an ellipsoidal volume (Euhus et al., 1986; Tomayko and Reynolds, 1989)

For data acquisition, anesthesia was induced with 2% isoflurane delivered in air at 1.5 l/min and maintained at 1.5% isoflurane at the same flow rate. The body temperature

was maintained at 37° C by circulating 34° C warm air through the stereotaxic holder, controlled with a T-type temperature probe (Omega, Stamford, CT) and a two-point feedback system.

3.2.2 NMR Measurements

Data were acquired using a horizontal bore GE CSI-II 2.0 T 45-cm imaging spectrometer operated at 85.56 MHz, equipped with ± 20 G/cm self-shielded gradients and a four-turn solenoidal RF coil with an inner diameter of 15 mm for spectroscopy and 18 mm for imaging.

NMR Spectroscopy:

A total of ten animals was used for the spectroscopic measurement of the RTO probability and enhancement. To avoid the influence of susceptibility gradients from large blood pools (sometimes present in tumors) on the measurement of the diffusion coefficient and to achieve large k values with short diffusion gradient duration, the RTO probability was measured spectroscopically with a modified pulsed-field-gradient stimulated-echo pulse sequence (Latour et al., 1993a) designed to cancel any effects of internal gradients (Fig. 3.2.2.1). The cancellation was achieved by separating pairs of gradient pulses with opposite polarity by 180° RF pulses in each of the TE/2 time periods. Five pairs of diffusion gradients were used with a diffusion-gradient duration of 1.5 ms. The diffusion gradients were successively incremented in 0.3 G/cm steps from 0.3 to 15 G/cm. Data were acquired over a range of five different diffusion times (42, 92,

192, 292, and 492 ms) with a spectral width, $SW = \pm 2000$ Hz, signal averages, $NEX = 4$, and 2048 data points.

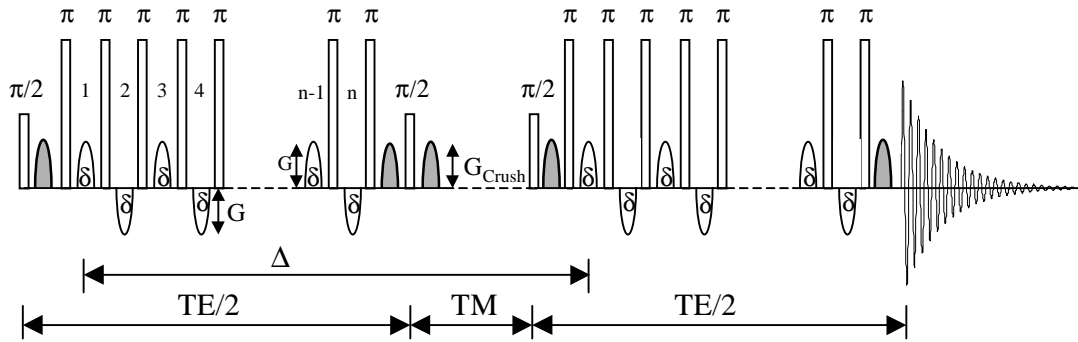


Figure 3.2.2.1: Modified pulsed-field-gradient stimulated-echo pulse sequence. Pairs of gradient pulses are applied separated by 180° RF pulses to cancel the effects of internal gradients on the diffusion measurement. The diffusion gradients have a duration of δ and an amplitude of G . Crusher gradients, used to destroy any unwanted magnetization and spurious echoes, are displayed in shaded gray. The sequence is based on a stimulated-echo pulse sequence and supplemented with π pulses to reduce the exposure of spins to the internal gradient fields.

NMR Imaging:

A total of fourteen animals were used for the NMR imaging study and two animals, with a large disagreement between the geometric shape of the imaging slice and the histology slice, were excluded from the analysis. The coronal plane for image acquisition was located at a constant offset of 3.0 mm with respect to the isocenter of the instrument to avoid image acquisition in the area of the underlying muscle tissue. The animals were immobilized in the stereotax, which ensured a relatively reproducible position in the bore of the magnet.

Coronal, diffusion-weighted, stimulated-echo echo-planar images were acquired with a field of view, FOV = 30.0 mm, a 64×64 in plane resolution, a slice thickness of 3.0 mm, a repetition time, TR = 6 s, number of averages, NEX = 4, an echo time of 56.0 ms, and a spectral width, SW = ± 70 KHz. Diffusion gradients were incremented in 32, 0.6 G/cm steps, from 0.0 to 18.6 G/cm. The diffusion time was 201.5 ms with half-sine-shaped diffusion-gradient pulses of duration, $\delta = 7.0$ ms. T₂-weighted images of the same slice were acquired at nine different echo times (10, 20, 40, 60, 80, 100, 150, 200, and 300 ms) with the same imaging parameters as the diffusion-weighted images.

3.2.3 Histology

Immediately following the NMR experiment, the animal was sacrificed by cervical dislocation. The tumor was excised and stored in formalin for fixation. Hematoxylin and eosin (H&E) staining, for the detection of viable and necrotic tumor tissue, was performed on the fixated neoplasms. For the spectroscopy experiment, a slice through the center of the RIF-1 tumor was chosen for histology. In the case of the imaging study, three slices (located at the top, center and bottom of the corresponding MRI slice) were selected for histology. The stained histology slices had a thickness of 5 μm for both experiments.

3.2.4 Data Analysis

NMR Spectroscopy:

The RTO probability was calculated from the measured signal, $M(\vec{k}, t)$, using Eq. [3.1.20]

$$P(t, k_{\max}) = \frac{1}{(2\pi)^2} \int_0^{k_{\max}} M(\vec{k}, t) \vec{k}^2 d\vec{k} \quad [3.2.4.1]$$

with

$$\vec{k} = n\gamma G\delta\left(\frac{2}{\pi}\right), \quad [3.2.4.2]$$

where G is the applied diffusion-gradient strength, γ is the gyromagnetic ratio, δ is the diffusion-gradient duration, n the number of diffusion-gradients applied, and $(2/\pi)$ the geometric correction factor for half-sine-shaped diffusion gradients. The absolute RTO probability, $F(\vec{k}, t)$, and the RTO enhancement, $R(\vec{k}, t)$, were then calculated from $P(\vec{k}, t)$ using Eqs. [3.1.23] and [3.1.25], respectively.

NMR Imaging:

As discussed earlier, for small k values, the slope of the signal attenuation curves is linear and deviates little from the Gaussian diffusion behavior. A previous study (Helmer et al.,

1995) found that the diffusion attenuation curves of RIF-1 tumors start to deviate from linearity at a normalized signal attenuation $\ln(M(\vec{k},t)/M_0)$ greater than approximately 20%. Hence the apparent diffusion coefficient (ADC) maps were calculated on a pixel-by-pixel basis from the initial slope of the $\ln(M(\vec{k},t)/M_0)$ versus k^2t signal attenuation curve, where the signal attenuation is less than 20%.

The RTO enhancement, $R(\vec{k},t)$, was calculated from the complete data set. The RTO probability was generated from Eq. [3.1.2] by numerical integration of the $M(\vec{k},t)/M_0$ versus k signal attenuation curve on a pixel-by-pixel basis using the IDL (Interactive Data Language, Boulder, CO) programming language. The result was then inserted into Eq. [3.1.25], using a bulk water diffusion coefficient of $3.0 \times 10^{-5} \text{ cm}^2/\text{s}$ at 37° C , to determine the RTO enhancement for the creation of the RTO enhancement maps.

T_2 maps were generated by fitting the images, acquired at different echo times (TE's), on a pixel-by-pixel basis with a least-squared algorithm to the T_2 -relaxation equation

$$M_{xy} = M_0 e^{-\frac{TE}{T_2}}, \quad [3.2.4.3]$$

where M_{xy} is the transverse magnetization at the echo time, TE , and M_0 is initial magnitude of magnetization following a 90° RF pulse applied to a system at the Boltzmann equilibrium. Histograms of the diffusion, RTO-enhancement and T_2 maps

were generated for all tumors and normalized by the total non-zero pixel count of the corresponding map.

Histological slices were digitized using a computer-based imaging system (Alpha Imager 2000, Alpha Innotech Inc., CA) and stored for further processing. Necrotic areas were measured by manual tracing using the OPTIMAS (BIOSCAN, Edmonds, WA) image processing software package. The necrotic areas detected on the histology stains were then compared to the ADC, R , and T_2 maps to identify necrotic and viable tissue area. Normalization of the necrotic area, as detected by manual tracing, by the entire tumor area of the histological slice yields the necrotic tumor fraction.

3.3 Results

NMR spectroscopy:

Figure 3.3.1 shows the natural logarithm of the measured signal intensity ($\ln(M/M_0)$) versus k^2 for water diffusing in a 1.4 cm³ RIF-1 tumor at five different diffusion times of 42 (◆), 92 (■), 192 (ρ), 292 (▲) and 492 (●) ms. The signal attenuation of the plot $\ln(M/M_0)$ versus k^2 is linear for small values of k^2 and approaches a constant for large values of k^2 . It can be seen that an increase in diffusion time increases the signal attenuation. The signal attenuation curve of the $\ln(M/M_0)$ versus k^2 plot for the shortest diffusion time of 42 ms levels off at a value of approximately -1.4 while the attenuation curve for the longest diffusion time of 492 ms levels off at approximately -3.0.

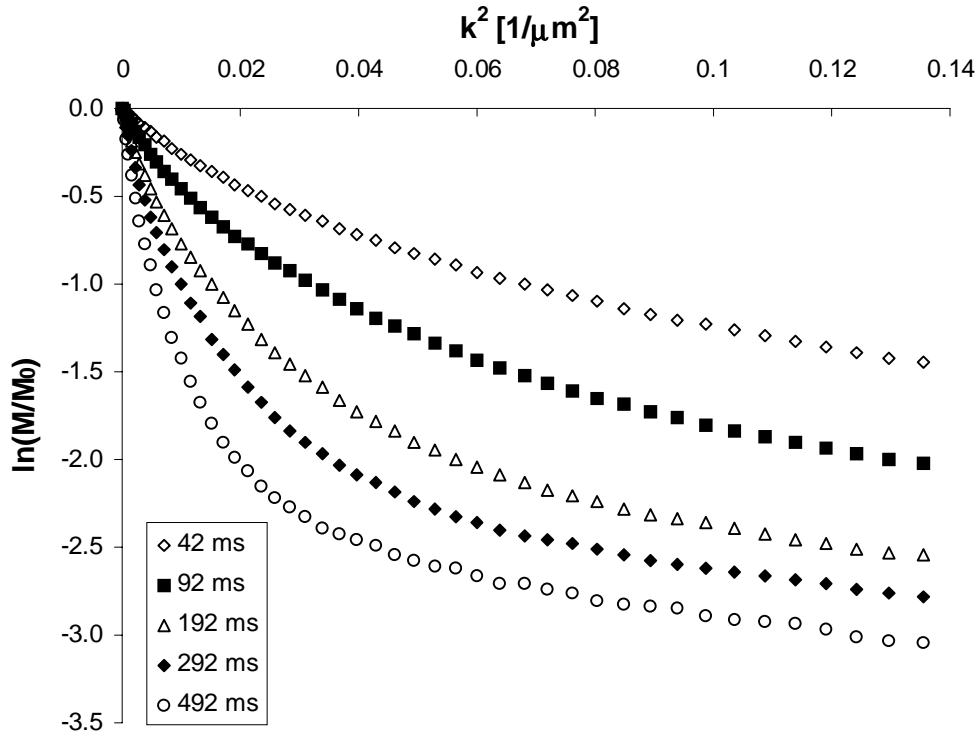


Figure 3.3.1: Plot of the natural logarithm of the measured signal intensity ($\ln(M/M_0)$) versus k^2 for water diffusing in a RIF-1 tumor of 1.4 cm^3 at five different diffusion times ranging from 42 (\diamond), 92 (\blacksquare), 192 (\triangle), 292 (\blacklozenge) to 492 (O) ms.

Figure 3.3.2 shows a plot of the absolute RTO probability, F , versus $1/k$ for the data shown in Fig. 3.3.1. The solid lines are calculated from the RIF-1 tumor data of Fig. 3.3.1 and the dashed lines are calculated for freely-diffusing water. The plot demonstrates that the existence of restrictions in RIF-1 tumors leads to higher RTO probability as compared to water molecules diffusing in a bulk solution. Larger diffusion gradients translate to a fine resolution.

Molecules diffusing freely for 42 ms have approximately a 3.8% chance to be found within a radius of $l_{min} = 3 \text{ }\mu\text{m}$ near their origin, while water molecules diffusing in a tumor have a 41% chance to be found within the distance of $l_{min} = 3 \text{ }\mu\text{m}$ of their starting

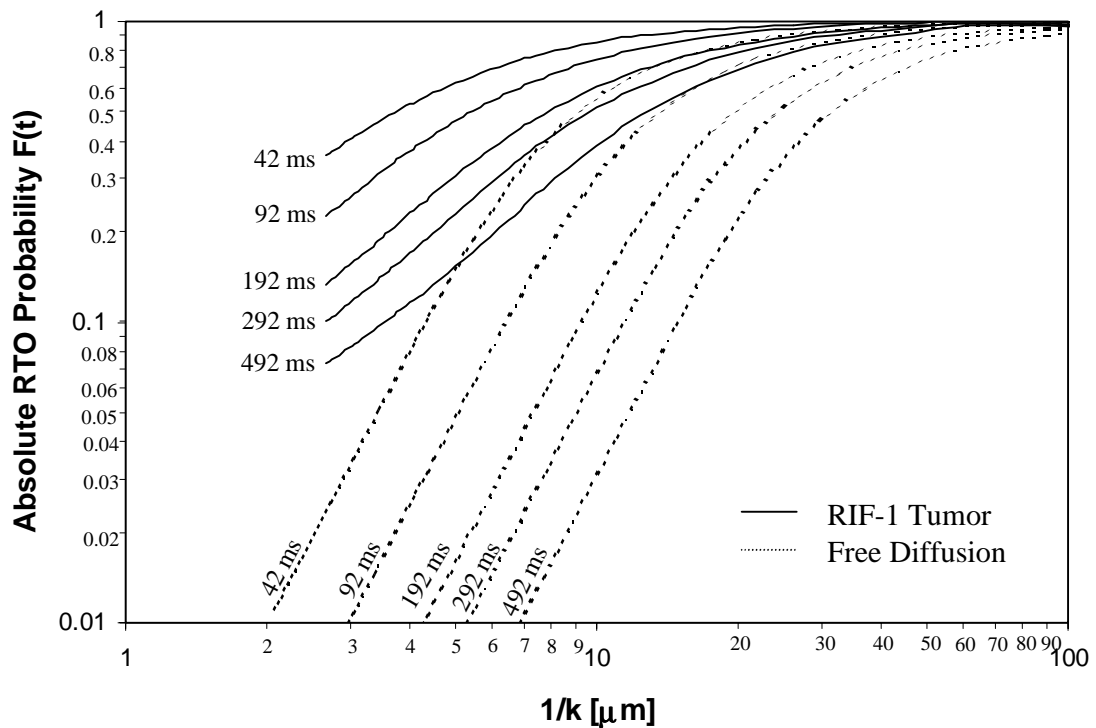


Figure 3.3.2: Plot of the absolute RTO probability, F , versus $1/k$ for a single RIF-1 tumor at five different diffusion times of 42, 92, 192, 292 and 492 ms and the corresponding, calculated curves for water. The solid lines are calculated from the RIF-1 tumor data of Fig. 3.3.1 and the dashed lines are calculated for freely diffusing water.

position. This difference in the absolute RTO probability becomes even larger at longer diffusion times, as molecules have more time to probe the surrounding space and make contact with the restricting boundaries.

Another way to view the effect of restrictions on diffusing water molecules is to plot of the RTO enhancement, R , versus $1/k$. Figure 3.3.3 shows a plot of the RTO enhancement, R , versus $1/k$ calculated from the RTO tumor data displayed in Fig. 3.3.1. The graph displays the enhancement between water molecules diffusing in RIF-1 tumors and bulk solution. Water molecules diffusing for 42 ms in RIF-1 tumors are 10.8 (41 versus 3.8) times more likely to be found within a sphere of radius 3 μm than water molecules

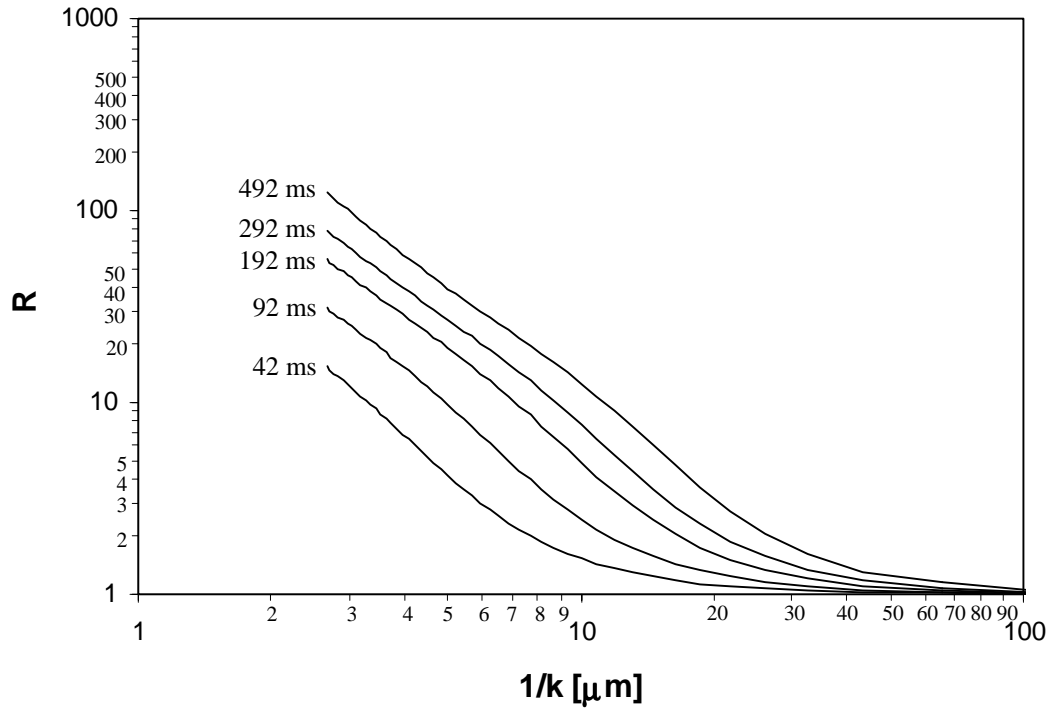


Figure 3.3.3: Plot of the RTO enhancement, R , calculated from the absolute RTO probability as displayed in Fig. 3.3.2, versus $1/k$ for water diffusing in a RIF-1 tumor at five different diffusion times ranging from 42, 92, 192, 292 to 492 ms.

diffusing in bulk solution, which is the same result as seen in Fig. 3.3.2 presented in a different way.

Figure 3.3.4 shows a plot of the RTO enhancement, R , for four different RIF-1 tumor volumes ranging from 0.7 (◆), 0.8 (■), 1.1 (▲) to 1.4 cm³ (●), plotted versus five different diffusion times (42, 92, 192, 292, and 492 ms) at $1/k = 2.7 \mu\text{m}$. The graph demonstrates that the differences in RTO enhancement, due to different amounts of restricting diffusion barriers, are largest at long diffusion times. The larger tumors, which are generally more necrotic, display smaller RTO enhancement than the smaller tumors. The smallest tumor (0.7 cm³) in Fig. 3.3.4, with the smallest necrotic tumor fraction, has the largest enhancement ($R = 208$), while the largest tumor has the smallest enhancement ($R = 130$) at a diffusion time of 492 ms.

are generally more necrotic, display smaller RTO enhancement than the smaller tumors. The smallest tumor (0.7 cm^3) in Fig. 3.3.4, with the smallest necrotic tumor fraction, has the largest enhancement ($R = 208$), while the largest tumor has the smallest enhancement ($R = 130$) at a diffusion time of 492 ms.

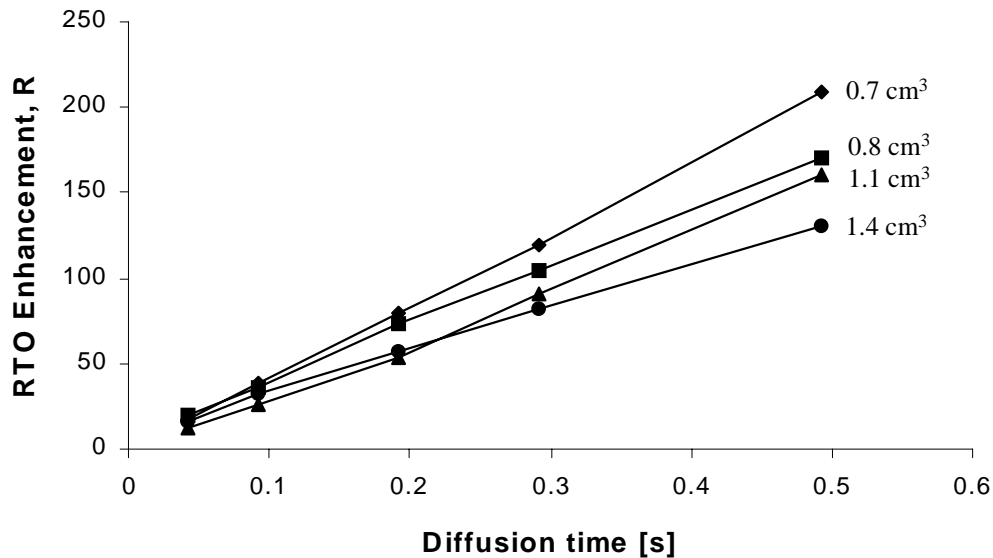


Figure 3.3.4: RTO enhancement, R , for four different RIF-1 tumor volumes, ranging from 0.7 (◆), 0.8 (■), 1.1 (▲) to 1.4 cm^3 (●), plotted versus five different diffusion times (42, 92, 192, 292, and 492 ms) and a sphere radius of $2.7 \mu\text{m}$. Large tumors are generally more necrotic resulting in a lower RTO enhancement. This graph demonstrates that the best separation in RTO enhancement between tumors of different necrotic fractions is achieved at long diffusion times.

Even though the results gained by NMR spectroscopy are promising, they are strongly influenced by volume averaging effects due to contributions from many different tissue types. NMR imaging, with its higher spatial resolution compared to spectroscopy, can reduce the amount of volume averaging and allow comparison with histology for further validation of the findings.

NMR Imaging

Figure 3.3.5 shows a plot of the natural logarithm of the measured signal intensity $\ln(M/M_0)$ of 32 images versus k^2 from two pixels of a RIF-1 tumor and the calculated curve for freely diffusing water at a temperature of 37° C. The curves show a difference in signal attenuation for a pixel in viable (◆) and necrotic (●) tumor tissue. Tissue types were identified by examination of the corresponding histological slice. Both tumor tissue curves show evidence of restricted diffusion as compared to the freely diffusing water (▲). The viable tissue displays a smaller ADC (less steep initial slope) than the necrotic tissue. The difference in ADC values is the difference in the initial slope of the two curves. ADC values extracted from the tumor data in Fig. 3.3.5 give 77 and 133×10^{-7}

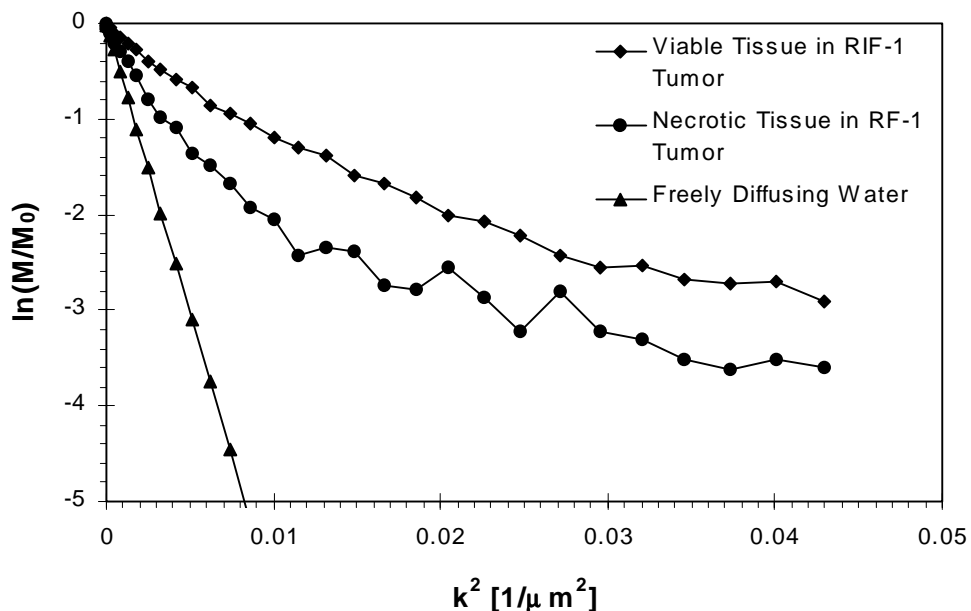


Figure 3.3.5: Plot of the natural logarithm of the signal intensity $\ln(M/M_0)$ versus $k^2 = (\gamma G \delta)^2$ for a pixel in viable (◆) and necrotic (●) RIF-1 tumor tissue as well as the calculated curve for freely diffusing water (▲) at 37°C. Data were acquired using a diffusion-weighted stimulated-echo pulse sequence with a diffusion-gradient pulse duration of 7.0 ms, a diffusion time of 201.5 ms and 32 diffusion-gradient increments from 18.6 G/cm in 0.6 G/cm steps.

cm^2/sec , for viable and necrotic tissue, respectively. The plot further shows that viable and necrotic tissue possesses a different RTO probability, which is proportional to the area between the curve and the k^2 axis. Data points with the larger k values are given the largest weighting in the calculation of the RTO enhancement. The RTO enhancement was calculated to be 16.4 and 7.1 for viable and necrotic tissue, respectively.

Figure 3.3.6 shows the generated T_2 , ADC and R maps of three representative RIF-1 tumors in comparison to the corresponding H&E stained histology slice obtained from the same spatial location as the NMR imaging slice. Maps and histological section have a slice thickness of 3.0 mm and 5 μm , respectively. The volumes of the three RIF-1 tumors displayed in A, B and C are 0.7, 1.3 and 2.1 cm^3 , respectively. The viable tissue in the histological section is depicted by the dark color and the necrotic tissue by the brighter gray tones, with the largest tumors showing the largest necrotic area. Visual comparison of the histological sections and the ADC and RTO enhancement maps in Fig. 3.3.6 show that there is only general spatial agreement between the MRI parameters and the necrotic regions. ADC and RTO enhancement maps, with their coarser resolution compared as to the histology, display only the more prominent features found in the histological section. T_2 maps displayed on the left side of Fig. 3.3.6 show only small changes for the varying degrees of necrosis and no spatial correlation with either the ADC and RTO enhancement maps or the histological section.

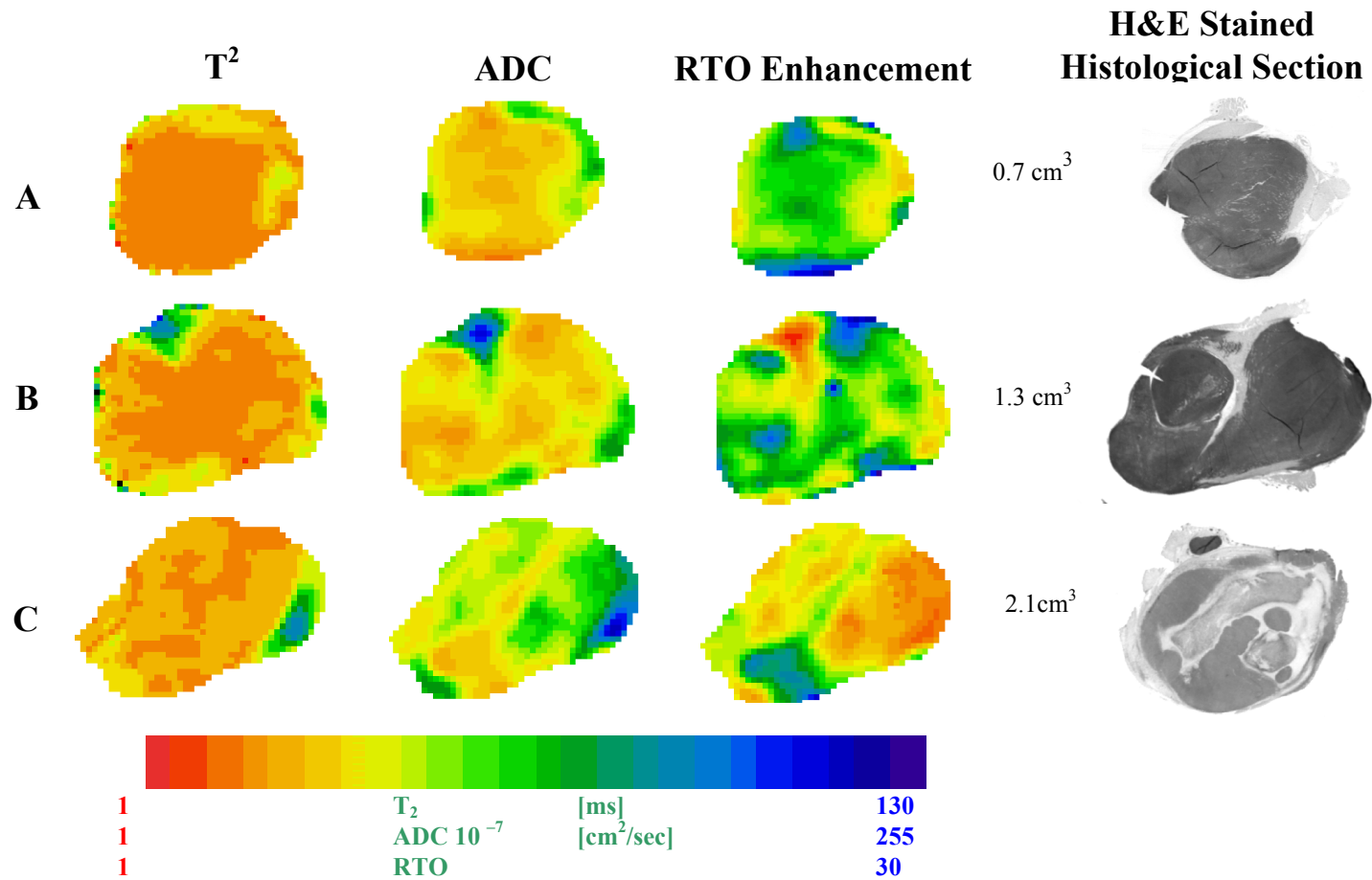


Figure 3.3.6: T_2 , ADC and RTO enhancement maps of three representative RIF-1 tumors with a slice thickness of 3.0 mm in comparison to the corresponding hematoxylin and eosin (H&E) histology slice of 5 μ m thickness obtained at the same spatial location. ADC and RTO maps were created from diffusion-weighted NMR images acquired with a diffusion time of 201.5 ms, an echo time of 56 ms, and 32 increments of the diffusion-gradient from 0.0 to 18.6 G/cm in 0.6 G/cm steps. T_2 maps are generated from nine images with varying echo times.

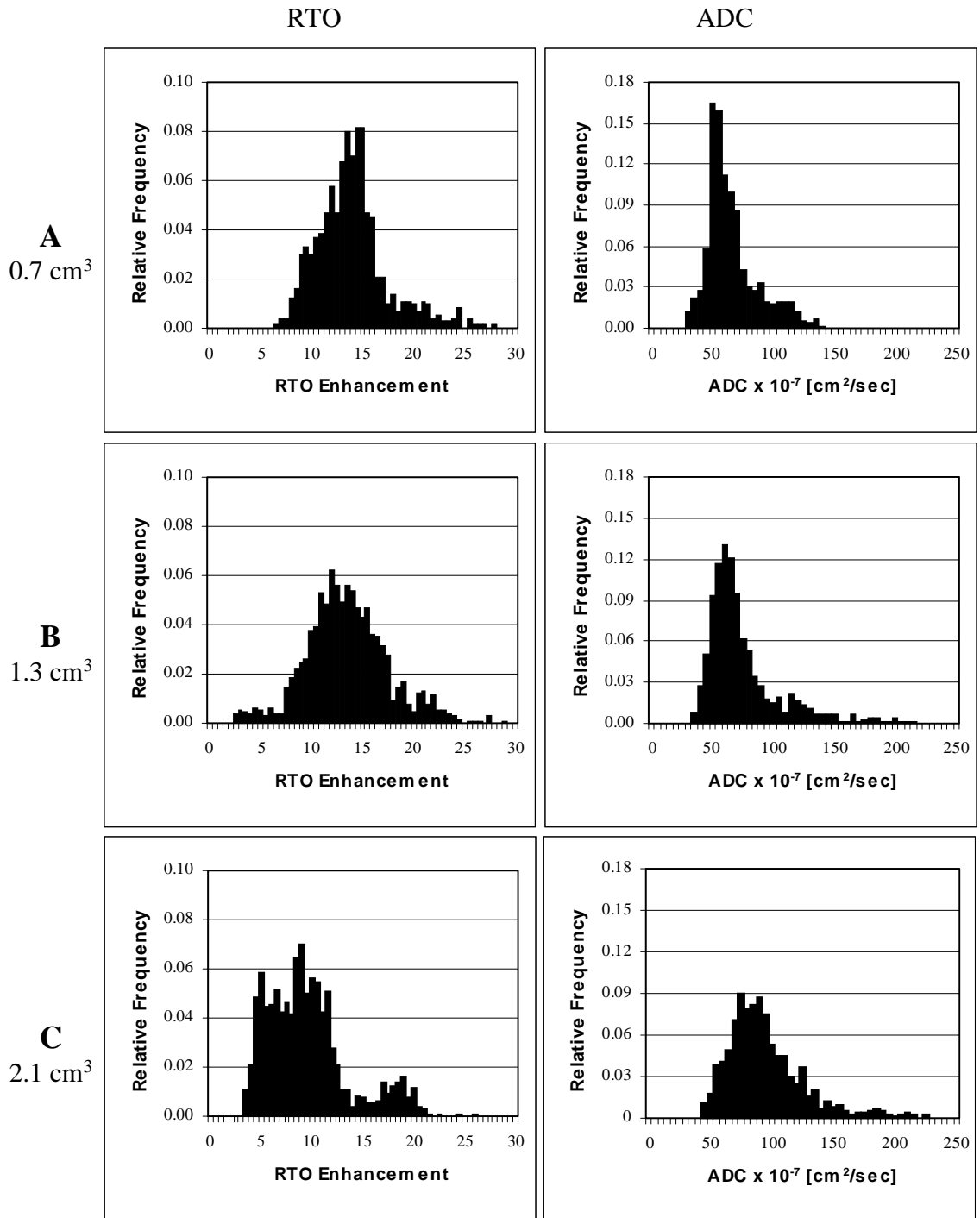


Figure 3.3.7: Histograms generated from the ADC and RTO enhancement maps in Fig. 3.3.6 and normalized by the total non-zero pixel count of the respective maps. The tumor volumes for the three tumors A, B, and C are 0.7, 1.3 and 2.1 cm³, respectively.

Figure 3.3.7 shows the histograms generated from the ADC and RTO enhancement maps in Fig. 3.3.6 normalized by the total non-zero pixel count of the respective maps. The ADC histogram (Fig. 3.3.7, A) shows a sharp peak for the smallest tumor with almost no necrosis. As the tumor volume increases, so does the amount of necrosis present in the tumors (Fig. 3.3.6). The mean ADC for the three representative tumors of volume 0.7, 1.3, and 1.4 cm³ is 68, 77, and 97 x 10⁻⁷ cm²/sec, respectively, with the tumor displaying the largest amount of necrosis having the highest mean ADC. The increase in mean ADC is accompanied by an increase in the width of the distribution, which is caused by a shift of pixels towards higher ADC values and a decrease in the distribution magnitude. The RTO enhancement histograms (Fig. 3.3.7, right side) show a behavior similar to that of the ADC. For the smaller two tumors with little necrosis, a relatively narrow distribution

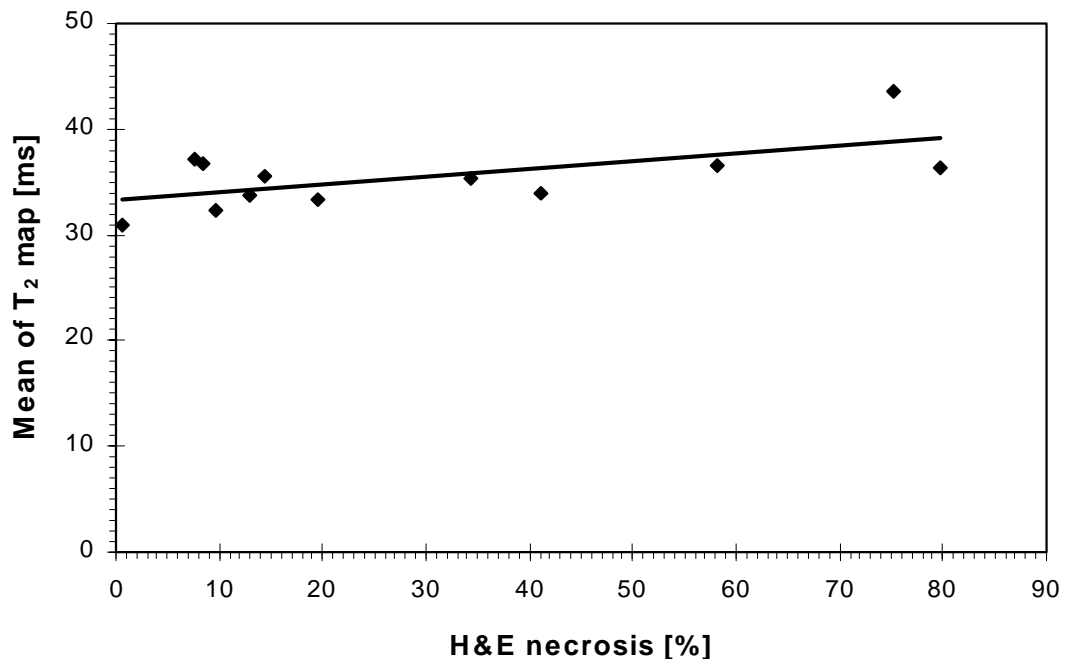


Figure 3.3.8: Plot of the T₂ map mean versus the necrotic tumor fraction as determined by hematoxylin and eosin (H&E) staining, for 12 RIF-1 tumors of varying sizes and degrees of necrosis.

can be observed. The mean RTO enhancement for the three representative tumors of volume 0.7, 1.3, and 1.4 cm³ is 14, 13.7, and 9.8, respectively, with the tumor displaying the largest amount of necrosis having the smallest RTO enhancement. The decrease in the RTO enhancement with increasing necrosis is accompanied by a dispersion of the histogram and a shift of pixels towards lower RTO enhancement, while the magnitude of the distribution decreases.

Figure 3.3.8 is a plot of the mean T₂, calculated from the NMR T₂ maps, versus the necrotic tumor fraction (as determined by H&E staining) for 12 RIF-1 tumors of varying sizes and degrees of necrosis. The mean T₂ correlates poorly (r = 0.62) with the necrotic

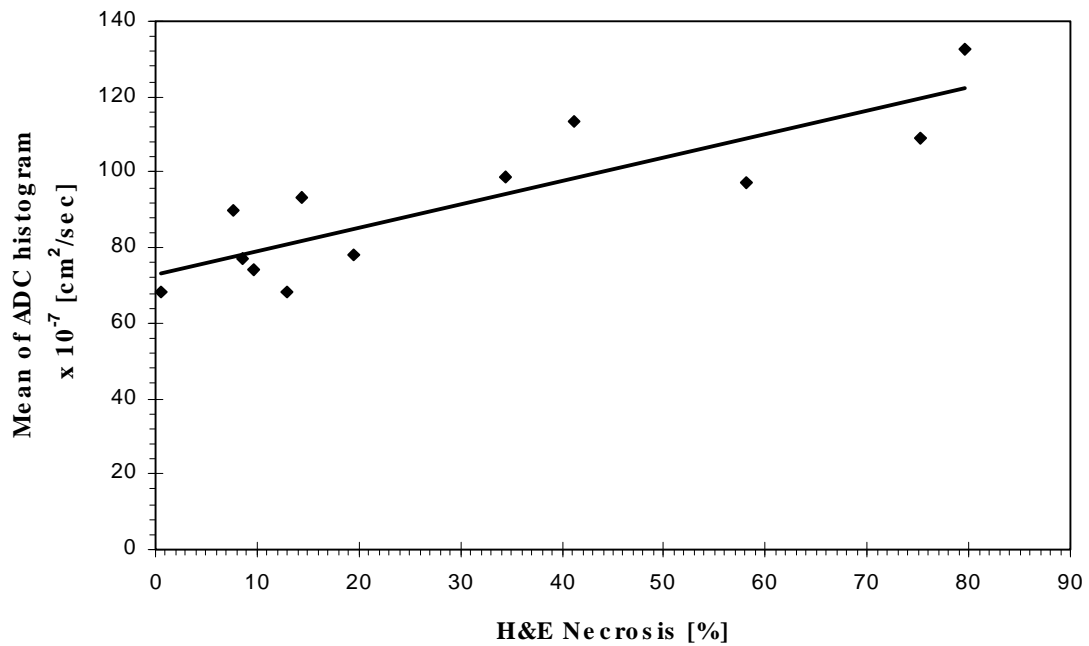


Figure 3.3.9: Plot of the ADC map mean versus the necrotic tumor fraction, as determined by hematoxylin and eosin (H&E) staining, for 12 RIF-1 tumors of varying sizes and degrees of necrosis.

tumor fraction and exhibits only small change over the entire range of necrotic tumor fractions.

Figure 3.3.9 is a plot of the mean ADC, calculated from the ADC histograms, versus the necrotic tumor fraction, as determined by H&E staining, for 12 RIF-1 tumors of varying sizes and degrees of necrosis. The plot illustrates how well the mean ADC tracks necrosis in RIF-1 tumors over a wide range of necrotic tumor fractions. The correlation coefficient for this data is $r = 0.86$.

The graph in Fig. 3.3.10 plots the mean of the RTO enhancement histograms versus the necrotic tumor fraction, as determined by H&E staining, for 12 RIF-1 tumors of varying sizes and necrotic volumes. The correlation coefficient for this data is $r = 0.82$.

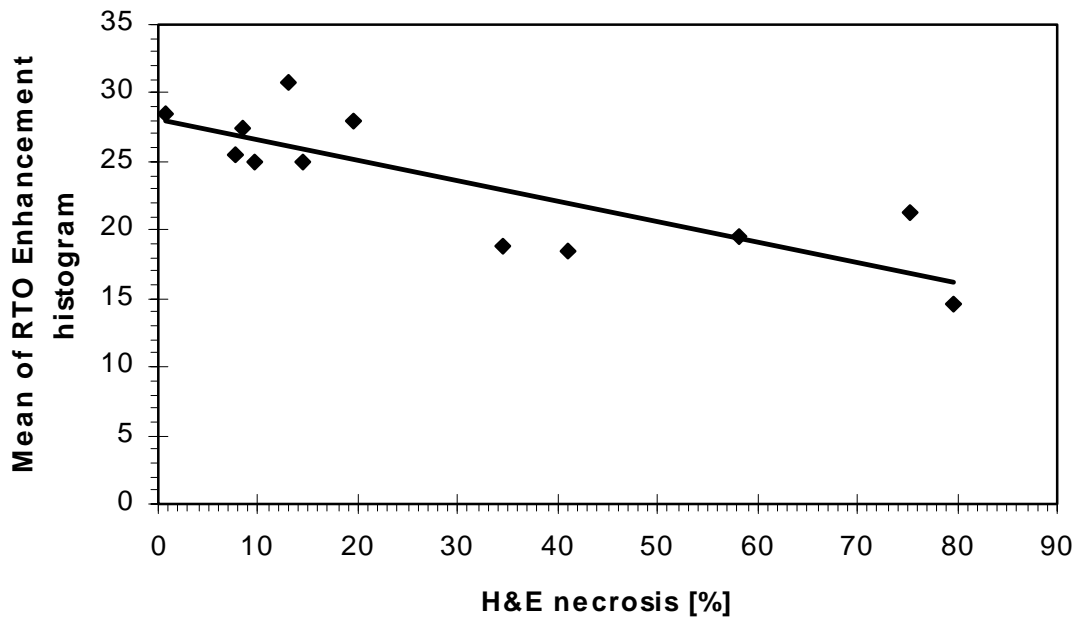


Figure 3.3.10: Plot of the RTO enhancement map mean versus the necrotic tumor fraction, as determined by hematoxylin and eosin (H&E) staining, for 12 RIF-1 tumors of varying sizes and degrees of necrosis.

3.4 Discussion and Conclusion

Fig. 3.3.1 clearly shows the differences of the water signal attenuation from RIF-1 tumors for a varying range of diffusion times. The differences in the initial slope of the attenuation curves at small values of k^2 show the time-dependence of the diffusion coefficient, $D(t)$. With increasing diffusion times, t , the diffusing molecules sample larger spaces and therefore have an increased chance to find obstacles in their diffusion path, reducing their mean squared displacement. This behavior is well reflected by the initial slopes of Fig. 3.3.1, where shallowest slope is observed for the shortest diffusion time and the steepest for long diffusion times. In this regime of small k^2 values, the measurement includes most of the spin population. In the plateau region (large k^2 regime), the signal arises predominately from a spin population with low diffusion coefficients. These spins have not been completely dephased by the large applied diffusion gradient.

Since diffusing molecules at long diffusion times encounter more restrictions than at short diffusion times, their absolute RTO probability, $F(t)$, is increased. This increase in $F(t)$ for longer diffusion times is illustrated in Fig. 3.3.2, where $F(t)$ is plotted versus $1/k$ for five different diffusion times. The plot demonstrates that for a large radius ($\sim 1/k$) of the sphere of origin the absolute RTO probability approaches unity, since the diffusing molecules cannot diffuse far enough to leave the sphere around their point of origin. For very small values of $1/k$ (small radius), the absolute RTO probability decreases since it is less likely that the molecules will return to their sphere of origin or have never left it. Comparing of the absolute RTO probability of water molecules diffusing in a RIF-1

tumor with that of water diffusing in an unrestricted bulk solution, demonstrates a significantly increased $F(t)$ in the restricted tissue environment. Further inspection of Fig. 3.3.2 reveals that for water molecules diffusing for 492 ms in RIF-1 tumor tissue, there is approximately a 25% chance that the molecules will be found within a sphere of 7- μm radius. By comparison, water molecules diffusing in bulk solution have only a 1% chance of being found within a sphere of equal dimensions. For shorter diffusion times, like 42 ms, the absolute RTO probability for diffusing molecules to return to a sphere with radius 7 μm is 75% in RIF-1 tumors and 32% in the bulk phase. This can be interpreted that at 492 ms, water molecules in a RIF-1 tumor are about 25 times more likely to be found within a sphere of the above dimensions than bulk water molecules, but only twice as likely for a diffusion time of 42 ms. The plot in Fig. 3.3.2 also shows that the largest enhancements are achieved at long diffusion times.

This enhancement over freely diffusing water for different diffusion times and sphere radii is described by the RTO enhancement in Fig. 3.3.3. The RTO enhancement is a different way to present the enhancement of restricted diffusion over that of free diffusion as seen in Fig. 3.3.2. The extracted enhancement from Fig. 3.3.2 maps to the plot of the RTO enhancement, R . At a sphere radius of 7 μm , the absolute RTO probability for 42 ms was 0.75 and 0.32 for diffusion in RIF-1 tumor and bulk water, respectively. This results in an enhancement of 2.3, which is in perfect agreement with the plot in Fig. 3.3.3. The plot also shows that R increases with diffusion time. For the example with the sphere radius of 7 μm and a diffusion time of 492 ms the calculated RTO enhancement ($R = 25$) and the extracted enhancement ($R = 0.25/0.01$) of the RIF-1 tumor ($F = 0.25$) over freely

diffusing water ($F = 0.01$) from Fig. 3.3.2 are in agreement. A further increase in the RTO enhancement can be achieved by decreasing the radius of the sphere ($\sim 1/k$). For the example at a diffusion time of 42 ms, the reduction to 3 μm yields an R of 10.8. This can be verified by inspection of Fig. 3.3.2, where the F at these parameters is 0.41 for the RIF-1 tumor and 0.038 for the freely diffusing water, respectively. From the examples above, it can be seen that the largest enhancement is achieved at long diffusion times and a small sphere radius (l_{min}).

A plot of the maximum RTO enhancement ($1/k_{max}$) of water as a function of diffusion time in RIF-1 tumors (Fig. 3.3.4) illustrates the increase in RTO enhancement with increasing diffusion time. The plot clearly reveals that the RTO enhancement decreases with tumor size and that the smaller tumors have a larger enhancement than the larger tumors. This is presumably due to the presence of more viable (i.e., less necrotic) tumor tissue. Smaller solid tumors presumably have less necrotic tissue and the spectroscopically-measured diffusion coefficient is expected to be higher since viable tissue presents more restrictions to diffusing molecules than necrotic tissue. Necrotic tissue debris is removed by auto- and/or heterolysis, leaving behind spaces with fewer membranes and organelles. Therefore, water molecules can diffuse longer distances without encountering any obstacles. As tumors grow larger, the amount of necrosis generally increases and the contribution of signals from water molecules with larger diffusion coefficients gives rise to an overall increase in the tumor water diffusion coefficient. This is consistent with the results found by Helmer et al. (1995), where

higher diffusion coefficients in RIF-1 tumors generally correlated with increased tumor necrosis.

Since spectroscopic data has contribution from a many different tissue types, the resulting measurement is strongly influenced by volume-averaging effects. NMR imaging can reduce this problem, since smaller imaging volumes are thought to contain fewer tissue types. The increased spatial resolution achieved by NMR imaging allows a comparison of the NMR data with tumor histology and should make it a more sensitive metric.

Plots of the signal attenuation, $\ln(M/M_0)$, versus k^2 for pixels originating in clearly viable and necrotic tumor tissue (Fig. 3.3.5), as verified by comparison to the histology, show that the ADC and RTO enhancement are sensitive to the structural differences between viable and necrotic tissue. The presence of restrictions causes a deviation from the linear diffusion behavior of water and thus both the ADC and the RTO probability can be used to distinguish between the two types of tumor tissue. The apparent diffusion coefficient, extracted from the initial slope of the signal attenuation, and the RTO enhancement, calculated from the complete data set, allow separation between viable and necrotic tissue due to the differences in pathophysiological structure.

Figure 3.3.5 shows a 73% difference in the initial slope of the attenuation curves for a pixel in necrotic (solid circle) and a pixel in viable tissue (solid diamond). The steeper initial slope of the attenuation curve from the necrotic tissue results in a higher apparent diffusion coefficient, ADC ($133 \times 10^{-7} \text{ cm}^2/\text{sec}$), than the shallower slope of the

attenuation curve from the viable tissue ($77 \times 10^{-7} \text{ cm}^2/\text{sec}$). Viable tissue confines diffusing water molecules to a smaller area (i.e. reduces their average net displacement) and consequently reduces their apparent diffusion coefficient. In necrotic tissue, the diffusing water molecules have a larger free diffusion path, yielding a larger average net displacement and hence a higher apparent diffusion coefficient. This is consistent with our hypothesis that necrotic tissue has fewer restricted water molecules.

The differences in the attenuation curves for viable and necrotic tissue in Fig. 3.3.5 also illustrate the differences in the RTO probability, which is proportional to the area between the attenuation curve and the k^2 axis with data from large k values given the largest weighting. The attenuation curve of necrotic tumor tissue encloses a larger area as compared to the attenuation curve of viable tissue. The RTO enhancement for the viable and necrotic tissue was calculated to be 16.4 and 7.1, respectively, resulting in a 131% difference between the two tissue types. In comparison to the ADC (73%), the RTO has twice the dynamic range for the same two pixels.

The calculated ADC and RTO enhancement maps in Fig. 3.3.6 show only general spatial agreement with the histology. Larger areas in the histology slice, which are clearly classifiable as either necrotic (bright gray tones) or viable (dark gray tones) tumor tissue are well represented by the ADC and RTO enhancement maps. Both ADC and RTO enhancement maps display the same general features. The T_2 maps, which are a function of the tissue water content, show little agreement with either the histology or the ADC and RTO enhancement maps. Given the difference in ADC and RTO enhancement for

viable and necrotic tissue, an attempt was made to determine thresholds for the two quantities that identify necrotic and viable tissue on both maps. The detected necrotic area for varying thresholds was correlated with the necrotic tumor fraction of the histological slide. The best correlations between the necrotic area on the histology slices and the necrotic area (n=12) detected by thresholding of the ADC and RTO enhancement maps was 0.69 and 0.72, respectively, for an ADC threshold of $84 \times 10^{-7} \text{ cm}^2/\text{sec}$ and RTO enhancement threshold of 6. Despite the reasonably good correlation coefficients, the necrotic areas detected by the thresholds had relatively poor visual correspondence with the necrotic areas in the histological section.

Since major features in the MRI maps showed a general agreement with the histology, histograms (Fig. 3.3.7) of the maps were created. The increase in necrotic fraction with increasing tumor size (0.7, 1.3 and 2.1 cm^3) is reflected by a shift in the histogram mean ADC and RTO enhancement. Mean ADC values shift with increasing tumor volume from 68 to 77 to $97 \times 10^{-7} \text{ cm}^2/\text{sec}$, respectively. This behavior is expected, since an increase in necrotic fraction would be reflected as an increase in the mean ADC value of the histogram. The use of the mean rather than the median was desirable in this case to be sensitive to extreme values. Similar behavior was observed for the RTO enhancement histograms, where the mean values shifted from 14.2 to 13.2 to 9.8, respectively, due to the decreased RTO probability in necrotic tissue.

The change in histogram means from the smallest tumor volume to the largest is 42% for the ADC and 44% for the RTO enhancement. These numbers show that when parameter

values from different tissue types are averaged, the large difference between the RTO enhancement and the ADC are eliminated. The means of the histograms resemble more the spectroscopic approach, where different tissue types are averaged together and it can be implied that, due to this volume averaging, spectroscopic studies will not gain the advantage of the greater sensitivity achieved by the RTO enhancement.

The mean T_2 values, with their small dynamic range, exhibit only small changes over the entire range of necrotic tumor fractions and poor correlation ($r = 0.62$). This result is not unexpected considering that T_2 maps showed neither visual agreement with histology or any significant changes in T_2 values between T_2 maps of varying necrotic area. T_2 measurements are a function of the tumor tissue water content and thus not sensitive to the structural differences between viable and necrotic tumor tissue.

In comparison, the mean ADC values show a high correlation ($r = 0.86$) with the necrotic tumor fraction and a good tracking of the increasing necrosis by the mean ADC (Fig. 3.3.9). The ADC pixel distribution in tumors with relatively little necrosis consists of pixels that reside primarily in viable tissue. These pixels have low ADC values and hence their distribution is centered around a relatively small mean ADC. Increased necrosis within the tumor slice causes an increased contribution from pixels with high ADC values, associated with necrotic tissue, and thereby a shift of the mean ADC towards higher values. As the contribution of pixels from necrotic tumor tissue increases, so does the mean ADC.

Similar behavior, but in the opposite direction, can be seen in the plot of the mean RTO enhancement versus the necrotic tumor fraction (Fig. 3.3.10). The net displacement of molecules diffusing in viable tissue results in a low RTO enhancement. In tumors with small necrotic tumor fractions, most of the pixels have high RTO enhancement and hence the RTO enhancement pixel distribution is centered around a low mean RTO enhancement value. Increasing amounts of necrosis permit a larger net displacement of diffusing water molecules and the contribution of pixel with low RTO enhancement, associated with necrotic tumor tissue, increases. The increase in the number of pixels displaying a low RTO enhancement causes the mean RTO enhancement to shift towards a lower value. The decrease of the mean RTO enhancement with increasing necrotic tumor fraction can be observed in Fig. 3.3.10 and illustrates that the RTO enhancement can be used to differentiate different amounts of necrosis. Correlation of the mean RTO enhancement with the necrotic tumor fraction results in a correlation coefficient of $r = 0.82$.

The poor visual agreement of the ADC and RTO enhancement maps with the histology can be attributed to the volume-averaging effects due to the 3-mm slice thickness used during imaging. The sharper outline of the stained tumor slice is due to the higher spatial resolution of the histology compared to the in-plane resolution of 0.47 mm per pixel for the calculated ADC and RTO enhancement maps. The volume-averaging is enhanced by the MRI slice thickness of 3 mm compared to the slice thickness of $\sim 5 \mu\text{m}$ for histology. This large difference in slice thickness leads to a reduction in the details and averaging of different tissue types within a single pixel of the MRI maps.

The averaging of different tissues in each pixel is further enhanced by the regions of necrotic and viable tissue. This can be seen in the histological section in Fig. 3.3.6, A. As necrosis progresses, more and more cells per unit area become necrotic, causing the stain to appear brighter and making it more difficult to clearly separate necrotic from viable tissue. Separation of the tissue in three categories - viable, mixed and necrotic - may seem more appropriate, but is even more difficult to achieve due to the varying amount of mixed tissue and this issue will need to be addressed in future studies.

Another problem for comparisons between imaging and histology arises from the distortion inherent to the echo-planar imaging process. During the sweeping of k space, the EPI gradient switching alters the phase of the acquired signal which leads to distortions in the image during the Fourier transform. Although these distortions are small in our case, the mismatch in geometry hampers a comparison with histology. To enhance the problem, the histology has its own geometrical distortions due to dehydration of the tumor section during staining. Fixation and staining are dehydrating processes and impart a significant amount of shrinkage on the histology slice, making a direct one-to-one comparison impossible. While the imparted shrinkage still allows a comparison of the general features, the necrotic area cannot be determined accurately, since the amount of reduction in geometry is unknown. The assessment of the necrotic area with respect to the slice area allows determining tumor necrosis on a relative basis.

Despite these differences, it has been demonstrated that both the ADC and RTO enhancement can be used as indicators of necrosis in tumor tissue and are more sensitive

than conventional T_2 -weighted MRI. The RTO enhancement is, however, more sensitive than the ADC, implying that the number of restricted spins (the signal at the largest diffusion gradient) is a better measure of the tissue viability than is a parameter that reflects both unrestricted and restricted water molecules. The advantage of the ADC data set, which is a subset of the RTO data set, is a shorter acquisition time and smaller values of the space vector for data collection. For the collection of the RTO data set, large k values are necessary, which require large diffusion gradient magnitudes that are not commonly available on most clinical MRI scanner.

Both the ADC and RTO enhancement provide a large improvement for detecting necrosis as compared to T_2 -weighted MRI, which is not sensitive to the structural differences of the two tissue types under investigation. The ability of the ADC and RTO enhancement to differentiate between viable and necrotic tissue could be especially useful in defining dynamic changes in tumors in response to therapeutic intervention at early time points, where a non-invasive method is needed to verify the efficacy of chemo- or radiation therapy.

Chapter 4

**Return-to-the-Origin Probability and ADC Mapping
of Water as Early Indicators of the Efficacy of
Chemotherapy in RIF-1 Tumors**

4.0 Return-to-the-Origin Probability and ADC Mapping of Water as Early Indicators of the Efficacy of Chemotherapy in RIF-1 Tumors

The purpose of this study is to compare the ability of the return-to-the-origin (RTO) probability and the apparent diffusion coefficient (ADC) to detect and characterize changes in water diffusion in response to chemotherapeutic treatment of RIF-1 tumors using 5-Fluorouracil (5-FU). Information pertaining to tissue structure can be gathered by measuring the displacement of endogenous water molecules. The degree to which diffusing water molecules are restricted is reflected by both the return-to-the-origin (RTO) probability and the apparent diffusion coefficient (ADC). Molecules in viable tissue have a low ADC and high RTO probability due to the presence of restricting boundaries, like cell membranes and organelles, that confine the molecules. Water molecules in necrotic tissue experience fewer restrictions and hence have a higher ADC, while their RTO probability is decreased. Chemo- and radiotherapy induced pathophysiological and structural changes associated with tissue necrosis can be detected by ADC and RTO probability. Mice bearing RIF-1 tumors treated with 50 and 100 mg/kg 5-Fluorouracil (5-FU) were monitored on a daily basis until the tumor volume exceeded 2.0 cm³. Diffusion-weighted, stimulated-echo echo-planar images were taken daily and ADC maps and RTO enhancement maps were constructed from the images. This study shows that changes in the dynamic state of tumor physiology after therapeutic intervention can be visualized by both the ADC and RTO enhancement. The largest changes in mean ADC (87%) and mean RTO enhancement (106%) were observed at the

time point of maximum tumor regression, four days after the administration of the chemotherapeutic agent. This characterization of tumor response to chemotherapy permits the evaluation of optimal biological responses to therapy management and could potentially optimize the timing of therapy scheduling and thus improve patient care.

4.1 Introduction

Therapy schedules for most chemotherapy treatments are based on the limited understanding of pharmacokinetics and dosage is dependent upon the normal tissue response of the patient. A better understanding and monitoring of the dynamic state of tumor physiology in response to treatment would allow an improvement in the design of therapy scheduling strategies to optimize vulnerable periods of tumor biology for an increase in the efficiency of current treatment strategies. The purpose of this study is to compare the ability of the return-to-the-origin probability (RTO) and the apparent diffusion coefficient (ADC) to detect and characterize dynamic changes in water diffusion in response to chemotherapeutic treatment by 5-Fluorouracil (5-FU) of RIF-1 tumors. Recent studies of tumors have shown that the ADC is sensitive to pathological and structural changes in tumors associated with ischemia and necrosis (Helmer et al., 1995; Zhao et al., 1995a).

These structural changes can be assessed by the ADC and the application of the RTO probability as described in Chapter 3. The RTO probability (Mitra et al., 1995b) measures the probability that diffusing water molecules will be found near their initial position

after diffusing for a time, t . In the presence of diffusion-restricting barriers, the RTO probability will increase with respect to that of freely-diffusing water. This enhancement, R , over free diffusion is a useful metric to assess structural changes as they relate to necrosis and to differentiate between viable and necrotic tumor tissue (Helmer et al., 1997; Meiler et al., 1998).

Rapid cell proliferation causes a neoplasm to outgrow its vasculature. Cells in the affected areas lack an adequate supply of oxygen and become hypoxic. If the oxygen supply to these regions is not restored, the hypoxic cells become necrotic and the process of cellular degradation begins. This process causes structural changes as viable cells become hypoxic and subsequently turn necrotic. Hypoxia and necrosis cause cell swelling, rupture of membranes and subsequent auto- and/or heterolysis (Wyllie, 1981) to remove the resulting debris. Similar changes in structure can be induced by chemo- and radiation therapy (Aiken et al., 1994; Zhao et al., 1996). Magnetic resonance spectroscopy (MRS) *in vivo* can monitor metabolic changes in response to rapid tumor growth or therapeutic intervention. While MRS can detect changes in tumor metabolism (Steen, 1989; Kamm et al., 1996), it suffers from a relatively coarse spatial resolution due to the low abundance of these nuclei. In order to evaluate and verify the progression and efficacy of therapy, it would be advantageous to visualize changes in tissue viability at the spatial resolution achievable by water-proton MRI. As reported in Chapter 3, return-to-the-origin probability and ADC imaging can overcome these shortcomings in spatial resolution and allows visualization of necrosis in tumor tissue in response to therapeutic intervention.

4.2 Experimental Methods

4.2.1 Animal Preparation

All experiments and procedures were approved by the Animal Research Committee (ARC) of the University of Massachusetts Medical School. Animals were housed under diurnal lighting conditions and allowed free access to food and water before and after the imaging experiments. Eight-week-old, female C3H mice (Taconic Farms, Germantown, NJ) were anesthetized by intraperitoneal injection of 60 mg/kg sodium pentobarbital (Abbott Laboratories, Chicago, IL). The right hind leg was shaved and remaining hair removed with a commercial hair remover (NAIR, Carter Wallace Inc., New York, NY). Radiation induced fibrosarcoma, RIF-1 (Twentyman et al., 1980), cells from a second passage were suspended in Waymouth's medium supplemented with 15% ^{v/v} FBS and 10% ^{v/v} glycerol and stored in liquid nitrogen. Prior to inoculation, the frozen cells were defrosted and 0.15 ml of the suspension containing 1×10^5 cells was subcutaneously injected into the right hind leg with a 30-gauge hypodermic needle.

4.2.2 Chemotherapy

5-Fluorouracil (5-FU) powder (Sigma Chemicals, St. Louis, MO) was dissolved in sterile 0.9 % saline (Baxter, Deerfield, IL) and agitated with a vortex mixer. Animals were separated into three groups of 10 animals each; control group, drug group I and drug group II. As soon as the tumor volume reached 0.7 cm^3 , the animals received an

intraperitoneal injection of either drug or placebo. The control group received a placebo of saline, while the drug group I and II were injected with 50 and 100 mg/kg 5-FU, respectively. Both doses are well below the LD₅₀ dose of 260 mg/kg (Sijens et al., 1991). Tumor growth was assessed daily for all animals. The endpoint of the study was reached when the tumor volume exceeded 2.0 cm³. Tumor volume was determined by measuring the three major orthogonal axes with sliding calipers and the volume was calculated to be: $V = \pi/6 \times \text{length} \times \text{width} \times \text{height}$ (Shackney et al., 1978; Spang-Thomson et al., 1980; Euhus et al., 1986; Fiennes, 1988; Tomayko and Reynolds, 1989).

4.2.3 Dose Response Studies

Dose-response studies were performed prior to the MRI experiments in order to determine the tumor doubling time and the point of maximum tumor regression. The tumor volume was measured daily. None of the animals showed a significant reduction in body weight or activity. Tumor growth data were collected for all animals to determine tumor doubling time (*TDT*) and time-to-maximum regression (*TMR*).

4.2.4 NMR Measurements

Diffusion-weighted, stimulated-echo echo-planar images were acquired using a horizontal bore GE CSI-II 2.0 T / 45 cm imaging spectrometer operated at 85.56 MHz for protons and equipped with ± 20 G/cm self-shielded gradients. Experiments were

performed using a 4-turn solenoidal RF coil with 18-mm inner diameter placed around the tumor. Anesthesia was induced with 2% Isoflurane delivered in air at 1.5 l/min and maintained at 1.5% Isoflurane at the same flow rate. During the MRI experiments, the body temperature was maintained at 37°C by circulating 34°C warm air through the animal holder. The temperature was controlled using a T-type temperature probe (Omega, Stanford, CT) and a two-point feedback system.

The coronal plane for image acquisition was located at a constant offset of 3.0 mm with respect to the isocenter of the instrument to avoid image acquisition in the area of the underlying muscle tissue. The animals were immobilized on a stereotaxic holder, which ensured reproducible positioning in the bore of the instrument with respect to the isocenter, the underlying muscle, and the RF coil. The imaging plane was kept at a fixed location to monitor changes at this location. This approach was chosen since the positioning has better reproducibility than positioning with respect to the changing tumor core. During the time course of the study, the tumor was allowed to grow through the imaging plane.

Coronal images were acquired through the tumor with FOV = 30.0 mm, 64×64 data matrix, slice thickness of 3.0 mm, TR = 6 s, NEX = 8, TE = 56.0 ms, and SW = ± 70 KHz. Diffusion-gradients were incremented in 32, 0.6 G/cm steps from 0.0 to 18.6 G/cm. The diffusion time was 201.5 ms with a half-sine-shaped gradient pulse with a width of $\delta = 7.0$ ms. T₂-weighted, spin-echo echo-planar images were acquired for nine different echo

times (10, 20, 40, 60, 80, 100, 150, 200, and 300 ms) with the same imaging parameters used for the diffusion-weighted images.

4.2.5 Data Analysis

Dose response Study

Animals with tumors showing injury were excluded from the study. The tumor doubling time (*TDT*) was determined for each group using the formula (Houchens and Ovejera, 1991)

$$TDT = t_2 - t_1 \quad [4.2.3.1]$$

where t_2 is the time point for the larger volume and t_1 is the time point of the smaller tumor volume. TDT was measured as the tumor volume doubled from initially 0.7 cm^3 to 1.4 cm^3 . A single factor ANOVA test was applied to establish the statistical significance between the treatment groups and the control group.

The time of maximum regression was calculated as the time difference between the time point of the smallest tumor volume after injection of the drug and the time point at which the tumor had a volume of 0.7 cm^3 by

$$TMR = t_{min} - t_1 \quad [4.2.3.2]$$

where t_{min} is the time point of the smallest tumor volume and t_I is the initial time point. Means and standard deviations were calculated for the treatment groups and the statistical significance was evaluated by a single factor ANOVA test.

NMR Measurements

MRI data were analyzed on an Apollo 735 (Hewlett Packard, Palo Alto, CA) computer workstation using in-house software written in C and IDL (Interactive Data Language, Boulder, CO) programming language.

The slope of the signal attenuation curves is linear and deviates little from the Gaussian behavior at small k values. In a previous study, Helmer et al. (1995) found that the diffusion attenuation curves of RIF-1 tumors start to deviate from linearity at a signal attenuation $\ln(M(k,t)/M_0)$ greater than 20%. Hence the ADC maps were calculated on a pixel-by-pixel basis from the initial slope of the $\ln(M(k,t)/M_0)$ versus k^2t signal attenuation curve, where the signal attenuation is smaller than 20%.

The RTO enhancement, $R(k,t)$, was calculated from the complete data set acquired. The RTO probability was generated from Eq. [3.1.2] by numerical integration of the $\ln(M(k,t)/M_0)$ versus k signal attenuation curve on a pixel-by-pixel basis. The result was then inserted into Eq. [3.1.25], using a bulk water diffusion coefficient of 3.0×10^{-5} cm²/sec at 37° C, to determine the RTO enhancement for the creation of the RTO enhancement maps. The tumor temperature was assumed to be equal the body

temperature of the animal (37° C) even if some areas within the tumor may be up to 1.5° C lower.

T₂ maps were generated by fitting the images, acquired at different echo times (TE's), on a pixel-by-pixel basis with a least-squared algorithm to the T₂-relaxation equation

$$M_{xy} = M_0 e^{-\frac{TE}{T_2}} \quad [4.2.5.1]$$

with M_{xy} is the transverse magnetization at the echo time, TE , and M_0 the initial magnitude of the magnetization following a 90° RF pulse applied to a system at the Boltzmann equilibrium.

Histograms of the ADC, RTO-enhancement and T₂ maps, excluding the background, were generated for all tumor maps and normalized by the total non-zero pixel count of the corresponding map. The mean and standard deviation of the mean of the histograms was calculated for each group at each day.

Hematoxylin and eosin (H&E) staining was performed on histological slices from the tumors. Histological slices of ~5-μm thickness were obtained from positions at the top, center and bottom of the corresponding MRI slice. The stained histological sections were then digitized on a computer-based imaging system (Alpha Imager 2000, Alpha Innotech Inc., CA.) and stored for further processing. Necrotic areas were measured by manual

tracing using a personal computer and OPTIMAS (BIOSCAN, Edmonds, WA) image-processing software. The histological sections were then compared to the ADC, RTO-enhancement and T_2 maps to correlate necrotic and viable tissue areas.

4.3 Results

Dose Response Study

Figure 4.3.1 shows the tumor growth curves for three representative RIF-1 tumors, since a plot of all tumors would obscure the displayed features. The control animal (○) shows a steady increase in tumor volume over time, while animals treated with a single dose of

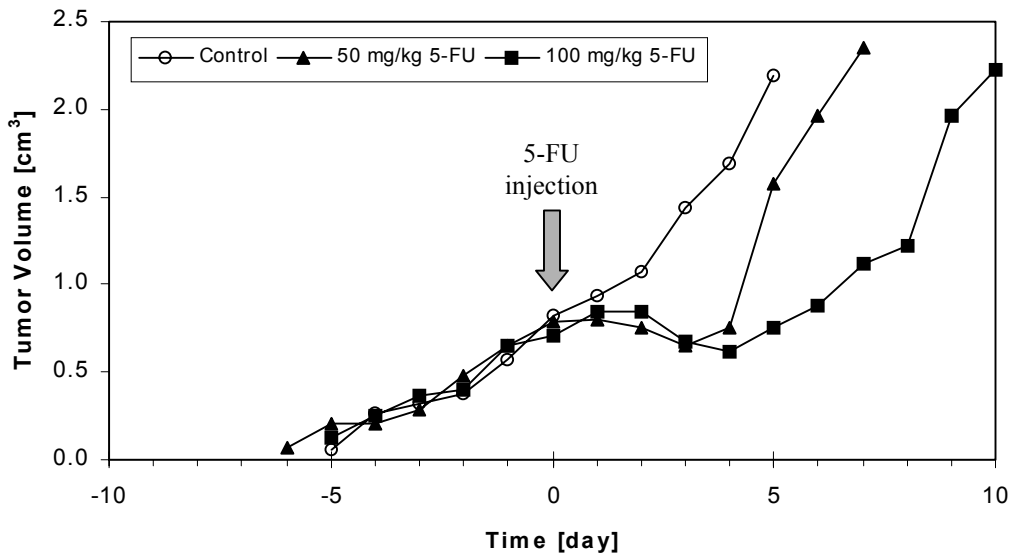


Figure 4.3.1: Plot of tumor volume as a function of time for a representative animal of the control group (○), the with 50 mg/kg 5-Flourouracil (5-FU) treated group (▲), and the with 100 mg/kg 5-FU treated group (■). Tumor volumes were assessed from their first appearance until they exceeded 2.0 cm³. At a volume of 0.7 cm³ (Day 0) control and treatment animals were injected with a placebo and 5-FU, respectively.

50 mg/kg (▲) and 100 mg/kg (■) 5-FU (Day 0) exhibit a transient regression in tumor volume before tumor growth resumes. The calculated TDT for the tumors is displayed in Table 4.3.1 and the mean \pm standard deviation for each group was determined to be 3.1 ± 0.6 days for the control group (n = 9), 5.8 ± 0.6 days (n = 8) and 7.8 ± 0.7 days (n = 6) for the group treated with 50 mg/kg and 100 mg/kg 5-FU, respectively. The statistical significance between the control and drug groups was established by a single factor ANOVA test ($p < 0.0001$) for both treatment groups, taking into account the different number of animals in each group.

The time to maximum regression (TMR) was determined to be 3.1 ± 1.1 days and 3.8 ± 0.4 days (mean \pm SD) for the 50 mg/kg (n = 9) and 100 mg/kg (n = 6) 5-FU treatment groups, respectively. The statistical significance between the TMR for the two treatment

Tumor Doubling Time (TDT) [Days]			
Animal No.	Control Group	Treatment Group	
		50 mg/kg 5-FU	100 mg/kg 5-FU
1	1.91	5.27	7.80
2	3.87	5.73	7.52
3	2.90	5.37	8.72
4	3.54	6.50	6.76
5	3.31	7.05	8.10
6	2.68	4.77	8.19
7	3.45	5.38	
8	2.55	6.36	
9	3.64		
Mean	3.09	5.80	7.84
\pm SD	0.63	0.76	0.66

Table 4.3.1: Tumor doubling time (TDT) of RIF-1 tumors grown on the right hind leg of C3H mice determined at tumor volumes between 0.7 and 1.4 cm³. The column displays the individual TDT for each tumor from the control group and the treatment group of 50 mg/kg and 100 mg/kg 5-FU as well as the mean and standard deviation for the respective groups.

groups was established by a single ANOVA test ($p < 0.015$) taking into account the different number of animals in each group.

NMR Measurement

Figure 4.3.2 displays the generated ADC, RTO enhancement, and T_2 maps of a representative RIF-1 tumor for an animal from the control group as a function of time (days) and volume, as well as the corresponding H&E stained histological section. The section used for histology was obtained at the last day from the same spatial location as the NMR imaging slice. The ADC and RTO enhancement maps show an increase in ADC values and a decrease in the RTO enhancement over the period of five days when the RIF-1 tumor grew from 0.7 to 2.1 cm³. At Day 5 a regression in the ADC values and a slight increase in the RTO enhancement can be observed. The T_2 maps exhibit only small changes over the 5-day observation period. Areas in the ADC and RTO enhancement maps associated with necrotic tissue are represented by high ADC and low RTO enhancement values, while areas of low ADC and high RTO enhancement values are associated with viable tumor tissue. The histological section obtained at the last imaging day displays viable tissue in dark and necrotic tissue in bright gray tones. Visual comparison of the histological section and the generated ADC and RTO enhancement maps at the last day (Day 5) show only general spatial agreement between the MRI parameters and the necrotic regions. No agreement can be found between the necrotic areas and the T_2 maps.

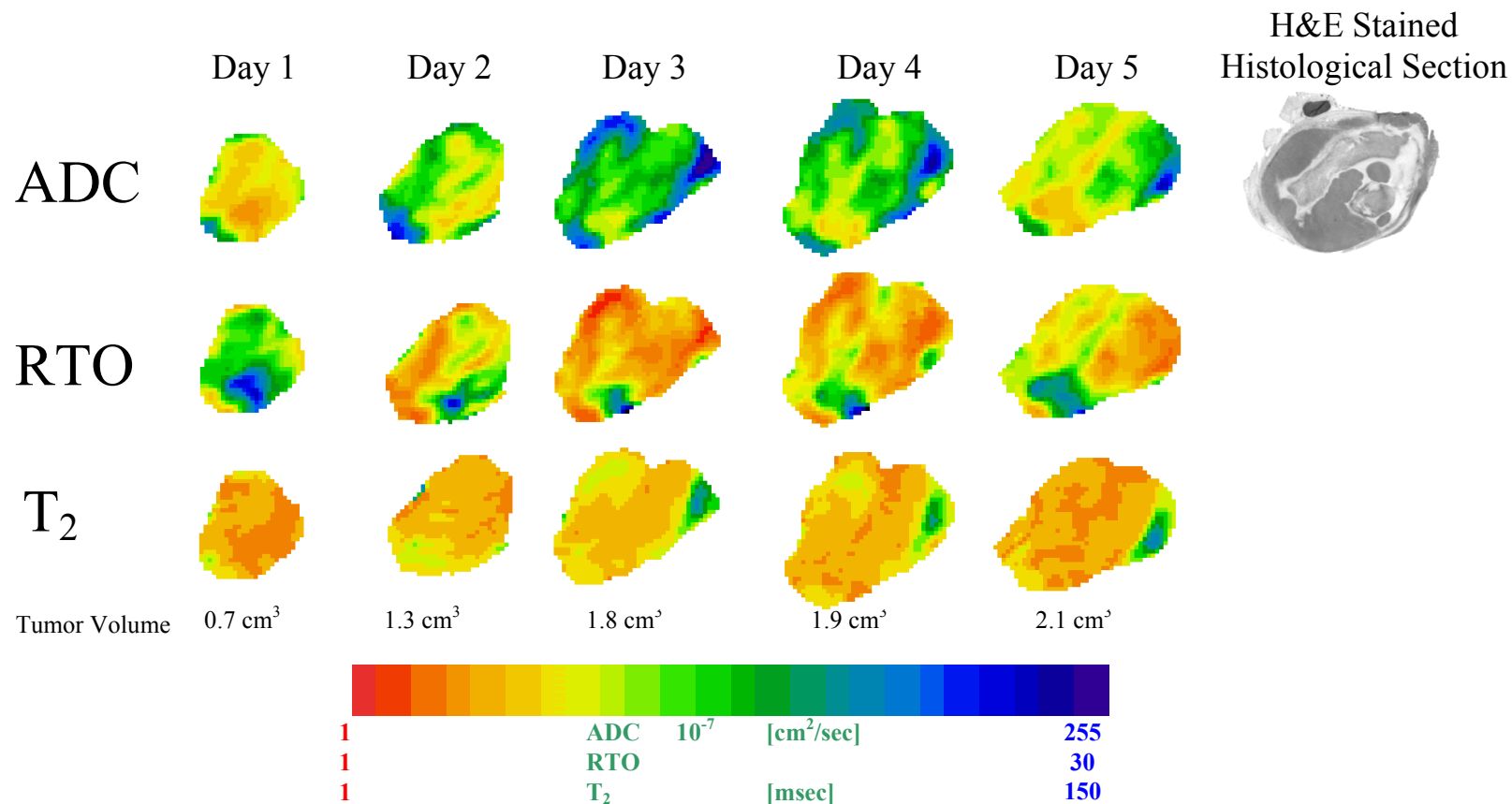


Figure 4.3.2: ADC, RTO enhancement, and T₂ maps as a function of time (days) and volume for a RIF tumor from the control group. The ADC and RTO enhancement maps were acquired with a diffusion-weighted, stimulated-echo echoplanar pulse sequence at a diffusion time of 201.5 ms, a diffusion-gradient duration of 7 ms, and a slice thickness of 3 mm. The T₂ maps were created from nine different images with echo times of 10, 20, 40, 60, 80, 100, 150, 200, and 300 ms. The histological slice from the corresponding location of the MRI slices was obtained at the last day (Day 5) and has a thickness of 5 μ m. Low ADC and high RTO enhancement values are associated with viable tumor tissue while high ADC and low RTO enhancement values are associated with necrotic tumor tissue.

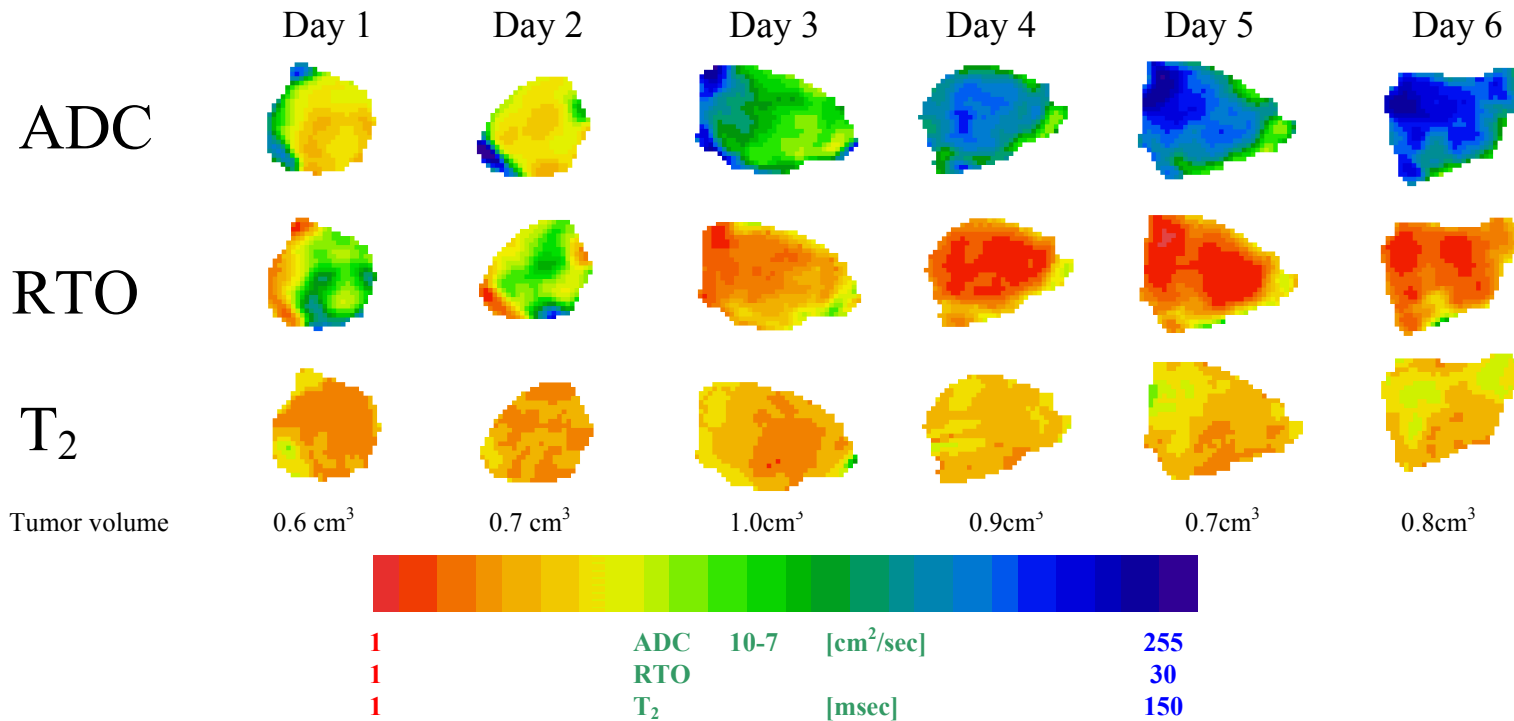


Figure 4.3.3: ADC, RTO enhancement, and T₂ maps as a function of time (days) and volume for RIF-1 tumor from the treatment group. Following the imaging procedure on Day 2, 100 mg/kg of the chemotherapeutic agent 5-Fluorouracil (5-FU) was administered via intraperitoneal injection. The ADC and RTO enhancement maps were acquired with a diffusion-weighted, stimulated-echo echo-planar pulse sequence at a diffusion time of 201.5 ms, a diffusion-gradient duration of 7 ms, and a slice thickness of 3 mm. The T₂ maps were created from nine different images with echo times of 10, 20, 40, 60, 80, 100, 150, 200, and 300 ms. The histological slice from the corresponding location of the MRI slices was obtained at the last day (Day 11) and has a thickness of 5 μm. Low ADC and high RTO enhancement values are associated with viable tumor tissue while high ADC and low RTO enhancement values are associated with necrotic tumor tissue. The figure continues on the next page.

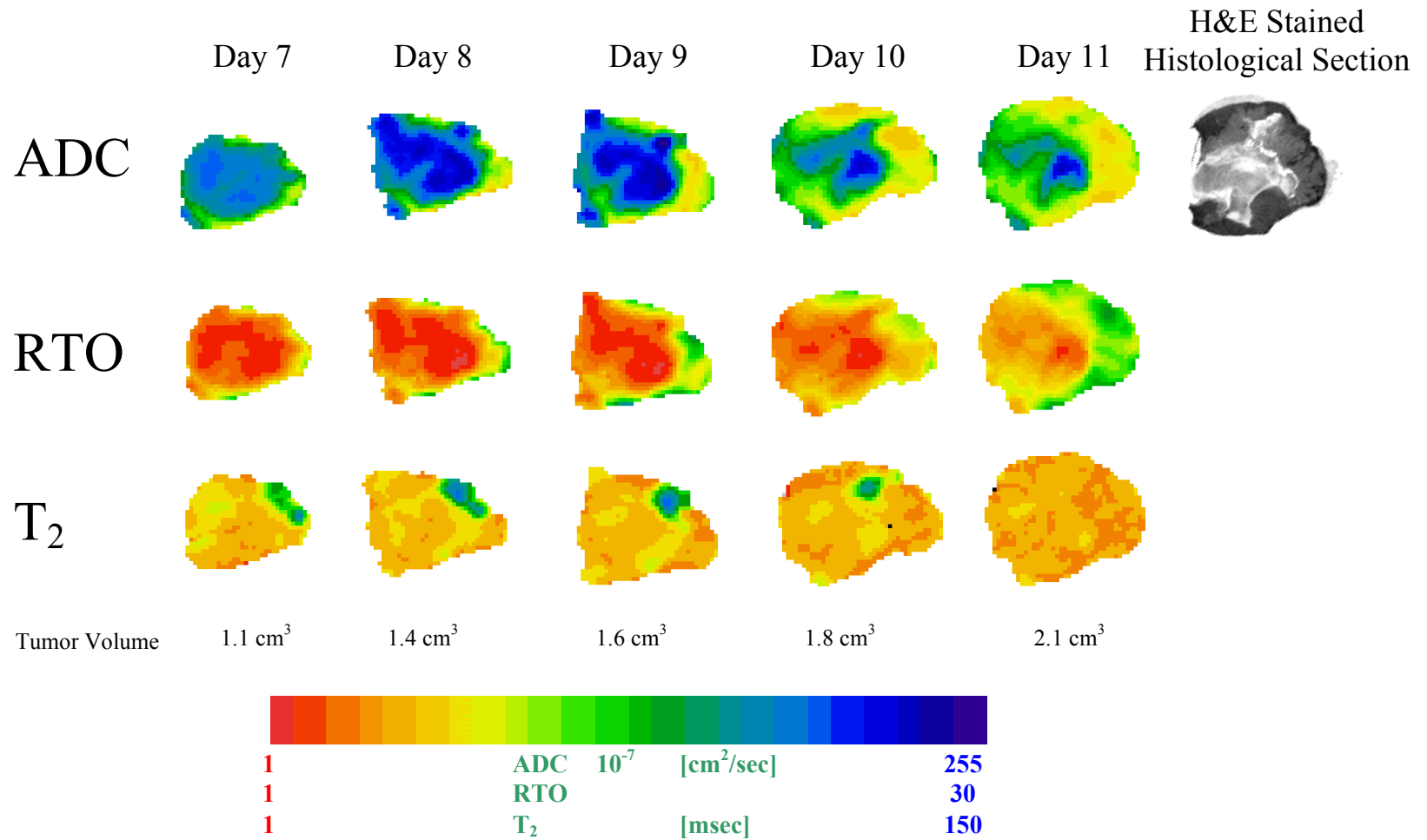


Figure 4.3.3 (cont.): See caption on previous page.

ADC, RTO enhancement and T_2 maps shown in Fig. 4.3.3 as a function of time (days) and volume for a RIF-1 tumor from an animal treated with 100 mg/kg 5-FU, together with the corresponding H&E stained histological section obtained at the last day from the same spatial location as the NMR imaging slice. The maps span an 11-day period and treatment was administered at Day 2 when the tumor volume was 0.7 cm^3 . The maps show an initial overall increase in ADC and decrease in RTO enhancement throughout the tumor and achieve extreme values between Day 5 and Day 6. Thereafter, the overall ADC values decrease and the RTO enhancement increases over the remainder of the observation period. T_2 maps in comparison show only minor changes over the entire observation period.

Figure 4.3.4 shows the histograms of the ADC, RTO enhancement, and T_2 maps for a RIF-1 tumor as a function of time for the control animal data in Fig. 4.3.2. As indicated by the maps, the histograms show a shift towards higher ADC values (Fig. 4.3.4, A) and lower RTO enhancement values (Fig. 4.3.4, B). The relatively narrow distribution from Day 1 disperses over a larger range of values over an observation period of five days. The histograms of the T_2 maps (Fig. 4.3.4, C) show a relatively narrow peak and no shift of the T_2 value distribution over time. At the last day there is a large increase in magnitude but the distribution is still centered around the same values as on the previous days.

Figure 4.3.5 shows the histograms of the ADC, RTO enhancement, and T_2 maps for a RIF-1 tumor as a function of time for data from a animal treated with 100mg/kg 5-FU from Fig. 4.3.3. Histograms of the ADC (Fig. 4.3.5, A) at Day 1 show a distribution

centered around low ADC values, which are associated with viable tissue. After the chemotherapy was administered at Day 2, the distribution shifts towards higher ADC values and is largest between Day 5 and Day 6. Thereafter, the distribution shifts back towards lower ADC values, while the distribution disperses over a wider range of values.

Histograms of the RTO enhancement (Fig. 4.3.5, B) display a behavior similar to that of the ADC histograms. At the first two days, the distribution is centered around high RTO enhancement values associated with viable tissue. After the single dose of 5-FU was administered at Day 2, the distribution shifts towards lower RTO enhancement values, indicative of necrotic RIF-1 tumor tissue, with the largest shift around Day 5. Thereafter, the distribution shifts back towards higher RTO enhancement values over the following day and assumes a wider distribution of values.

The T_2 histograms (Fig. 4.3.5, C) show no shift of the distribution. At the first two days before the chemotherapy was administered, the T_2 -value distribution has a relatively narrow and well-defined peak. Thereafter, the distribution disperses over a wider range of values and the magnitude decreases, with the larger dispersion and smallest magnitude occurring between Day 5 and Day 6. Over the remainder of the days, the width of the distribution and the magnitude return towards their pre-treatment values.

Figure 4.3.6 shows the mean of the histograms from Figs. 4.3.4 and 4.3.5 over time (days) for the control animal and the animal treated with 100 mg/kg 5-FU. The mean ADC of the control animal increases at the first three days and then return towards its

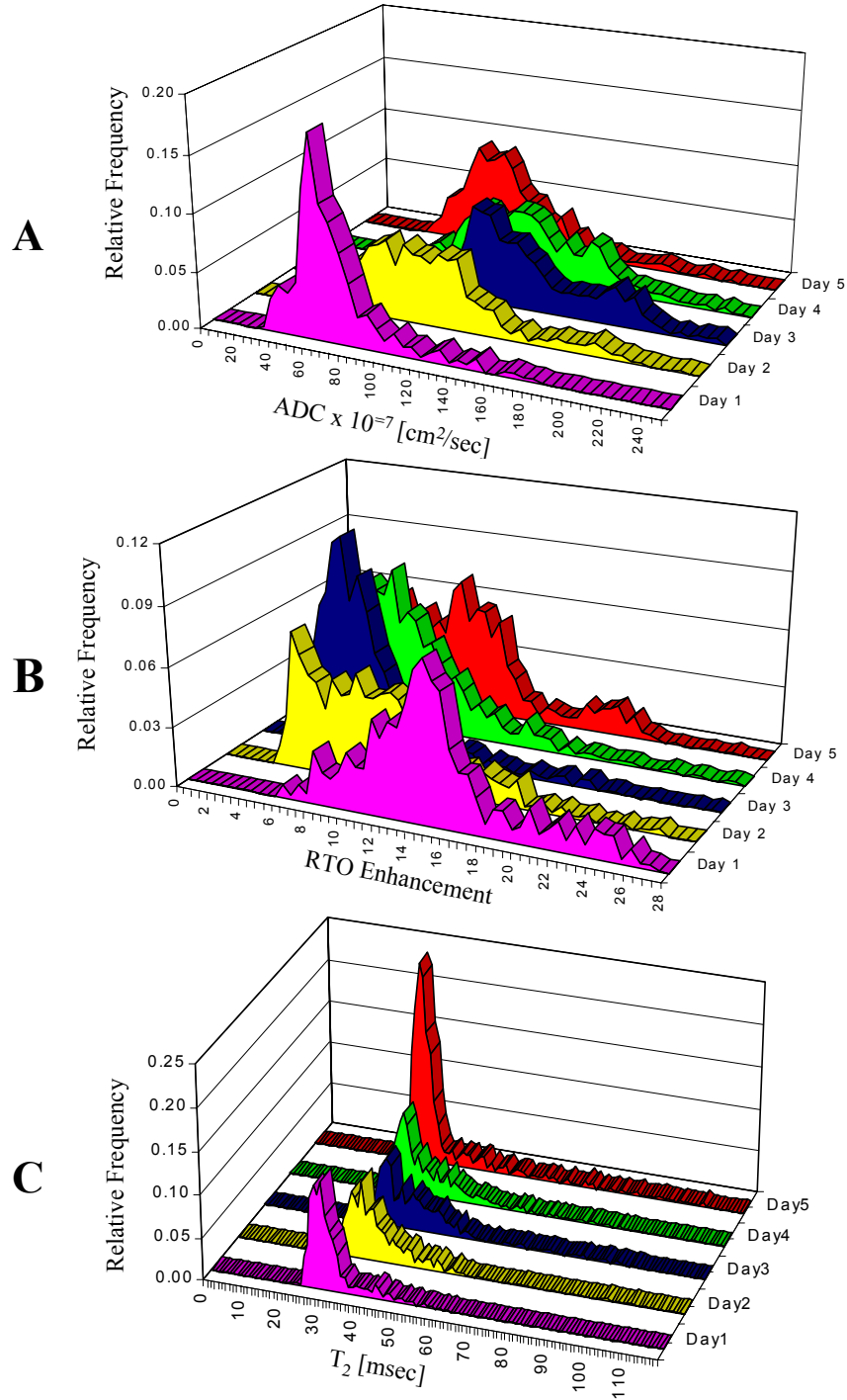


Figure 4.3.4: Histograms of the ADC (A), RTO enhancement (B), and T₂ (C) maps from a RIF-1 tumor as a function of time (days) for data from a control animal (Fig. 4.3.2). The histograms were generated from the 3.0-mm-thick ADC, RTO enhancement and T₂ maps, excluding the background, and normalized by the total non-zero pixel count of the respective map. The spatial location of the imaging slice was kept at a constant location with respect to the isocenter of the instrument, and the tumor was allowed to grow through the imaging plane during the 5-day observation period.

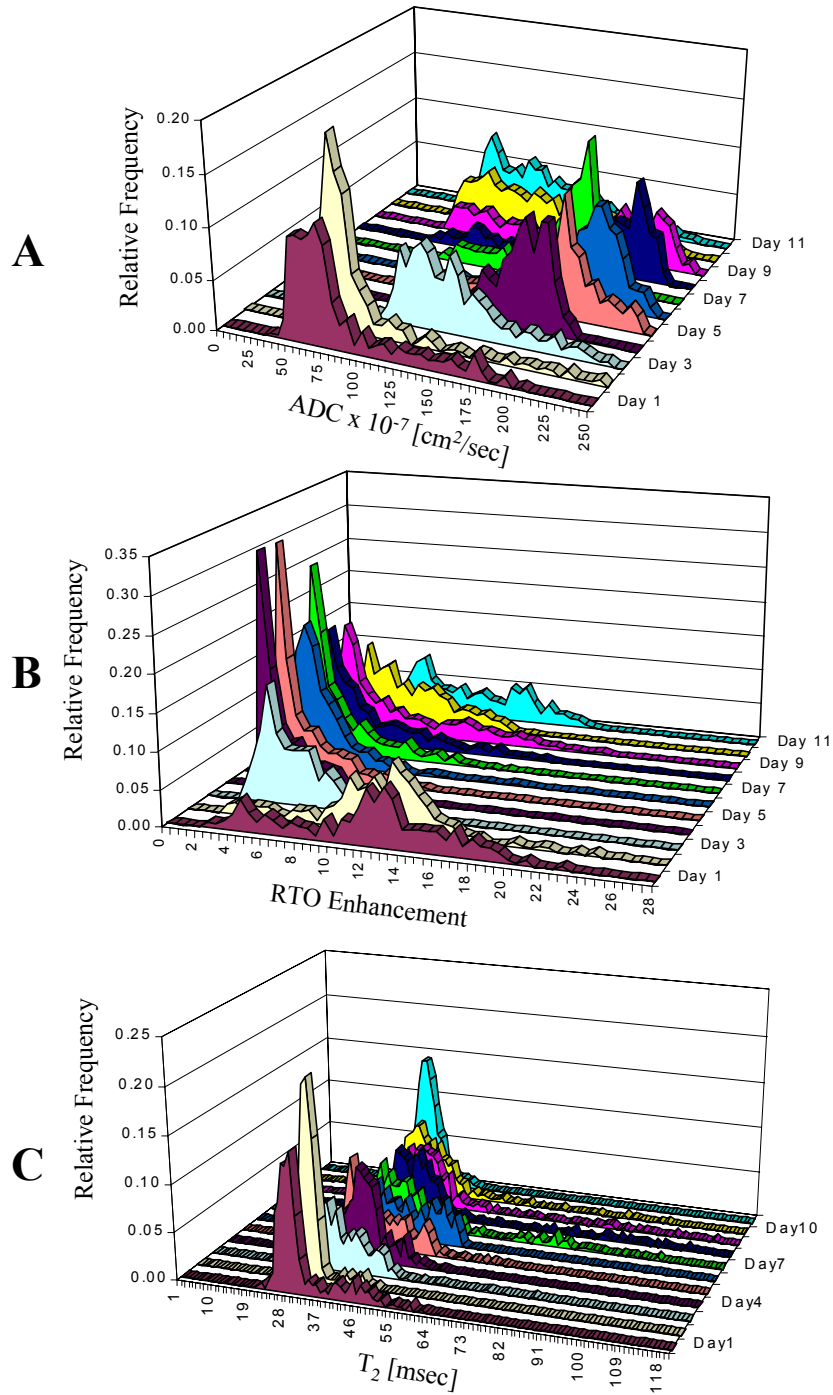


Figure 4.3.5: Histograms of the ADC, RTO enhancement, and T_2 maps from a RIF-1 tumor as a function of time (days) for data from a animal treated with 100mg/kg 5-FU in Fig. 4.3.3. The histograms were generated from the 3.0-mm-thick ADC, RTO enhancement, and T_2 maps, excluding the background, and normalized by the total non-zero pixel count of the respective map. The spatial location of the imaging slice was kept at a constant location with respect to the isocenter of the instrument and the tumor was allowed to grow through the imaging plane during the 11-day observation period.

value of Day 1. The animal treated with 100 mg/kg 5-FU shows a large increase in the mean ADC after the drug was administered at Day 2. Mean ADC values follow the same behavior as observed in the ADC maps and histograms. The largest reduction is seen between Day 4 and Day 6, when the mean is reduced to less than half of the value it had before therapeutic intervention.

Figure 4.3.6, B displays the mean RTO enhancement as calculated from the histograms. For the control animal, the mean RTO enhancement values decrease over the first three days before they recover over the remainder of the 5-day observation period. The mean RTO enhancement of the treatment animal shows a behavior similar to that of the mean ADC. Mean RTO enhancement values decrease after the 5-FU was administered and peaks at Day 6, at twice the value before treatment. Thereafter, the mean RTO enhancement increases towards the higher initial values for the remainder of the 11-day period.

Figure 4.3.7 shows the mean \pm standard deviation of the mean ADC (A), RTO enhancement (B), and T_2 (C) for a RIF-1 tumor plotted over time (days) for the control group ($n = 5$) and the group treated with 100 mg/kg 5-FU ($n = 5$). The plot of the mean ADC (Fig. 4.3.7, A) for five animals shows the difference between the control and treatment group. Mean ADC values of the two groups deviate after drug administration, with the largest separation on Day 6. The mean ADC for the treatment group increases towards a higher mean ADC and is 87% higher at Day 6 compared to the pre-treatment mean ADC. At this time point, the treated tumor volume is approximately equal to the

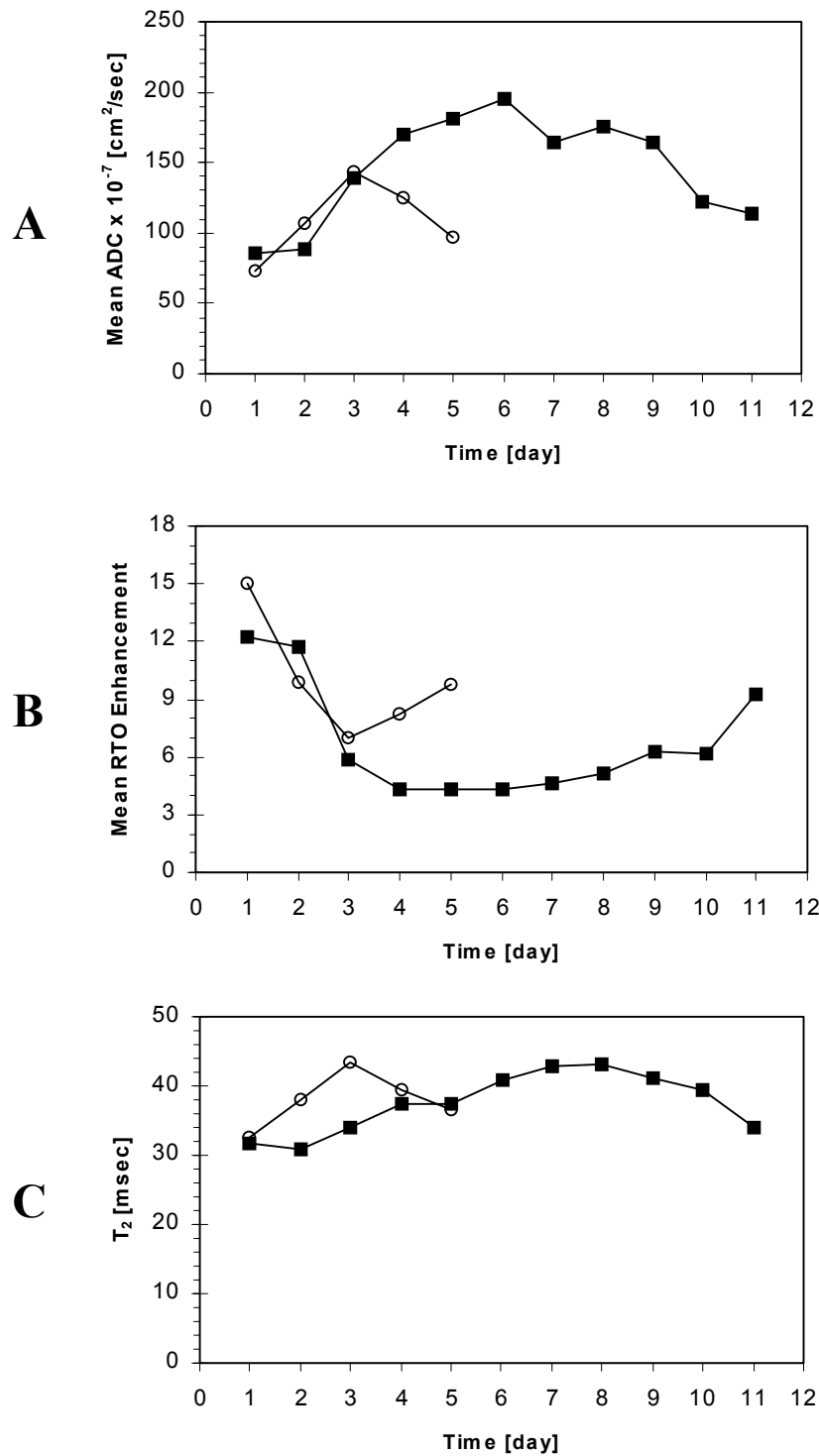
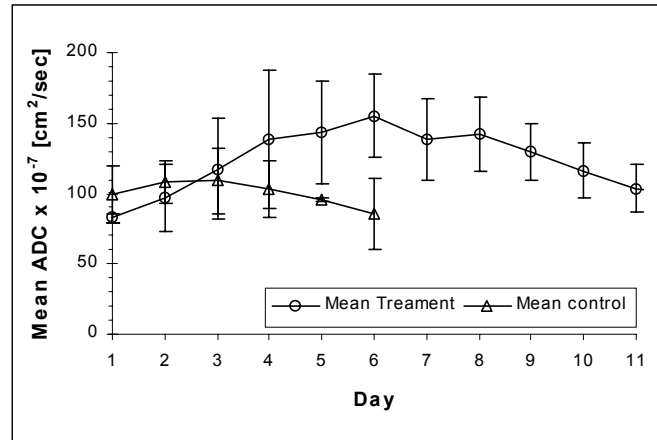
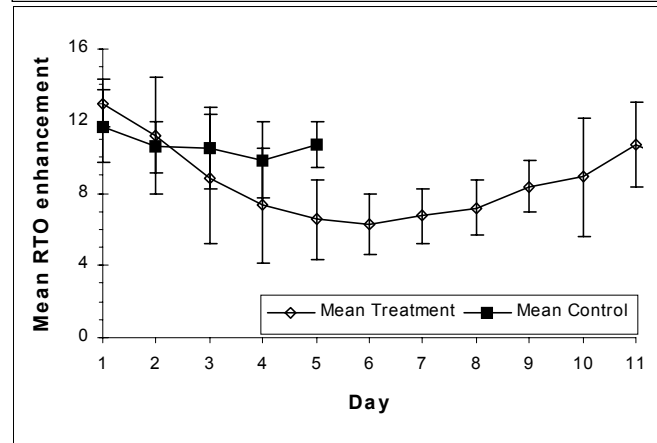


Figure 4.3.6: Mean of the ADC (A), RTO enhancement (B) and T₂ (C) histograms in Figs. 4.3.4 and 4.3.5 plotted over time (days) for the control animal (○) and the animal treated with 100 mg/kg 5-FU (■). Chemotherapy was administered following data acquisition at Day 2. The histograms were generated from the ADC, RTO enhancement, and T₂ maps shown in Figs. 4.3.2 and 4.3.3.

A



B



C

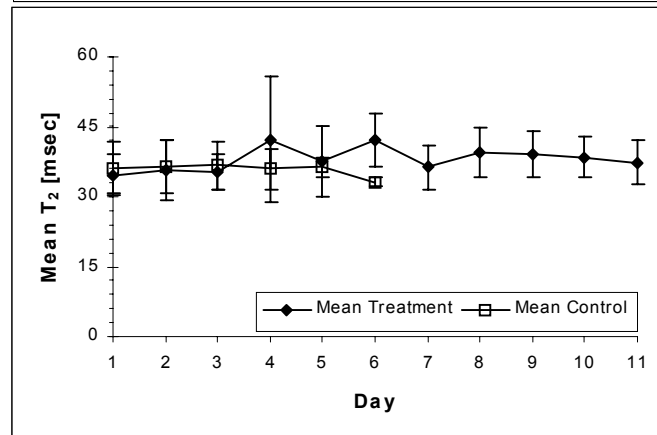


Figure 4.3.7: Mean \pm standard deviation of the mean ADC (A), RTO enhancement (B) and T₂ (C) for a RIF-1 tumor plotted over time (days) for the control group (n = 5) and the group treated with 100 mg/kg 5-FU (n = 5). The means were calculated from the ADC, RTO enhancement, and T₂ maps using a slice thickness of 3.0 mm. Chemotherapy was administered to the animals in the treatment group after the tumor volume was 0.7 cm³. The maps were acquired at a constant spatial location with respect to the isocenter of the instrument and the tumors were allowed to grow through the imaging plane during the observation period of five and 11 days for the control and treatment groups, respectively.

pretreatment volume. Thereafter, the mean ADC decreases over the remainder of the observation period. The mean ADC of the control group shows an increase followed by a slow decrease over time. At the last observation day, when the tumor volumes are similar ($\sim 2.0 \text{ cm}^3$), the mean ADC values for both the control (Day 5) and treatment group (Day 11) are in the same range.

The mean RTO enhancement (Fig. 4.3.7, B) over time exhibits the same behavior as the mean ADC, but in the opposite direction. Mean RTO enhancement values of the control and treatment group deviate after drug administration, with the largest separation between the groups on Day 6. The mean RTO enhancement for the treatment group decreases towards lower values and is smallest on Day 6. At this time, where the tumor volumes are approximately equal, the mean RTO enhancement before treatment is 106% higher than the mean RTO enhancement at Day 6. For the remainder of the 11 days, the RTO enhancement increases towards the initial value. The RTO enhancement of the control animal shows a decline of the mean RTO enhancement, with a slight increase at the last day. At Day 5 and Day 11, the last observation day for the control and treatment group, respectively, when the tumors are similar in volume, the mean RTO enhancement of both groups is same range.

The plot of the mean T_2 over time shows no significant changes for either the control or the treatment group. Both groups stay within a relatively narrow range over the 5- and 11-day periods for the control and treatment group, respectively. The largest change in mean T_2 was observed at Day 6, showing a 17% increase.

4.4 Discussion and Conclusion

Dose Response Study

The plot in Fig. 4.3.1 illustrates the differences in tumor growth for the three groups. Animals treated with 50 and 100 mg/kg 5-FU show a clear reduction in tumor volume after the drug was administered. After the drug level of 5-FU, with a half live of 50 min in RIF-1 tumors (Sijens et al., 1991), decreased to a low enough level, the rapid cell proliferation regains its dominant effect and the tumor volume again increases. Animals treated with 100 mg/kg 5-FU exhibited a longer regression period compared to the animals treated with the lower dose. This prolonged effect in the higher-dose group can be attributed to the increased level of metabolized 5-FU. The TMR for the 100 mg/kg is in agreement with the data shown by Li et al. (1991). The tumor doubling time and time to maximum regression were longest for the animals treated with 100 mg/kg. Consequently, the 100 mg/kg 5-FU dose, which provides a longer time span for observation, was chosen for the NMR experiments.

The reference point for the determination of the tumor doubling time and time to maximum regression was selected to be 0.7 cm^3 . This volume was chosen to characterize the tumor since it is large enough for imaging but usually has only small regions of necrosis despite the usual assessment of the tumor doubling time between 0.1 and 0.2 cm^3 (Houchens and Ovejera, 1991), where the neoplasm has little, if any, necrosis.

NMR Measurement

The imaging maps from a control animal (Fig. 4.3.2) give a good illustration of the

changes in RIF-1 tumor detected by diffusion-weighted MRI. In these maps, the imaging plane was placed at the center of the tumor on Day 1 and kept constant over the observation period. This approach was thought to be more reproducible than keeping the imaging plane in the center of a tumor with changing volume and shape. Therefore, only maps with similar tumor volumes are directly comparable. At Day 1 the relatively small tumor (0.7 cm^3) is comprised of mostly viable tissue, which exhibits low ADC and high RTO enhancement values. As the tumor grows, the development of necrosis results in increasing ADC values with a corresponding decrease in the RTO enhancement. ADC values measured are in agreement with data published Helmer et al. (1995), who found that areas of high ADC correlated with necrotic tissue in the corresponding histological section. The slight reduction of ADC and small increase in RTO enhancement at Day 5 can be attributed to the growth of the tumor through the imaging plane. Viable tissue from the tumor periphery is growing into the imaging plane, replacing the necrotic tissue imaged at earlier time points. The T_2 maps, which are a function of the tissue water content, exhibit only small changes over the 5-day observation period, showing that the range of T_2 values is small in necrotic and viable tissue. H&E-stained histological sections obtained at the last imaging day, from the same spatial location as the imaging slice, show only general spatial agreement of the necrotic regions with the ADC and RTO enhancement maps, while the generated T_2 maps showed little or no agreement.

The ADC and RTO enhancement maps of the treatment group (Fig. 4.3.3) display a different temporal evolution as compared to the control group. On the first day, prior to treatment, the tumor maps have relatively low ADC and high RTO enhancement values

indicative of viable tumor tissue. After the injection of the 5-FU on Day 2 , there is a significant increase in the size of regions in the maps with high ADC and low RTO enhancement values. Extreme values are achieved at the time point (Day 5 and Day 6) where the tumor reaches its smallest volume. The increase in ADC and decrease in RTO enhancement 24 hours after the drug administration is thought to be due to edema, since the tumor volume continued to increase over that time period. Thereafter, as the tumor volume regresses, the changes seen in ADC and RTO enhancement are most likely due to an increase in necrotic tissue and the subsequent removal of the tissue debris. This interpretation is supported by the decrease in tumor volume following the drug administration and the consistently high ADC and low RTO enhancement until the tumor reaches its smallest volume. Sijens et al. (1991) has shown that injection of 5-FU alters the tumor energy metabolism. The decrease energy availability results in hypoxia and subsequent cell death within 48 h after therapeutic intervention.

After the TMR, the overall ADC values decrease and the RTO enhancement increases over the remainder of the observation period. The increase in tumor volume causes the tumor to grow through the fixed imaging plane and hence the sample slice changes with time. T₂ maps of the treated animals show no significant changes over the 11-day observation period.

The structural changes measured by the ADC and the RTO enhancement can also be visualized by inspection of the histograms generated from the maps. The histograms of the control animals (Fig. 4.3.4) show a narrow distribution of low ADC values at Day 1,

representing pixels from viable tissue. The narrow distribution of ADC values decreases over time with a shift in the distribution towards higher ADC values representative of necrotic tumor tissue. The growth of viable tissue into the imaging plane at Day 5, which can be seen in the ADC maps, is recognizable as a shift in the distribution towards lower ADC values. The histograms of the RTO enhancement (Fig. 4.3.4, B) show a behavior similar to that of the ADC. At Day 1, the histogram shows high RTO enhancement values representative of viable tissue. Over the ensuing days, progressively more tissue becomes necrotic, causing the distribution to shift towards lower RTO enhancement values. At Day 5, the pixels associated with tumor necrosis are still visible in the histogram, and pixels from the viable tissue growing into the constant imaging plane show up at high RTO enhancement values. This simultaneous appearance of viable and necrotic tissue causes a wider distribution of the pixels. Histograms of the T_2 maps show little or no shift of the distribution in either direction.

The histograms for the treatment group show the same general tendency as for the control group, since the pathophysiological changes (i.e., necrosis) caused by the effects of 5-FU are similar to the necrotic changes that accompany rapid cell proliferation. In the ADC histogram, the narrow distribution at low ADC values, representing viable tumor tissue, increases at Day 2. On Day 3, 24 hours after the injection of 5-FU, the distribution broadens and shifts towards higher ADC values with the largest shift at Day 6. After Day 6, a reduction of the drug effect allows the growth of new tumor tissue. This growth of viable tissue, together with an upward shift of the tumor core with respect to the imaging plane, results in an increased amount of viable tissue in the (fixed) imaging plane. As

progressively more viable tissue occupies the imaging plane, the ADC shifts to lower values. The RTO enhancement histograms display a complementary behavior. At Day 1, there is a small contribution to the distribution at low RTO enhancement values. The bulk of the distribution is comprised of high RTO enhancement values, which represent viable tumor tissue. Over the time course of the subsequent days, most of the viable tissue becomes necrotic, with a shift in the RTO-enhancement distribution towards lower values. As the therapeutic effects of the 5-FU subside, the growth of viable tissue into the imaging plane results in the shift of the RTO-enhancement distribution to higher values. A comparison of the distributions before treatment and at Day 6, where the tumor volumes equal, shows the large changes in ADC and RTO enhancement induced by chemotherapy. A direct comparison of the histograms with the control group is only possible at days of equal tumor volume as before treatment (0.7 cm^3) and at the endpoint of the study (2.1 cm^3). Comparison at these time points show that the distributions ADC and RTO enhancement for the control and treated animals are similar. This can be expected for the small tumor volume, since at this time point the treatment and control tumor are the same and no therapeutic intervention had taken place. The comparable distributions at the endpoint of the study for the control animal (Day 5, 2.1 cm^3) and the treated animal (Day 11, 2.1 cm^3) suggest that a single bolus injection of 5-FU has no prolonged effects on the tumor. The histograms of the T_2 maps display no visible shift of the distribution over the 11-day observation period. After drug administration, the distribution disperses over a wider range accompanied by a decrease in the magnitude, with the largest dispersion and smallest magnitude at Day 6. Thereafter, the distribution returns to its pre-treatment distribution over the remainder of the time.

Plots of mean ADC, RTO enhancement and T_2 (Fig. 4.3.6) show the same trend observed in the maps and histograms of the control and treated animals. The mean and not the median was used in order to be sensitive to shifts to extreme values exhibited by the three MRI modalities. For both the mean ADC and mean RTO enhancement, mean values calculated from the maps of the control animal show a strong increase in ADC and decrease in RTO enhancement, which is a consequence of increased necrosis due to rapid cell proliferation. As more viable tissue grows into the imaging plane and replaces the necrotic tissue at this location, a regression in the mean ADC and mean RTO enhancement can be observed. The observed increase and subsequent decrease of the mean T_2 is a result of the dispersion of the distribution rather than changing degrees of necrosis.

The plots of the mean ADC, RTO enhancement and T_2 for the animal treated with 5-FU is relatively stable over the first two days (before injection of 5-FU). Within twenty-four hours after the injection of 5-FU (Day 3), the mean ADC showed its high sensitivity to structural changes and increased by 59% with respect to the mean ADC before treatment. The largest change in the mean ADC was observed at Day 6, with an increase of 122% compared to the pre-treatment value. Over the remainder of the observation period of the experiment, the mean ADC shifted slowly back towards ADC values seen in the initial days. This drop in ADC is caused by the progressive growth of viable tissue into the imaging plane in combination with reoccurring rapid cell proliferation. Similar but larger changes can be observed for the mean RTO enhancement. The mean pre-treatment RTO enhancement value is 101% greater than the mean RTO enhancement

measured 24 hours after therapeutic intervention and 171% greater than the minimum value detected at Day 6, when the tumor had its smallest volume. This indicates that the mean RTO enhancement has a higher sensitivity to structural and pathophysiological changes induced by chemotherapy than the mean ADC. It is believed that this increased sensitivity results from highly restricted spins, which have a higher weighting in the calculation of the RTO enhancement compared to the ADC, which is calculated from a composition of highly- and less-restricted spins. The mean T_2 displays only small changes over the 11-day period. At the first day after treatment, the mean T_2 value changes by 10% with respect to the pre-treatment value. The largest change of 18% was observed at Day 6, where the T_2 histogram shows the largest dispersion of the distribution. The observed changes in the dispersion of the distribution are most likely due to the chemotherapeutic intervention.

A plot of the mean \pm standard deviation of the mean ADC, RTO enhancement and T_2 over time (Fig. 4.3.7) for the control group (n=5) and the group treated with 100 mg/kg 5-FU (n=5) show the same behavior observed in the representative animals. The means of the control group show an initial increase in the mean ADC and decrease in the mean RTO enhancement as tumor necrosis increases with tumor volume. The regression of the mean at the last days in the control animals is an artifact of the experiment. As the tumor volume increases over time, viable tumor tissue displaces the necrotic tissue in imaging plane, which was kept at a constant location with respect to the magnet isocenter. This penetration of viable tissue into the imaging plane results in the decrease of ADC and increase of RTO enhancement at the last days. Again, the mean T_2 shows only small

changes and does not differ significantly from that of the treatment group.

The changes in mean ADC and RTO enhancement observed at the first day after drug administration are not as large as those observed in the representative animal. The maximum difference in the averaged mean is still at Day 6, the TMR. It should be noted that the tumor volumes at the point of maximum regression are similar to the initial volume and thus comparable. The mean ADC shows an increase of 87% over the pre-treatment value, while the mean RTO enhancement at pre-treatment is 106% higher than the mean RTO enhancement at Day 6. The variability between tumors of the same group results in a large standard deviation. Over the remainder of the observation period, the mean ADC and RTO enhancement of the treatment group progressively returns to its initial value. The plot of the mean T_2 for the treatment group shows only small changes over the 11-day period and illustrates clearly the insensitivity of the T_2 maps to chemotherapeutic intervention.

This study demonstrates that diffusion-weighted MRI is sensitive to structural changes that accompany tumor growth and treatment and that these changes can be visualized using ADC and RTO enhancement maps. The high sensitivity of both diffusion-weighted metrics compared to conventional T_2 -weighted MRI enables the early detection of therapeutically-induced changes at an early time point in therapy. The RTO enhancement is, however, more sensitive than the ADC implying that a measure of water diffusion that is weighted towards highly restricted spins is a better measure of tissue viability than is a parameter that reflects both unrestricted and restricted water molecules. In spite of that,

the ADC data set (which is a subset of the RTO data set) has the advantage of shorter acquisition times and the smaller diffusion gradient values necessary for data collection. The ability of the ADC and the RTO enhancement to differentiate between viable and necrotic tissue could be especially useful in defining dynamic changes in tumors in response to therapeutic intervention at early time points in the course of treatment.

Chapter 5

**The Diffusion Coefficient Measurement as a
Function of the Diffusion Gradient
Duration**

5.0 The Diffusion Coefficient Measurement as a Function of the Diffusion Gradient Duration

The measurement of the tissue water diffusion coefficient by pulsed-field-gradient (PFG) NMR is an important tool for the detection of pathophysiological changes in cancer and stroke. Measurements of the diffusion coefficient on clinical MRI systems have been limited by the maximum gradient strength available on these systems. The limited gradient strength requires the lengthening of the diffusion gradient duration, δ , to ensure sufficient signal attenuation for the calculation of the diffusion coefficient. Diffusion coefficient measurements that are not in the narrow-pulse regime ($\delta \ll \Delta$, where Δ is the diffusion gradient separation time), but rather in the constant-gradient regime ($\delta \sim \Delta$), violate the experimental conditions of the diffusion experiment as described by Stejskal and Tanner (1965) and thus need to be interpreted differently.

The goal of these experiments was to show the dependence of the measured diffusion coefficient, $D(t)$, on the gradient-pulse duration, δ . I was responsible for the animal preparation, data acquisition and modification of some of the experiments as well as a minor part of the data analysis.

Parts of the experiments were presented at the Experimental NMR Conference (ENC) Meeting 1997 (Helmer et al., 1997) as a poster entitled "Experimental Determination of Finite Pulse Width Effects in Diffusion Coefficient Measurements."

5.1 Introduction

Most of the early diffusion measurements using NMR were performed in the presence of a constant magnetic field gradient (Hahn, 1950; Carr and Purcell, 1954; Torry, 1956). This means that the diffusion-gradient duration is on the order of the diffusion-gradient separation ($\delta \sim \Delta$). Although most of the early diffusion experiments were done in homogeneous, bulk liquid, the influence of spatial restrictions on the measured diffusion coefficient has been recognized and considered in the early history of these measurements (Woessner, 1963; Robertson, 1966; Wayne and Cotts, 1966; Murday and Cotts, 1966). The breakthrough for NMR diffusion measurements came with the

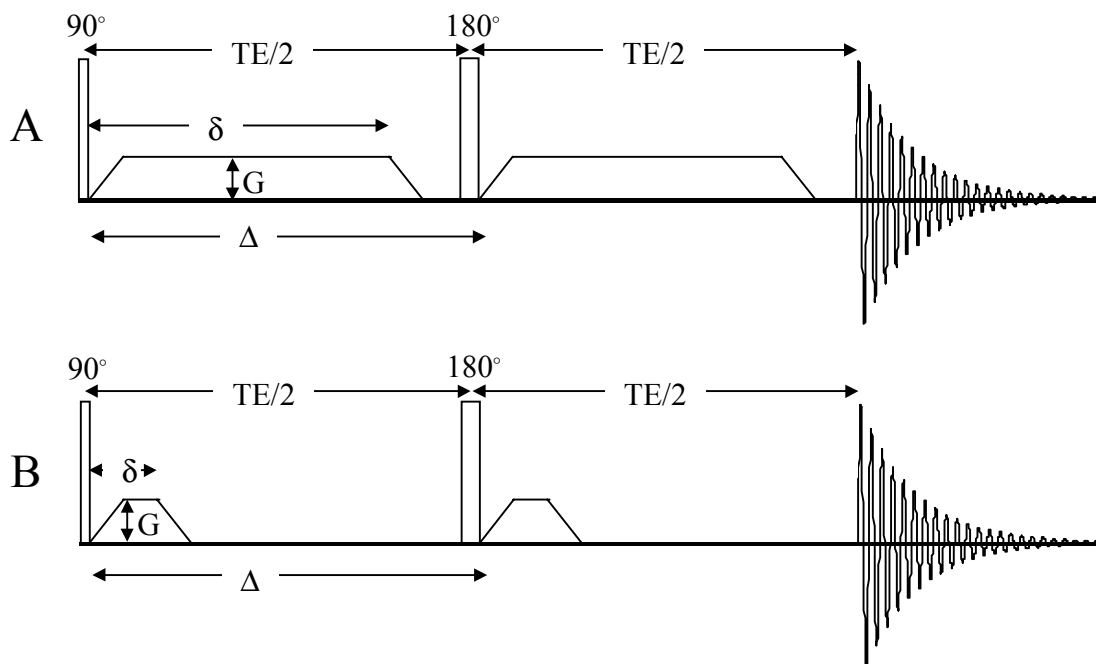


Figure 5.1.1: Two different NMR pulse sequences used to measure the diffusion coefficient. Sequence A is an example of a constant-gradient pulse sequence characterized by the long diffusion gradient duration, δ , for such a sequence is on the order of the diffusion gradient separation, Δ . Sequence B is a typical pulsed-field-gradient diffusion sequence (Stejskal and Tanner, 1965), characterized by the short diffusion gradient duration, δ , with respect to the diffusion-gradient separation time, Δ .

introduction of the pulsed-field-gradient (PFG) diffusion measurement (Stejskal and Tanner, 1965, Stejskal, 1965; Tanner and Stejskal, 1968), which is still widely used today. An example of a constant-gradient diffusion sequence and a pulsed-field-gradient sequence is shown in Fig. 5.1.1. Sequence A is a constant-gradient diffusion sequence characterized by the long diffusion-gradient duration, δ , which is in the order of the diffusion-gradient separation time, Δ . The pulsed-field-gradient sequence (Fig. 5.5.1, B), is characterized by very short diffusion-gradient durations, δ . Diffusion-gradient pulses are switched on only for very short periods of time to establish the initial and final position of diffusing molecules. The diffusion-gradient separation in such pulse sequences is much longer than the diffusion gradient duration ($\Delta \gg \delta$).

With the advent of NMR imaging for medical applications, diffusion has gained importance since the detection of many diseases is based on changes in tissue microstructure. These changes in microstructure have been exploited in the detection of structural tissue changes in cancer and stroke research. The biological tissue contains cell membranes and organelles, which present barriers to water diffusion, reducing the displacement of water molecules. Since NMR diffusion experiments measure the mean-squared displacement of an ensemble of water molecules due to thermal motion, a reduction in the displacement alters the measured diffusion coefficient.

In the PFG diffusion measurement, a gradient pulse of short duration is applied to impart a phase that depends on the position on the spins and after at time, t , a second gradient pulse of short duration removes the same amount of phase. Signal from spins that have

not diffused away from their initial position will be unaffected by this operation, while the signal from spins that have moved will be attenuated. The resulting signal attenuation of the detected signal is a function of the area under the curve of the gradient pulse and the temporal separation between the short gradient pulses. The attenuation of the detected signal due to diffusion is given by

$$M(\vec{k}, t) = M_0 e^{-\vec{k}^2 D t} \quad [5.1.1]$$

where

$$\vec{k} = \gamma \vec{G} \delta, \quad [5.1.2]$$

$M(\vec{k}, t)$ is the measured NMR signal, M_0 is the initial signal without attenuation, D is the diffusion coefficient, t is the diffusion time, γ is the gyromagnetic ratio, \vec{G} is the applied diffusion gradient strength, and δ is the diffusion-gradient pulse duration. Inspection of Eq. [5.1.1] shows, that the signal attenuation for a given diffusion time depends on \vec{k} and the diffusion coefficient, which is proportional to the mean-squared displacement, as described by the Einstein relation. The diffusion coefficient can be extracted from the slope of the signal attenuation curve $\ln(M/M_0)$ versus $k^2 t$.

In order to achieve sufficient signal attenuation to accurately measure the diffusion coefficient, \bar{k} has to be increased. According to Eq. [5.1.2] there are only two ways to adjust the signal attenuation - the diffusion gradient strength and the diffusion gradient duration. With γ , the gyromagnetic ratio, constant and the applied diffusion gradient, G , limited by technical considerations, only the diffusion pulse duration, δ , can be increased to gain sufficient signal attenuation for an accurate calculation of the diffusion coefficient, $D(t)$. In clinical MRI systems with low diffusion gradient strength, the signal attenuation has to be achieved by increasing the diffusion gradient duration, a violation of the narrow-pulse width criteria ($\delta \ll \Delta$). The experiment is now no longer in the finite-pulse width regime but rather in the constant gradient regime ($\delta \sim \Delta$). The influence of the narrow-diffusion-gradient pulse-width criterion and its importance for the interpretation of many experiments has been studied by several groups (Bless, 1993; Mitra and Halperin, 1994; Wang et al., 1995) in order to provide an analytical expression for measurements in the restricted-diffusion regime.

Diffusion measurements in the presence of a constant gradient were first discussed by Hahn (1950) who found that the signal attenuation is

$$\frac{M(G, \tau)}{M_0} = e^{-\frac{2}{3} D_0 \gamma^2 G^2 \tau^3} . \quad [5.1.3]$$

where τ is half of the echo-time.

The signal attenuation equation for restricted diffusion in a constant-gradient field was described theoretically (Robertson, 1966) and experimentally (Wayne and Cotts, 1966) much later. These investigators concentrated on cases involving weak diffusion gradients and small restricting volumes, where diffusing spins are restricted before they exhibit significant dephasing.

Diffusion in the presence of restricting barriers can be characterized based on three different parameters (Hürlimann et al., 1995). 1) The diffusion length

$$l_D \equiv \sqrt{D_0 t} \quad [5.1.4]$$

which is the average distance a molecule diffuses during the time, t . D_0 is the bulk diffusion coefficient and t is the diffusion time. 2) The dephasing length

$$l_G \equiv \sqrt[3]{\frac{D_0}{\gamma G}} \quad [5.1.5]$$

which is the distance a molecule has to diffuse in the applied gradient field to gain a phase of 2π . Molecules gaining a phase larger than 2π can no longer be differentiated from molecules gaining only a small phase. In this case, G is the applied diffusion gradient strength, γ the gyromagnetic ratio, and D_0 is the bulk diffusion coefficient.

3) The structural length, l_s , which is the characteristic length scale of the pore space or structure in the confining geometry.

In the first or free-diffusion regime ($l_D < l_G, l_s$), where the diffusion length, l_D , is shorter than the dephasing length, l_G , and shorter than the structural length, l_s , the signal decays according to the Hahn expression (Hahn, 1950) for free diffusion in a constant gradient field by

$$\frac{M(G, \tau)}{M_0} = e^{-\frac{2}{3} D_0 \gamma^2 G^2 \tau^3} = e^{-\frac{3}{2} \left(\frac{l_D}{l_G} \right)^6}. \quad [5.1.6]$$

In the second or motion-averaging regime, diffusing molecules have crossed the pore/structure space many times and therefore have fully experienced the restrictions. In this regime the attenuation has been described by Robertson (1966)

$$\frac{M(G, \tau)}{M_0} = e^{-\frac{1}{120} \frac{\gamma^2 G^2 l_s^4 2\tau}{D_0}} = e^{-\frac{1}{60} \left(\frac{l_D}{l_G} \right)^2 \left(\frac{l_s}{l_G} \right)^4}. \quad [5.1.7]$$

The equation holds for various geometries; however, the numerical prefactor in the exponent must be modified depending upon the specific geometry (Neuman, 1974). The third regime is where the dephasing length, $l_G < l_D, l_s$, is smaller than the diffusion

length, l_D , as well as the structural length, l_S . In this regime the signal arises predominantly from spins in proximity to restricting walls, where boundaries have reduced their displacement and hence their dephasing during the experiment. Spins not confined by boundaries exhibit larger displacements and therefore are completely dephased during the diffusion measurement, and thus do not contribute to the resulting signal. The decaying magnetization in this regime, at long diffusion times, is given by (Swiet et al., 1994).

$$\frac{M(G, \tau)}{M_0} = c \frac{D_0^{2/3}}{\gamma^{1/3} G^{1/3} l_S} e^{-a_1 D_0^{1/3} \gamma^{2/3} G^{2/3} \tau} = c \frac{l_G}{l_S} e^{-a_1 \left(\frac{l_D}{l_G} \right)^2} \quad [5.1.8]$$

with $-a_1 = -1.018\bar{8}$ and c is a constant depending on the geometry of the restriction.

Considering the above regimes, it has often been argued that the Hahn formula (Eq. [5.1.6]) for unrestricted diffusion at short diffusion times is applicable to a sample where diffusion is restricted since diffusing spins have not traversed the structural space. Recent studies have shown (Stoller et al., 1991; Swiet and Sen, 1994; Hürliman et al., 1995) that the application of the Hahn formula to restricted diffusion is only valid at small diffusion gradient values with small dephasing.

When comparing the attenuation decay for the constant-diffusion-gradient experiment with that of the PFG-diffusion experiment, it becomes apparent that there are significant

differences. With increased gradient duration, there is significant diffusion during the diffusion-sensitizing gradient. Diffusion measurements in a finite-diffusion-pulse experiment will display a smaller diffusion coefficient (Mitra et al., 1995) due to the increased contribution of restricted molecules to the signal. Diffusion measurements performed under constant-gradient conditions will show a higher diffusion coefficient since restricted spins make a smaller contribution to the signal.

In addition to the different weighting of spin populations, arising from restricted and less restricted areas of the sample, the longer TE periods needed to accommodate longer diffusion gradient duration result in an additional loss of spins displaying a short T_2 relaxation. This in turn leads to a further increase in the measured diffusion coefficient since spins with short T_2 relaxation are usually associated with molecules in more restricted environments, which have smaller ADC's.

The different weighing of spins in the finite- and constant-diffusion gradient experiment leads to differences in the diffusion coefficient. The goal of this study was to compare experimental results obtained in the finite- and constant-gradient regime for biological systems, which contain restricting structures.

5.2 Experimental Methods

5.2.1 Animal preparation

All experiments and procedures were approved by the Animal Research Committee (ARC) of the University of Massachusetts Medical School. Animals were housed under diurnal lighting conditions and allowed free access to food and water before and after the NMR experiment. Eight-week-old, female C3H mice (Taconic Farms, Germantown, NJ) were anesthetized by intraperitoneal injection of 320 mg/kg chloral hydrate. The lower back was shaved and the remaining hair removed with a commercial hair remover (NAIR, Carter Wallace Inc., New York, NY).

Radiation induced fibrosarcoma cells, RIF-1 (Twentyman et. al., 1986), of the second passage, suspended in Waymouth's medium supplemented with 15% v/v glycerol, were stored in liquid nitrogen. Prior to inoculation the frozen cells were defrosted at room temperature and 0.15 ml of the solution containing $\sim 1 \times 10^5$ cells were subcutaneously injected into the lower back of the animal with a 30-gauge hypodermic needle. RIF-1 tumors were allowed to grow to a range of 0.4 to 3.0 cm^3 . The tumor volume was determined by measuring the three major orthogonal axes with slide calipers and the volume was calculated to be

$$Volume = \frac{\pi}{6} \times Length \times Width \times Height \quad [5.2.1.1]$$

assuming an ellipsoidal volume (Euhus et al., 1986; Tomayko and Reynolds, 1989).

For data acquisition, anesthesia was induced with 2% isoflurane delivered in air at 1 l/min and maintained at 1.5% isoflurane at the same flow rate. The body temperature was maintained at 37° C by circulating 34° C warm air through the stereotax, controlled with a T-type temperature probe (Omega, Stanford, CT) and a two-point feedback system.

5.2.2 NMR Measurements

Spectroscopic data were acquired using a horizontal bore GE CSI-II 2.0 T 45-cm imaging spectrometer operated at 85.56 MHz for protons, equipped with ± 20 G/cm self-shielded gradients and a four-turn solenoidal RF coil with 15-mm inner diameter.

Four distinct pulse sequences, as depicted in Fig. 5.2.2.1, were used for data acquisition. NMR data from the spin-echo sequences were acquired with a repetition time, $TR = 10$ s, six different half echo times, $TE/2 = 6.5, 11.5, 21.5, 46.5, 81.5$ and 126.5 ms, a spectral width, $SW = \pm 2000$ Hz, four signal averages ($NEX = 4$) and 2048 data points.

The first sequence in Fig. 5.2.21 was used to simulate a constant-gradient experiment. The trapezoidal diffusion gradient fills the entire $TE/2$ period except for a 1.5 ms delay after the first diffusion gradient to allow the eddy currents generated by the diffusion

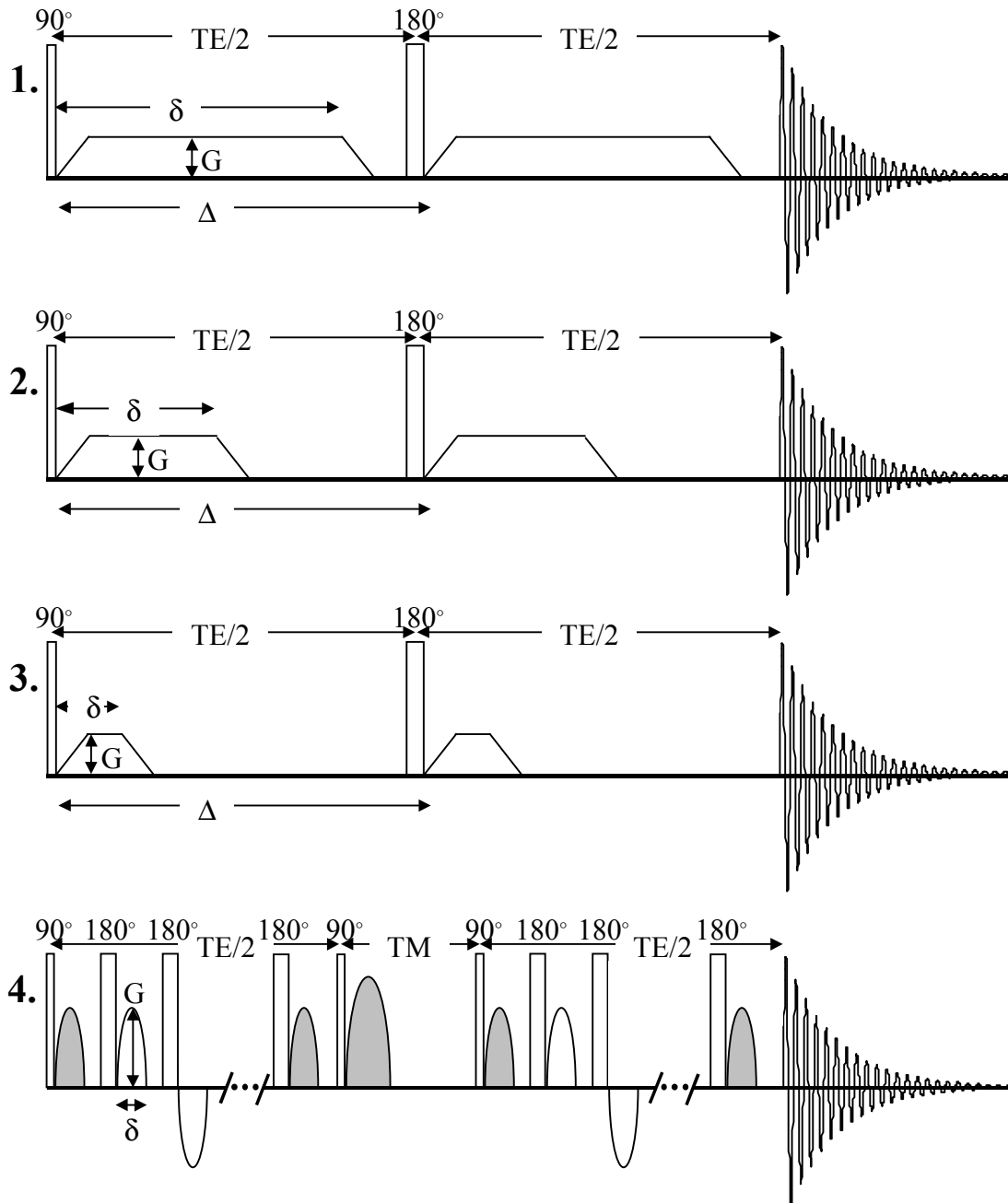


Figure 5.2.2.1: The four different pulse sequences used to obtain experimental data for comparison of the narrow pulse width and constant gradient regime. 1. Spin-echo sequence for the constant gradient experiment. 2. Spin-echo sequence with a gradient length of $TE/4$. 3. Spin-echo sequence with short, constant diffusion gradient. 4. Modified stimulated-echo sequence to cancel the effects of background gradients and narrow diffusion gradient. The filled, gray-shaded gradients are crusher gradients.

gradient to decay. The second spin-echo sequence in Fig. 5.2.2.1 was similar to the first sequence but with the diffusion gradient filling only half the TE/2 period. The third spin-echo sequence in Fig. 5.2.2.1 was a short diffusion-gradient pulse sequence. The diffusion-gradient duration for this sequence was kept constant at $\delta = 5$ ms and the TE/2 period was chosen to be equal to the previous two sequences, while including the T₂-relaxation effects present in the constant gradient (Sequence 1) and half-constant-gradient (Sequence 2) experiments. Data for the constant-gradient, half-constant gradient and narrow-gradient experiments were acquired using a spectral width, SW = ± 2000 Hz, a repetition time, TR = 10 s, four signal averages (NEX = 4), 2048 data points and six TE periods of 6.5, 11.5, 21.5, 46.5, 81.5 and 126.5 ms. The fourth sequence in Fig. 5.2.2.1 is a modified stimulated-echo sequence (Latour et al., 1993) used to cancel the effects of internal background gradients present during the experiment. The cancellation was achieved by separating pairs of gradient pulses of opposite polarity by 180° RF pulses in each of the two TE/2 periods. Two pairs of diffusion gradients were used with a diffusion pulse duration, δ , of 1.5 ms. Data were acquired using the fourth sequence over a range of 12 diffusion times between 13.1 and 613.1 ms with a repetition time, TR = 10 s, an echo time of, TE = 20 ms, a spectral width, SW = ± 2000 Hz, four signal averages (NEX = 4) and 2048 data points. This sequence minimized both the finite-pulse-width effects and the T₂ decay present in the spin-echo experiments.

5.2.3 Data Analysis

The signal attenuation for the four sequences employed in these experiments are given by the following equations. These equations are corrected for the shape of the diffusion gradient pulses (Price and Kuchel, 1991). For the spin-echo sequences with a rectangular gradient pulses with pulse edges, the signal attenuation is given by

$$\frac{M}{M_0} = e^{-\gamma^2 D G^2 \left\{ \delta^2 \left(\Delta - \frac{\delta}{3} \right) + B \right\}} \quad [5.2.3.1]$$

with the correction factor

$$B = \frac{1}{30} \varepsilon^3 - \frac{1}{6} \delta \varepsilon^2 \quad [5.2.3.2]$$

where M is the measured signal, M_0 is the signal without diffusion attenuation, D is the diffusion coefficient, G is the diffusion gradient strength, γ is the gyromagnetic ratio, δ is the diffusion gradient duration inclusive of one rise time, ε is the diffusion-gradient ramp time and Δ is the diffusion-gradient separation. For the modified stimulated-echo sequence with half-sine-shaped diffusion gradients, the signal attenuation is given by

$$\frac{M}{M_0} = e^{-k^2 D t} \quad [5.2.3.3]$$

with

$$k = 4\gamma G\delta(2n) \quad [5.2.4.4]$$

and

$$t = \Delta - \frac{\delta}{4} - \frac{TE}{6} \quad [5.2.3.5]$$

where M is the measured signal, M_0 is the signal without attenuation, D is the diffusion coefficient, G is the diffusion gradient strength, γ is the gyromagnetic ratio, δ is the diffusion-gradient duration, n is the number of gradient pairs, Δ is the diffusion-gradient separation, TM is the evolution time, and TE is the echo time.

The diffusion coefficient, $D(t)$, for all sequences was extracted from the slope of a plot of $\ln(M/M_0)$ versus the exponent of Eq. [5.2.3.1] for the trapezoidal diffusion gradients and Eq. [5.2.3.3] for the half-sine-shaped diffusion gradient.

5.3 Results

Figures 5.3.1 through 5.3.3 show data for RIF-1 tumors with three different volumes. The volumes of the tumors were 1.6, 2.6 and 3.0 cm³, respectively. The upper graph of each figure shows the measured diffusion coefficient, $D(t)$, of the spin-echo sequences with a constant (●), half-constant (▲) and the narrow diffusion gradient (■) for diffusion times varying from 4 to 133 ms. In each of the plots, the diffusion coefficients measured with

the constant-gradient sequence and the half-constant-gradient sequence diverge from those measured with a narrow diffusion gradient. Examination of the graphs reveals that for the two largest tumor volumes (2.6 and 3 cm³), the diffusion coefficients measured with a constant and half-constant gradient diverge from the diffusion gradients measured with a narrow gradient at a diffusion time of approximately 20 ms. For the smallest tumor volume, the divergence of diffusion coefficients from the narrow gradient experiment occurs around 60 ms. At larger diffusion times, the diffusion coefficients measured with a constant and half-constant gradient start to increase in value, while the diffusion coefficient for the narrow diffusion gradient levels out at a constant value.

The lower graphs of Figs. 5.3.1 through 5.3.3 display the diffusion coefficients measured with a narrow diffusion gradient over a larger range of diffusion times varying from 16 to 613 ms. For all three tumor volumes, the diffusion coefficient curves level out at constant value which represents the effective diffusion coefficient, D_{eff} , of the tumor. The value of D_{eff} displays some proportionality to the tumor volume as D_{eff} is highest for the largest tumor volume and lowest for the smallest tumor volume.

Figure 5.3.4 illustrates the effects of the finite pulse width and added T_2 on the diffusion coefficient. The upper graph shows the diffusion coefficients measured with a constant (●) and a narrow (■) diffusion gradient in a spin-echo experiment as well as the diffusion coefficients measured with the modified stimulated-echo sequence (▲). Data acquired with the modified stimulated-echo sequence allow relatively short diffusion gradient pulses, thus minimizing the finite-pulse width effects and T_2 -decay during the

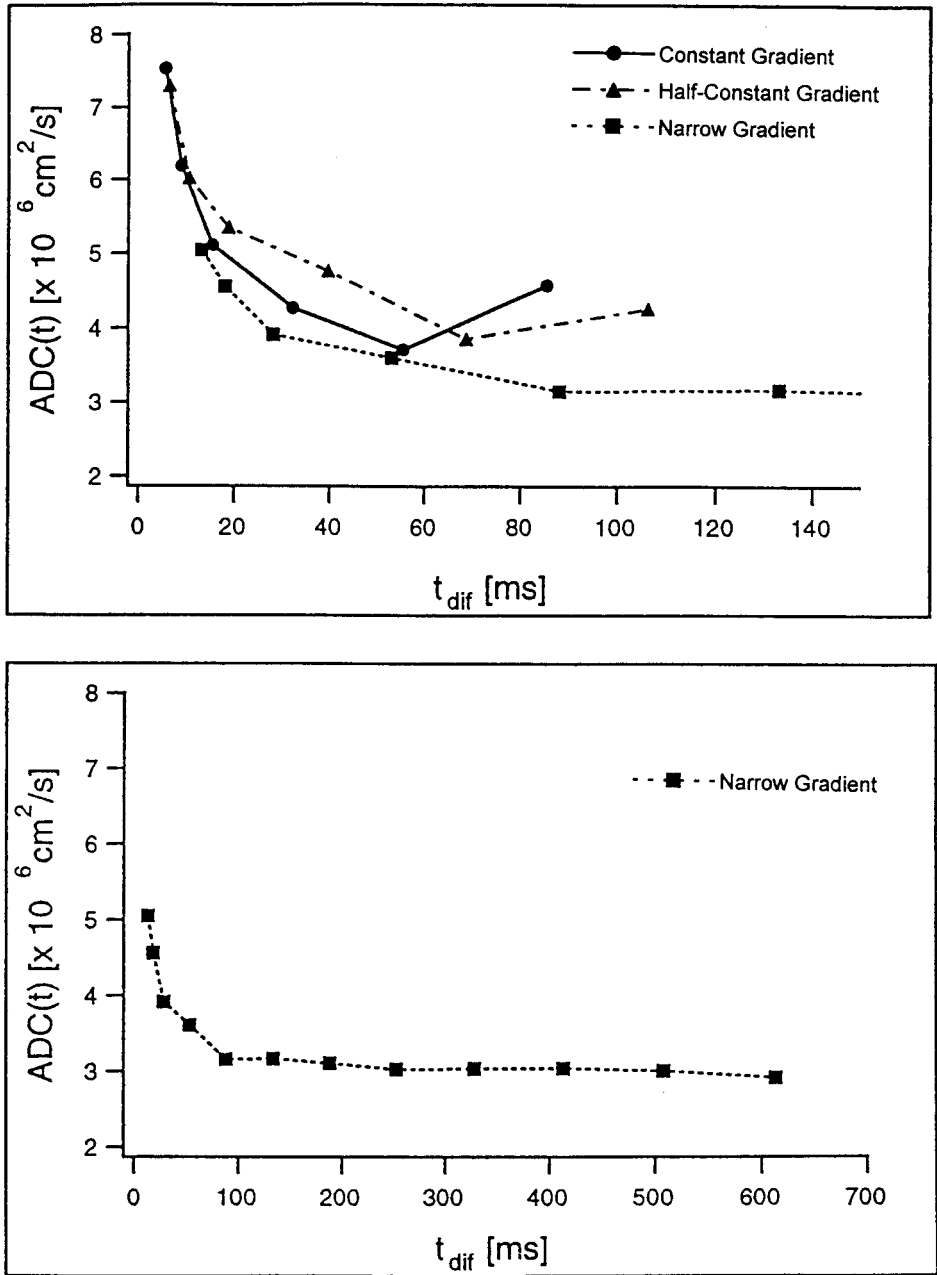


Figure 5.3.1: Measured diffusion coefficients for a RIF-1 tumor with a volume of 1.6 cm^3 . The upper graph shows the diffusion coefficients measured with a constant (●), half-constant (▲) and narrow (■) diffusion gradient over diffusion times ranging from 16 to 133 ms. The lower graph displays the diffusion coefficients measured with a narrow-diffusion gradient (Sequence 4 in Fig. 5.2.2.1) for an extended diffusion time range from 16 to 613 ms.

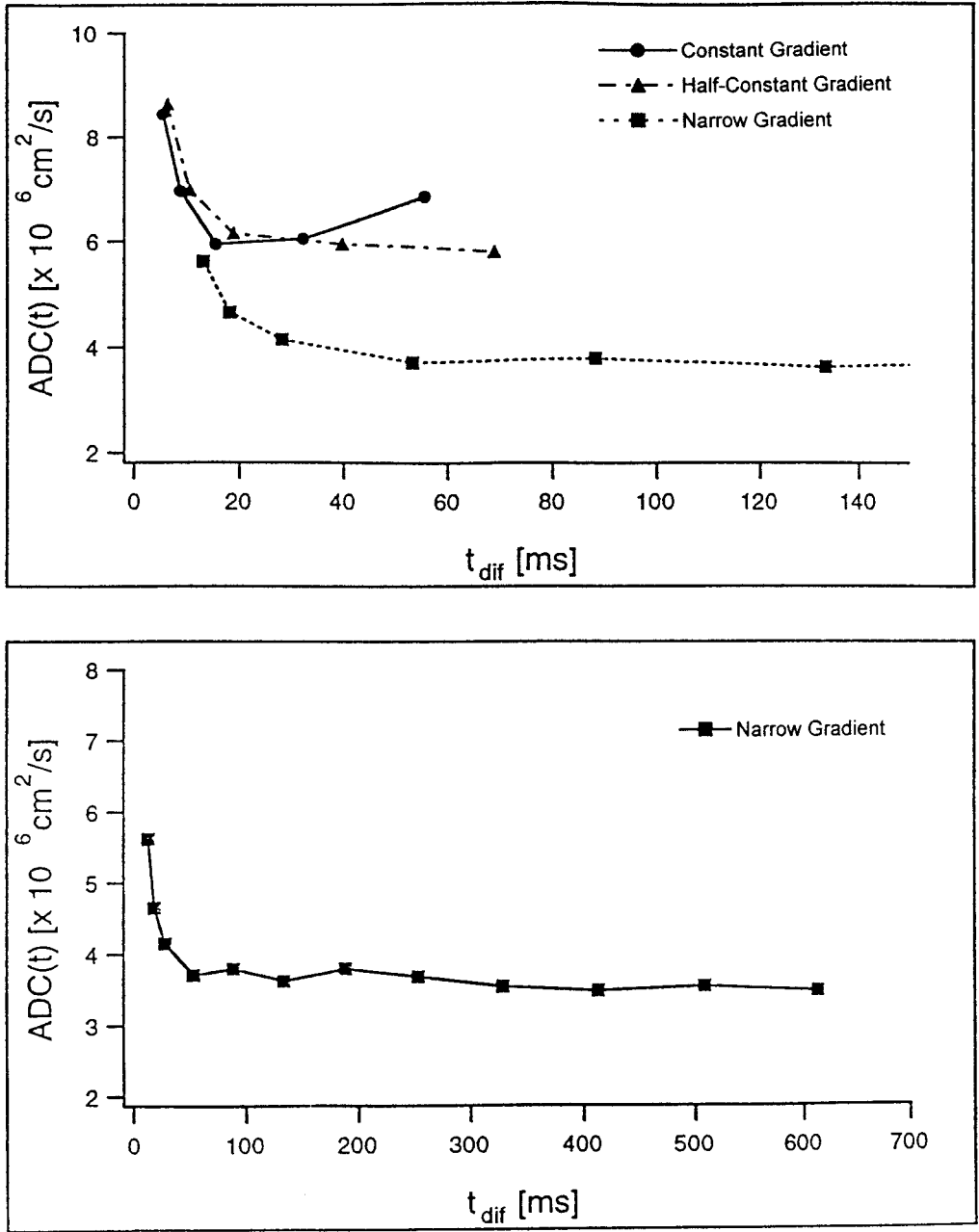


Figure 5.3.2: Measured diffusion coefficients for a RIF-1 tumor with a volume of 2.6 cm^3 . The upper graph shows the diffusion coefficients measured with a constant (\bullet), half-constant (\blacktriangle) and narrow (\blacksquare) diffusion gradient over diffusion times ranging from 16 to 133 ms. The lower graph displays the diffusion coefficients measured with a narrow-diffusion gradient (Sequence 4 in Fig. 5.2.2.1) for an extended diffusion time range from 16 to 613 ms.

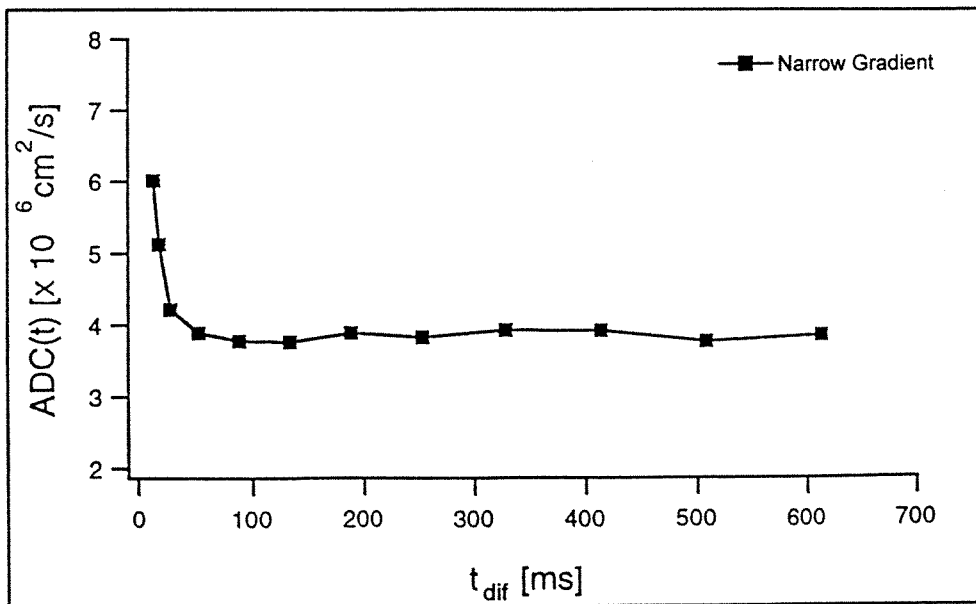
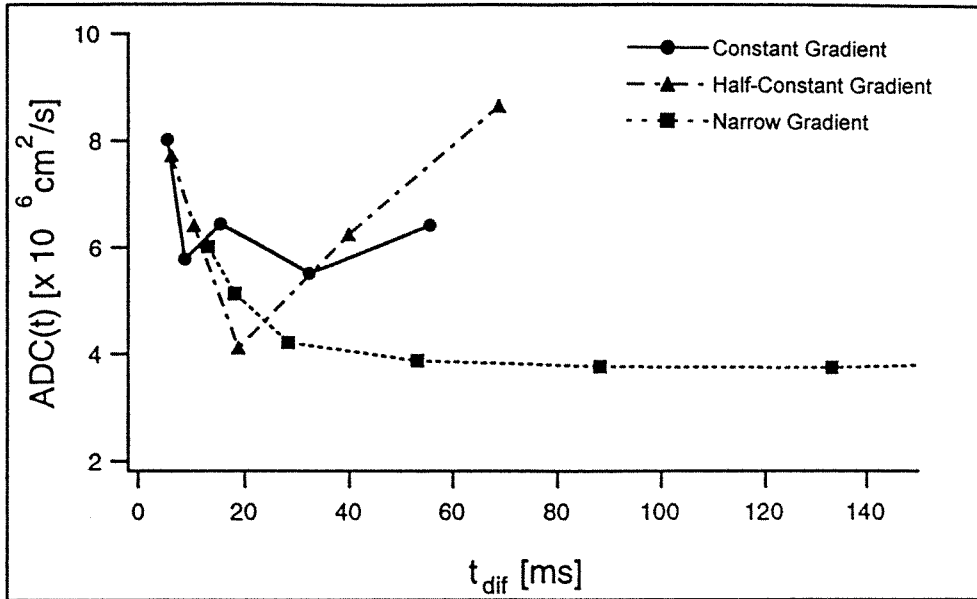


Figure 5.3.3: Measured diffusion coefficients for a RIF-1 tumor with a volume of 3.0 cm³. The upper graph shows the diffusion coefficients measured with a constant (●), half-constant (♦) and narrow (■) diffusion gradient over diffusion times ranging from 16 to 133 ms. The lower graph displays the diffusion coefficients measured with a narrow-diffusion gradient (Sequence 4 in Fig. 5.2.2.1) for an extended diffusion time range from 16 to 613 ms.

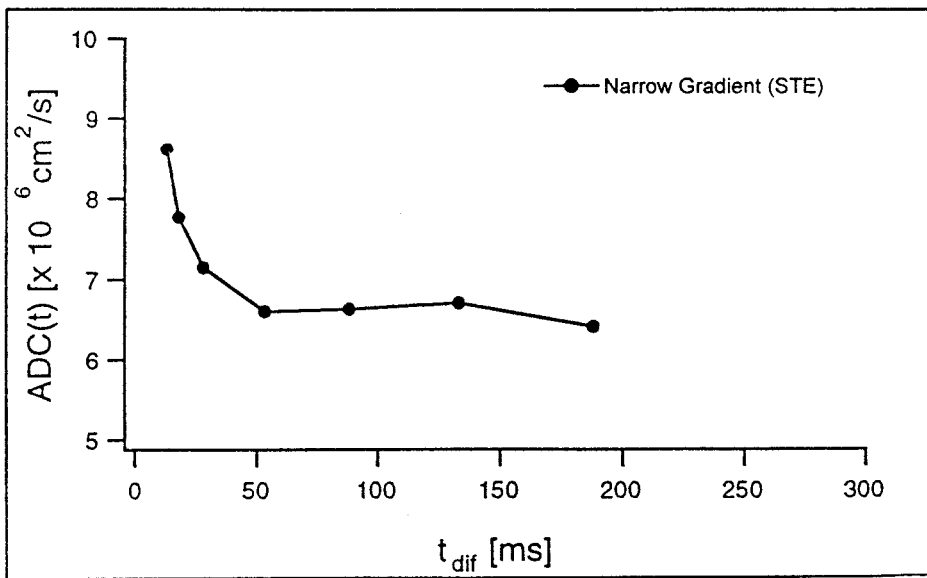
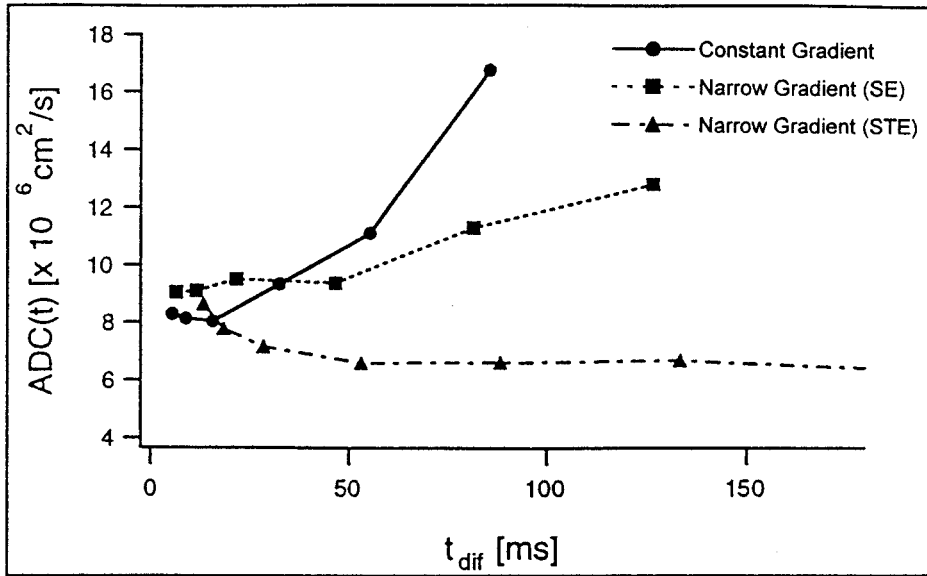


Figure 5.3.4: Measured diffusion coefficients for a RIF-1 tumor with a volume of 0.7 cm^3 . The upper graph shows the diffusion coefficients measured with a constant (●) and narrow (■) gradient spin-echo sequence as well as the diffusion coefficient measured with the modified stimulated-echo sequence (♦) over a diffusion time-range from 16 to 133 ms. The lower graph displays the diffusion coefficients measured with the modified stimulated-echo sequence (Sequence 4 in Fig. 5.2.2.1) for an extended time range.

experiment. The comparison of diffusion coefficients, measured with the narrow diffusion gradient spin-echo and the modified stimulated-echo sequence, demonstrates the effects of increasing T_2 and finite pulse width on the diffusion coefficient. The values of the diffusion coefficients are in agreement only for short diffusion times, but diverge and begin to increase at approximately 20 ms. Diffusion coefficients measured with a constant gradient display a steep increase in ADC with increasing diffusion time. The ADC measured with the narrow diffusion-gradient-spin-echo stays constant up to a diffusion time of 50 ms. Thereafter, the ADC increases with increasing diffusion times, but at a slower rate than the ADC measured by the constant-gradient experiment.

5.4 Discussion and Conclusion

The observed deviation of the diffusion coefficient in the constant and half-constant diffusion-gradient experiment is due to finite pulse width as well as relaxation effects. With increasing diffusion gradient duration, δ , TE also has to increase for these sequences and thus the signal from spins exhibiting short T_2 relaxation times are attenuated. T_2 relaxation times for RIF-1 tumors are approximately 60 ms while the echo-times used in the constant, half-constant and narrow diffusion-gradient spin-echo experiment are up to 120 ms long. For these long echo times, the signal arises preferentially from spins with long T_2 relaxation times as spins with shorter relaxation times experience a significant attenuation before signal acquisition. Since T_2 is inversely proportional to the degree of restrictions in porous media, the signal is expected to arise from spins with the highest diffusion coefficients. The rise of the diffusion coefficient

with increasing diffusion gradient duration and echo time can be clearly observed in the plots of Figs. 5.3.4.1 through 5.3.4.3.

Depending on the diffusion time, the finite pulse width effects may partially temper or enhance the increase of the diffusion coefficient at large values of δ and TE. It has been shown (Mitra and Halperin, 1995a) that diffusion of water molecules during the diffusion-sensitizing gradient can have two different effects. At short diffusion times with short and finite diffusion gradient duration, the effects of restrictions are enhanced and thus decrease the diffusion coefficient. For long diffusion times and long diffusion gradient pulse duration, effects due to restrictions are reduced and the ADC increases as shown in Figs 5.3.1 to 5.3.4. It can be inferred from the data shown in Fig. 5.3.4 that an increase in both the diffusion gradient duration and the echo time leads to an increase of the diffusion coefficient, $D(t)$, with increasing diffusion time.

The diffusion-time dependent measurement of $D(t)$ can be further used to extract important structural information from the sample. It has been shown that the time-dependent diffusion coefficient, $D(t)$, deviates from the bulk fluid value, D_0 , by a term proportional to the surface-area to volume ratio, S/V , (Mitra et al., 1992) as given by

$$\frac{D(t)}{D_0} = 1 - \frac{4}{9\sqrt{\pi}} \frac{S}{V} \sqrt{D_0 t} + O(D_0 t) \quad [5.4.1]$$

for a narrow-diffusion-gradient experiment and has to be modified for a constant-diffusion-gradient experiment (Swiet and Sen, 1994) to:

$$\frac{D(t)}{D_0} = 1 - \frac{32(2\sqrt{2}-1)S}{105\sqrt{\pi}V} \sqrt{D_0 t} + O(D_0 t) \quad [5.4.2]$$

Modification of the numerical prefactor to the surface-area to volume ratio, S/V , is necessary since the entire path of the diffusing molecules must be taken into consideration in addition to the initial and final positions of the molecule. This demonstrates clearly the dependence of the diffusion coefficient, $D(t)$, on the magnitude of the diffusion gradient duration.

The above data demonstrate that both the gradient duration, δ , and the echo time, TE, can have a significant impact on the results of diffusion measurements in biological systems. This is particularly important for diffusion coefficient measurements performed on clinical instruments where limited maximum gradient strength is often compensated for by increasing the diffusion gradient duration. Further complications arise if the measured diffusion coefficient needs to be compared to results obtained at different diffusion times, t , diffusion gradient durations, δ , and echo times, TE.

Chapter 6

Murine Tumor Oxygen Mapping

6.0 Murine Tumor Oxygen Mapping

The goal of this experiment was to develop a non-invasive method for the assessment of the tissue oxygen content during therapeutic intervention in a murine tumor. Hypoxia has long been associated with therapeutic failure, but there is still no clinically available non-invasive method, with good spatial resolution, to monitor tissue oxygenation. My predecessors, Drs. Paul Hees, Bernard Dardzinski and Sam Han have pioneered the development of methods to measure tissue oxygen tension by ^{19}F NMR. Their method was refined to provide a spatial resolution that would be acceptable for clinical use. In this experiment my responsibilities included inoculation of RIF-1 tumors, refinement of the ^{19}F pO_2 measurement, experimental design, data acquisition and processing, as well as data analysis.

6.1 Introduction

Cell hypoxia has long been linked with treatment resistivity and reoccurrence in human cancers (Gray et al., 1953). Tumor hypoxia is caused by the rapid growth rate of the neoplasm accompanied by defective and/or abnormal angiogenesis. The vasculature of tumors consists of blood vessels recruited from the host vasculature and from the vessels growing in response to the rapid tumor cells proliferation (Jain, 1988). The distribution of nutrients and oxygen through the vasculature is governed by the flow rate (Less et al., 1991) and the vascular morphology (geometric arrangement, diameter, length, and number) (Less et al., 1991). Although the underlying mechanism of angiogenesis is

similar in the host and tumor (Patan et al., 1996), they are completely different with respect to organization. The vascular architecture of tumors differs significantly from the host organ and the flow rate of red blood cells is no longer dependent on the vessel diameter but is orders of magnitude lower (Jain, 1996). In normal healthy tissue, cell proliferation is coupled with angiogenic processes to assure an adequate supply of oxygen and nutrients to all cells as well as removal of cellular waste. The rapid cell proliferation in tumors outgrowth the development of the vasculature and is often accompanied by defective angiogenesis. Cells in poorly vascularized and/or inadequately supplied regions of the tumor become oxygen deprived and subsequently hypoxic.

Hypoxia can be categorized as diffusion-limited (chronic) and perfusion-limited (acute) hypoxia. Chronic hypoxia results from the limited distance oxygen can diffuse in tissue (Thomlinson and Gray, 1955; Vaupel, 1977; Olive et al., 1992; Torres-Filho et al., 1994). Acute hypoxia is the result of impaired blood flow and occurs in the vicinity of the vasculature (Brown, 1979; Chaplin et al., 1987; Jain, 1988). The occurrence of hypoxic regions within solid tumors has been confirmed by other researchers (Guichard et al., 1980; Moulder and Rockwell, 1984; Chapman, 1984) and has long been recognized as a determining factor in cancer therapy outcome (Thomlinson and Gray, 1955) and associated with therapeutic failure (Horsman et al., 1988).

Given the relationship between tumor oxygenation and treatment response, many invasive techniques have been proposed to detect, predict (Chapman, 1984) and/or improve tissue oxygenation status (Rockwell, 1985). To date there is still no non-invasive

clinically accepted method available, which provides good spatial resolution, to monitor tissue oxygenation during therapeutic intervention. Oxygen electrodes inserted into the tissue are now small and reliable enough to gain reproducible results but lack the spatial resolution to give a reasonable estimate of the hypoxic cell status and, in some instances, disturb microcirculation patterns. Other methods such as conventional nuclear medicine (Garrecht and Chapman, 1983), photometric (Grunewald and Luebbers, 1976), fluorescent techniques (Olive and Durand, 1983), positron emission tomography (Chapman, 1977) and nuclear magnetic resonance spectroscopy (Ng et al., 1982; Kim and Ackerman, 1988) are either invasive or lack the necessary spatial resolution necessary to monitor dynamic changes.

MRI of administered PFC emulsions can provide anatomical and physiological information and has been used for ^{19}F NMR of blood vessels (Joseph, 1985a; Joseph et al., 1985b; Eidelberg et al., 1988a; Eidelberg et al., 1988b), and tumors (Sotak et al., 1993b; Longmaid et al., 1985; Ratner et al., 1988; Dardzinski et al., 1993b; Dardzinski et al., 1993c). The biodistribution of PFC emulsions has been studied by (McFarland et al., 1985; Ratner et al., 1987; Sotak et al., 1993a; Sotak et al., 1993b; Barker et al., 1993; Dardzinski et al., 1993a). Their radiosensitizing properties (Song, et al., 1985; Rockwell et al., 1986) have long been exploited in the treatment of tumors by radiotherapy.

Ever since the discovery that the spin-lattice relaxation times of perfluorochemicals are highly influenced by the dissolved oxygen concentration, many methods using these compounds have been proposed for the detection of tissue oxygenation and measurement

of partial oxygen pressure (pO_2) within tissue. NMRS was first used establish that perfluorochemicals could be used to detect changes in tumor oxygen status (Mason et al., 1991; Mason et al., 1996; Le et al., 1997). With a growing interest in the spatial distribution of the tissue oxygen status, MRI mapping methods were developed to monitor tumor oxygen status (Mason et al., 1989; Barker et al., 1993; Barker et al., 1994) although these methods suffered J-coupling effects commonly found in compounds with multiple NMR peaks. The introduction of a new perfluorochemical, perfluoro-15-crown-5-ether, with a single resonance and an increased number of fluorine atoms (Sotak et al., 1993c), combined with its biodistribution and sensitivity to oxygen status (Sotak et al., 1993a) allowed a more efficient determination of tissue pO_2 by MRS and echo-planar MRI (Dardzinski and Sotak, 1993a, 1994).

Perfluorocarbons have been used to study tumor vascular patency (Ceckler et al., 1990) and to assess tumor oxygen status in vivo (Thomas et al., 1988; Mason et al., 1991; Dardzinski and Sotak, 1993b). Perfluorocarbon emulsions injected into the vasculature of a mouse will sequester in areas of macrophage activity, such as the reticuloendothelial system, abscesses, and solid neoplasms. The relaxation rate of these compounds is linearly related to the oxygen tension of their environment and can be used as a non-invasive oxygen probe (Mason et al., 1991; Hees and Sotak, 1993; Dardzinski and Sotak, 1993a). In combination with fast imaging techniques such as EPI, MRI of perfluorocarbons can be used to map tumor oxygenation and changes in pO_2 in response to therapy.

The goal of this study was to develop a non-invasive method, based on the linearity relationship between the oxygen tension and the relaxation time of PFC's, to measure the oxygen status of tumors during therapeutic intervention. Characterization of the tumor oxygenation in response to chemotherapy could potentially be used to optimize the timing and effectiveness of therapeutic intervention, thereby improving patient care.

6.2 Experimental Methods

6.2.1 Animal Preparation

All experiments and procedures were approved by the Animal Research Committee (ARC) of the University of Massachusetts Medical School. Animals were housed under diurnal lighting conditions and allowed free access to food and water before and after the experiment. Eight-week-old, female C3H mice (Taconic Farms, Germantown, NJ) were anesthetized by intraperitoneal injection of 60 mg/kg sodium pentobarbital (Abbott Laboratories, Chicago, IL). The right hind leg was shaved and remaining hair removed with a commercial hair remover (NAIR, Carter Wallace Inc., New York, NY).

Radiation induced fibrosarcoma, RIF-1 (Twentyman et al., 1980), cells from a second passage were suspended in Waymouth's medium supplemented with 15% ^{v/v} FBS and 10% ^{v/v} glycerol and stored in liquid nitrogen. Prior to inoculation, the frozen cells were defrosted and 0.15 ml of the suspension containing 1×10^5 cells was subcutaneously

injected into the right hind leg with a 30-gauge hypodermic needle. The tumor volume was monitored daily and determined by measuring the three major orthogonal axes with slide calipers. The volume was calculated to be

$$Volume = \frac{\pi}{6} \times Length \times Width \times Height \quad [5.2.1.1]$$

assuming an ellipsoidal volume (Euhus et. al., 1986; Tomayko and Reynolds, 1989).

For data acquisition, anesthesia was induced with 2% isoflurane delivered in air at 1 l/min and maintained at 1.5% isoflurane at the same flow rate. The body temperature was maintained at 37° C by circulating 34° C warm air through the stereotax, controlled with a T-type temperature probe (Omega, Stanford, CT) and a two-point feedback system.

6.2.2 Experimental Protocol

The experimental protocol is shown in Fig. 6.2.2.1. C3H mice (n=5) with RIF-1 tumors of 0.7 cm³ received an intravenous tail-vein injection of 0.4 ml isotonic perfluoro-15-crown-5-ether (40% v/v) emulsion. Thereafter, the PFC was given 48 hours to clear from the vasculature before imaging. Imaging was then performed for three consecutive days. Following the first day of imaging, the animals received an intraperitoneal injection of 100 mg/kg 5-Fluorouracil (5-FU) (Sigma Chemicals, St. Louis, MO) dissolved in sterile

physiologic (0.9 %) saline (Baxter, Deerfield, IL). Two days after the first three consecutive days of MRI, the animal was reinjected with 0.4 ml of the isotonic perfluoro-15-crown-5-ether (40% v/v) emulsion. At this point, the tumor volume is at a minimum, as determined by inspection of RIF-1 tumor growth curves in Fig. 4.1.4.1, and significant amounts of the PFC injection had cleared from the tumor. A 48-hour time period was given to allow the second PFC injection to clear from the vasculature before the tumor was again imaged for three consecutive days.

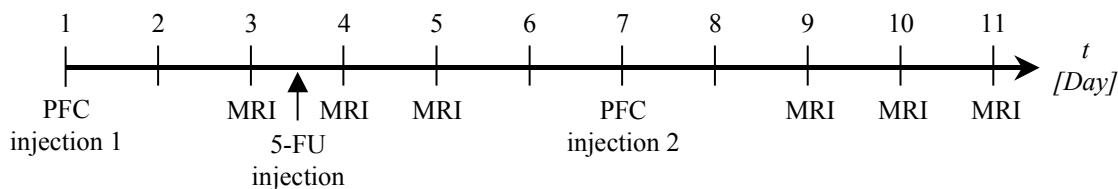


Figure 6.2.2.1: Experimental protocol for pO_2 monitoring of RIF-1 tumors in C3H mice treated with 5-Fluorouracil (5-FU). Animals with a tumor volume of 0.7 cm^3 received 0.4 ml of isotonic perfluoro-15-crown-5-ether (40 % v/v) emulsion via tail-vein injection. A 48 hour time period was given to allow the PFC from the first injection to clear from the vasculature. The animal was then imaged for three consecutive days. After the first imaging session animals received an i.p. injection of 100 mg/kg 5-FU. Two days after the first three days of imaging the animal received a second injection of 0.4 ml of perfluoro-15-crown-5-ether emulsion. The PFC of the second injection was allowed to clear from the vasculature for two days before the animal was imaged again for three consecutive days.

6.2.3 NMR Measurements

Imaging data were acquired using a horizontal bore GE CSI-II 2.0 T 45-cm imaging spectrometer (GE NMR Instruments, Fremont, CA), operating at 80.49 MHz for ^{19}F and

85.56 MHz for ^1H , equipped with ± 20 G/cm self-shielded gradients and a four-turn solenoidal RF-coil with 18-mm inner diameter.

Multiple-slice, inversion-recovery echo-planar imaging was used to acquire 1-mm-thick slices over the entire tumor volume. The eight coronal images for each slice were acquired with an inversion times (TI) of 0.01, 0.08, 0.2, 0.5, 1.0, 3.0, 5.0 and 8.0 seconds, respectively, a repetition time (TR) of 10 s, an echo time (TE) of 74 ms, a spectral width (SW) of ± 30000 Hz, four signal averages (NEX), a field of view (FOV) of 30.0×30.0 mm, and 64×64 digital resolution. ^1H images of each slice were obtained using the same acquisition parameters except for TR = 6s, and were used as segmentation images during the calculation of the $p\text{O}_2$ maps.

6.2.4 Data Analysis

In vitro T_1 relaxation curves for calibration were acquired spectroscopically from the net perfluoro-15-crown-5-ether at four different temperatures, 22, 27, 32, and 37° C, and O_2 concentrations of 5, 21, 35, and 50%, to establish the relationship between the relaxation time and the oxygen content. Calibrated O_2/N_2 gas mixtures of 5, 21, 35, and 50% O_2 were separately bubbled through the PFC for 30 minutes before the T_1 value was measured spectroscopically at each temperature. Calibration curves of the partial oxygen tension, $p\text{O}_2$, in torr as a function of temperature, T , and the relaxivity, R_1 ($1/T_1$), were obtained by fitting the data using multiple-linear regression.

Oxygen tension maps were created from a series of ^{19}F IR-EPI's, which were fitted, on a pixel-by-pixel basis, using a nonlinear-least-squares Levenberg-Marquardt algorithm to the equation

$$S(TI) = A \left(1 - B e^{-\frac{TI}{T_1}} \right) \quad [6.2.4.1]$$

where TI is the inversion time, A the signal intensity for $TI = 0$, B the inversion efficiency and T_1 the relaxation time. Each pO_2 map was masked using the ^1H images to avoid fitting pixels that did not originate from within the tumor. Oxygen tension maps were then created from the calculated T_1 maps using the calibration equation derived from the *in vitro* T_1 measurement. Tumor T_1 values smaller than 1 s and larger than 3 s were disregarded as a result of a poor fit and because they were out of the range of possible T_1 values achievable with perfluoro-15-crown-5-ether under physiological conditions.

Histograms of relative frequency versus pO_2 concentration, with a bin size of ten torr, were generated from each slice at each day. The mean pO_2 of each histogram was calculated and bar graphs displaying the mean of each slice for each individual day were created. Further, the mean pO_2 of the entire tumor was calculated at each day and plotted as a function of time.

6.3 Results

Multiple regression was used to extract the relationship between the partial oxygen tension, pO_2 , the temperature, T , and the *in vitro* measured relaxation time, $T_1 = 1/R_1$, from measurements at four oxygen concentrations and four different temperatures. The resulting calibration equation was

$$R_1 = 0.6897 + 0.0038pO_2 - 0.0098T \quad [r^2 = 0.997] \quad [6.3.1]$$

where the partial oxygen tension, pO_2 , is in torr, and the temperature, T , is in degrees Celsius. Rearranging Eq. [6.3.1] for pO_2 gives:

$$pO_2 = 264.502R_1 + 2.5799T - 182.424 \quad [6.3.2]$$

Equation [6.3.2] was then used to convert the measured ^{19}F relaxation rates, R_1 ($1/T_1$) into the partial oxygen tension at a given temperature of 37° C.

Figure 6.3.1 shows a calculated pO_2 map and a corresponding raw image at the inversion time, TI , of eight seconds. The map was filtered, as described in the methods section, and disregarded pixels due to a poor fit or physiologically unreasonable values were set to 253. Pixels with low signal-to-noise resulted in poor fits and hence erroneous relaxation times. Pixels at the noise level in the raw image corresponded well with the pixels (set to

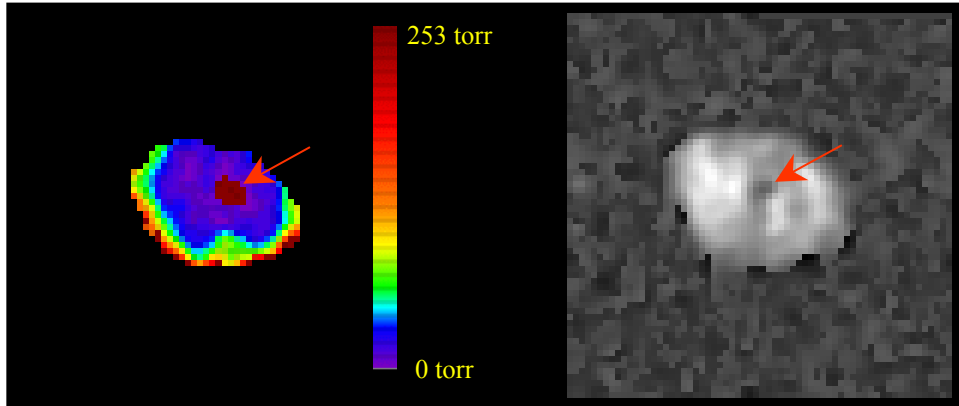


Figure 6.3.1: Calculated pO_2 map of a slice through RIF-1 tumor (left) and a ^{19}F IR-EPI (with $TI = 8$ s) of the same slice (right). Pixels with poor fit, marked by the red arrow, were set to a value of 253. The area of poor fitting can be seen in the ^{19}F IR-EPI as a region with low signal-to-noise and corresponds to the pixels with a value of 253 in the pO_2 map.

253) in the pO_2 maps as indicated by the red arrow in Fig. 6.3.1. Figure 6.3.2 illustrates the signal intensity versus TI for a pixel in Fig. 6.3.1 that was disregarded.

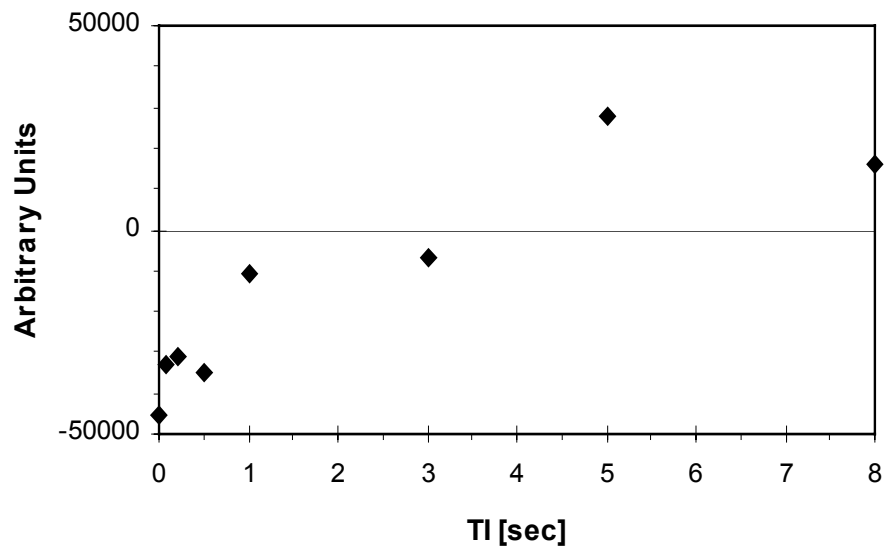


Figure 6.3.2: Plot of the signal intensity versus TI for a pixel from Fig. 6.3.1 that was disregarded.

The plot in Fig. 6.3.3 shows the signal intensity for a pixel of the same image but with a good fit. It can be seen that the signal magnitude for this pixel is larger than the signal magnitude of the poor-signal pixel and that the signal intensity follows Eq. [6.2.3].

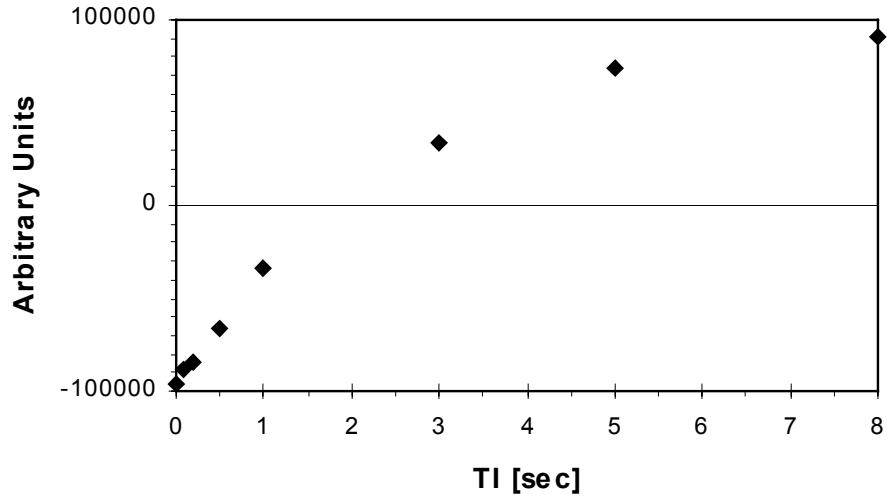


Figure 6.3.3: Plot of the signal intensity versus inversion time, TI , for a pixel from Fig. 6.3.1 which resulted in a good fit to Eq. [6.2.4.1].

The resulting pO_2 maps of a representative tumor for each imaging day and slice are displayed in Fig. 6.3.4. Slice 1, representing the bottom of the tumor, is the first slice and is located at the height of the underlying muscle. The adjacent slices are then taken towards the top of the tumor, away from the muscle. The maps demonstrate clearly the difference in oxygen tension between slices and over the entire tumor volume. A reduction in tumor oxygenation can be seen as the tumor volume decreases following the administration of chemotherapy and then at later time, when the tumor volume again starts to increase.

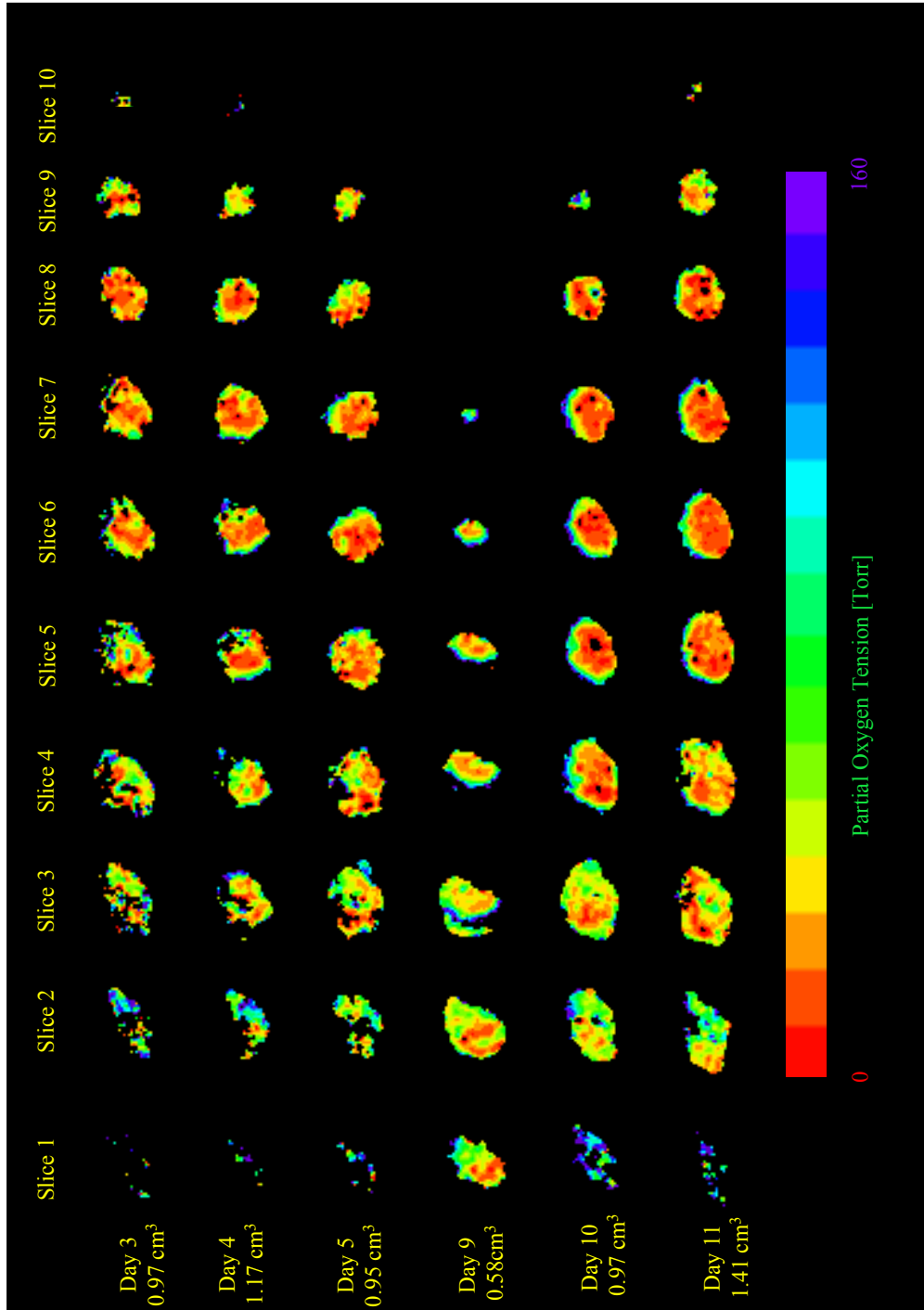


Figure 6.3.4: Oxygen tension maps of a representative RIF-1 tumor grown on the right hind leg of a C3H mouse. The maps were acquired by multiple-slice ^{19}F MRI, with a thickness of 1 mm, over the time course of chemotherapeutic intervention. Slice 1, representing the bottom of the tumor, is the first slice and is located at the height of the underlying muscle. The adjacent slices are taken towards the top of the tumor. Following the first day of MRI (Day 3), the animal received a single bolus injection of 100 mg/kg 5-Fluorouracil intraperitoneally. At Day 7, when the tumor volume was at the minimum, the animal received a second injection of 0.4 ml perfluoro-15-crown-5-ether. The pO_2 maps illustrate the dynamic changes in tumor oxygenation between consecutive days and for adjacent slices over the time course of chemotherapeutic treatment.

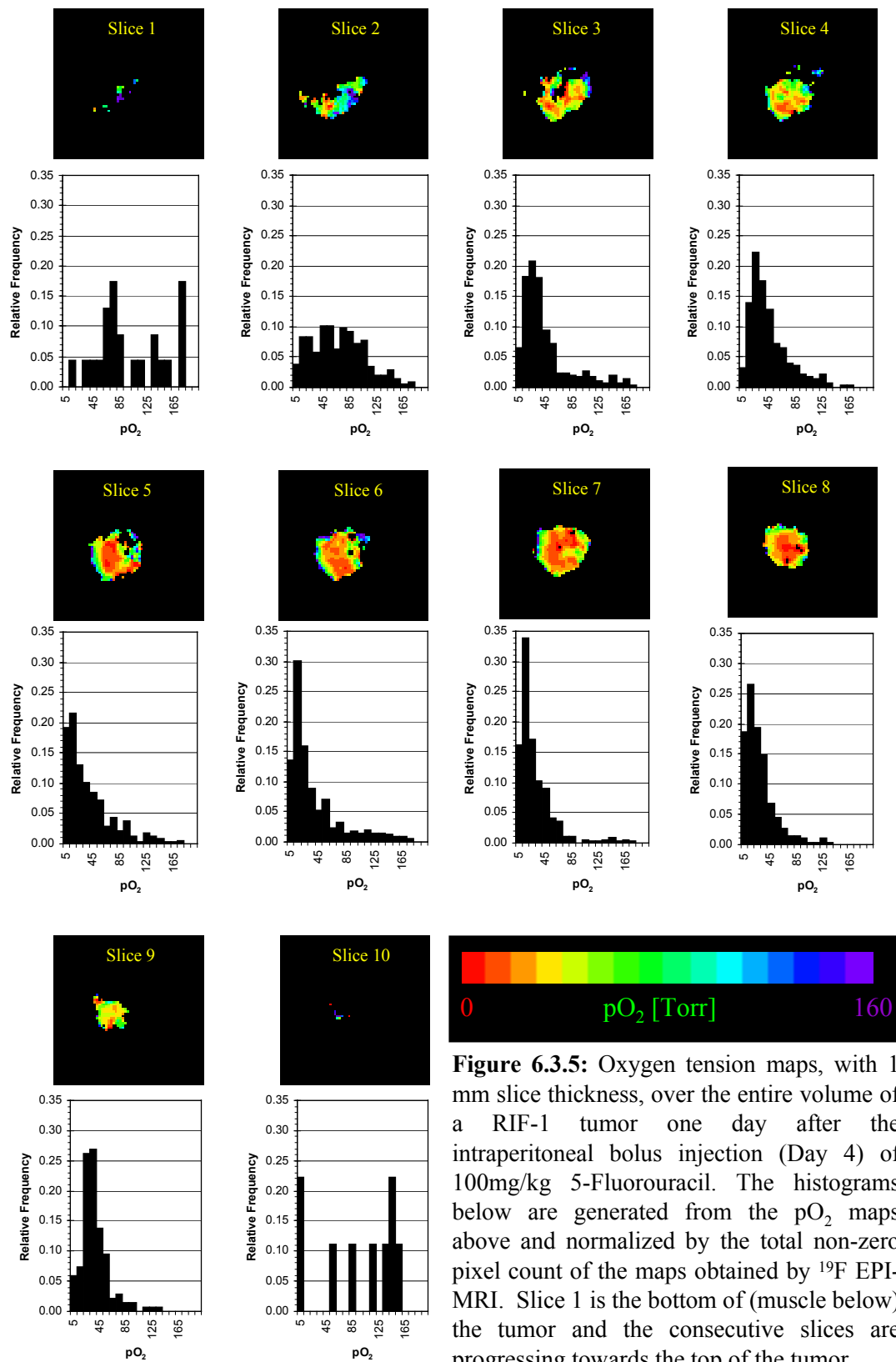


Figure 6.3.5: Oxygen tension maps, with 1 mm slice thickness, over the entire volume of a RIF-1 tumor one day after the intraperitoneal bolus injection (Day 4) of 100mg/kg 5-Fluorouracil. The histograms below are generated from the pO_2 maps above and normalized by the total non-zero pixel count of the maps obtained by ^{19}F EPI-MRI. Slice 1 is the bottom of (muscle below) the tumor and the consecutive slices are progressing towards the top of the tumor.

To further visualize the differences in pO_2 within an individual slice, a histogram of each slice was generated from the respective pO_2 maps. In Fig. 6.3.5, the pO_2 maps and the corresponding histograms are displayed for Day 4. Both the maps and the histograms show that the pO_2 concentration in the tumor varies significantly with spatial location.

During the time course of the chemotherapeutic intervention, clear changes in the oxygenation status of the tumor are observed. These changes are displayed in Fig. 6.3.6, where the mean pO_2 over the course of the treatment is plotted for each slice and day. Slices at the bottom (e.g. Slice 1) and top of the tumor consistently display a higher mean pO_2 than slices within the tumor.

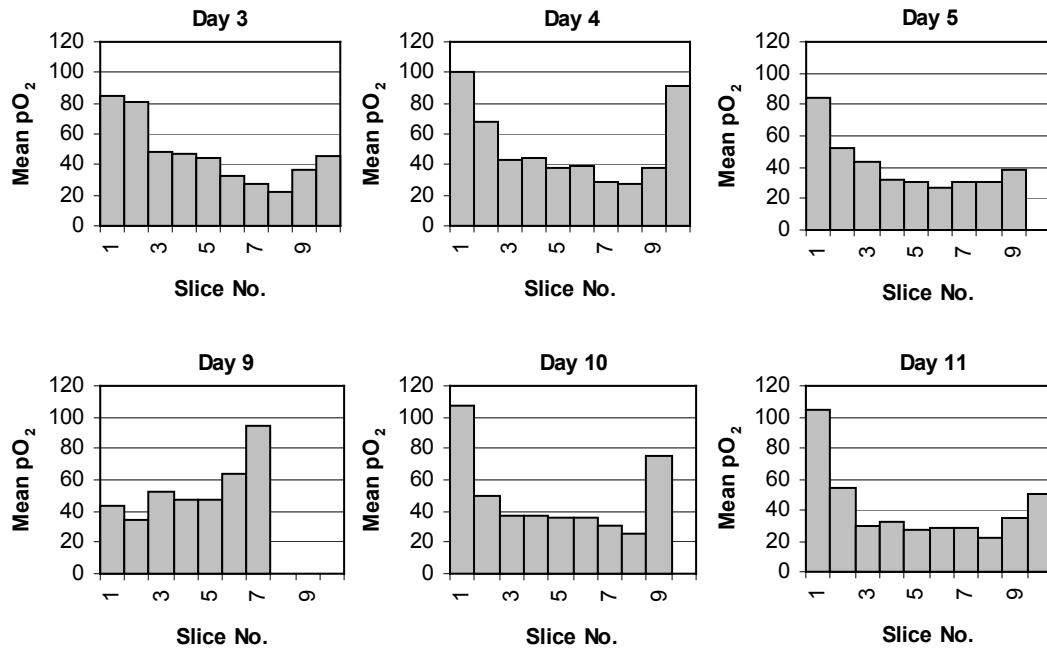


Figure 6.3.6: Mean pO_2 of each slice and each imaging day calculated from the histograms of the maps shown in Fig. 6.3.4.

Comparison of the mean pO_2 of the entire tumor calculated from all slices of that day allowed visualization of the effect of treatment on the pO_2 over the time course of therapeutic intervention. The mean pO_2 at Day 3 was measured before the injection of the chemotherapeutic agent. Over the subsequent days (Day 4 and Day 5), the mean pO_2 of the tumor decreases. As the tumor volume starts to increase again (Day 9 and Day 10) following therapy, the pO_2 increases slightly. As the tumor volume gets larger (Day 11), increases in hypoxic tissue further reduce the tumor oxygen tension. This general tendency was observed in all tumors studied and a plot for a representative animal is shown in Fig. 6.3.7.

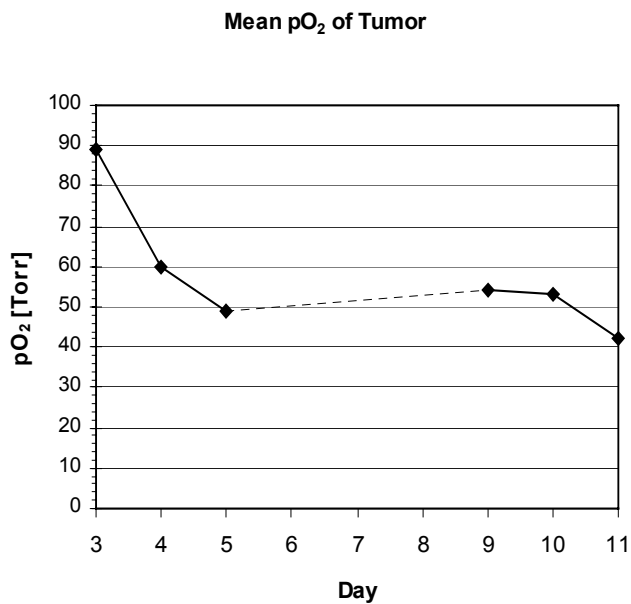


Figure 6.3.7: Plot of the mean pO_2 of the entire tumor versus time (Days) from a representative animal, calculated from all slices of the respective day. The dashed line marks the time when the PFC was reinjected and allowed to clear from the vasculature.

6.4 Discussion & Conclusion

Examination of the pO_2 maps demonstrates the changes of oxygen tension within the tumor and the necessity for good spatial resolution for the assessment of the tissue oxygen status. Even between adjacent slices there are large differences in oxygen tension (Fig. 6.3.5). Examination of Fig. 6.3.5 clearly illustrates the changes in pO_2 between adjacent 1-mm-thick slices. The plot of the mean pO_2 for each slice at Day 4 (Fig. 6.3.6) illustrates these changes. Slices at the bottom and top of the tumor have consistently higher pO_2 values than the tumor core, which can be explained by the vascular growth pattern. Tumor vasculature in solid tumors has its highest density at the periphery and a decrease in density towards the core of the tumor. These regions of high pO_2 can also be seen in Fig. 6.3.4. Areas well supplied with oxygen are mainly found at the periphery of the tumor. The bottom of the tumor is generally not well supplied with oxygen. In the case of RIF-1 tumors grown on the hind leg of a mouse, this area gains its oxygen supply from the well oxygenated muscle tissue adjacent to the tumor.

Looking at the entire tumor volume during chemotherapy allows a complete assessment of changes in tissue oxygenation in response to chemotherapy. As the tumor volume decreases as a result of chemotherapy, so does the tissue pO_2 . All tumors showed the expected decrease in mean pO_2 after the administration of the chemotherapeutic drug. This decrease is due to the toxic affect of the agent that causes tumor cell death. Dying and dead tumors cells, that have not been removed, have an extreme low oxygen tension and are still visible in the maps. The contribution of these cells results in an decrease in tissue oxygen tension that is observable in Figs. 6.3.4, 6.3.6 and 6.3.7. Dead cell material

is then removed by auto- and/or heterolysis resulting in a decrease in tumor volume. The decrease in pO_2 continues until tumor regrowth regains a dominant role following treatment. At this time, the relatively small tumor is well supplied with oxygen since most of the cells are within the vicinity of the vasculature. This close proximity to the vasculature in turn results in an increased oxygen supply and tissue oxygen status. Imaging on Day 9 captures the end of the regrowth phase, where the tumor is still relatively well supplied with oxygen. The resulting high mean pO_2 for this day can be seen in both the pO_2 maps as well as in the plot of the mean pO_2 versus time (Fig. 6.3.7).

Data from the regrowth phase were not available due to the clearance of the sequestered PFC from the tumor. Reduction of the tumor volume by auto- and/or heterolysis in response to chemotherapeutic intervention causes not only the removal of dead cell material but also the partial removal of the PFC emulsion particles. In order to gain sufficiently high S/N for the ^{19}F EPI, a second injection of the perfluoro-15-crown-5-ether was necessary. The preferred time point of this injection was chosen as the time at which the tumor had reached its smallest volume. Reinjection at this time point was thought to minimize the removal of the PFC from the tumor by the chemotherapeutic process. Following the second injection, there was a 48-hour period during which the PFC was allowed to clear from the vasculature. Imaging of the tumor during this period is thought to result in biased of the measured pO_2 by the vascular oxygen concentration.

On Days 10 and 11, a decrease in pO_2 can be observed as the rapid cell proliferation causes the tumor to again outgrow its vasculature supply. The rapidly-growing tumor is

not supported by a corresponding growth of the vasculature, leaving many cells within the tumor without adequate oxygen. While all the tumors studied displayed similar behavior and oxygenation pattern in response to chemotherapy, it was not possible to qualitatively pool the results from all tumors due to inter-tumor variability. Since each tumor displays its own growth pattern, which is dependent on the nutritional supply to the neoplasm and the host vasculature, each tumor can only be compared to the oxygen status before the initiation of therapy. Another factor is inter-animal differences in the rate at which the chemotherapeutic agent (5-FU) is metabolized for activation. Varying metabolic rates between animals leads to different levels of activated 5-FU and hence to differences in the growth pattern during chemotherapy. Consequently, the best basis for comparison is the pO_2 distribution and the mean pO_2 before treatment. Comparison of the pre-treatment pO_2 maps (Day 3) with the pO_2 maps after treatment clearly shows the induced changes in tissue oxygen status and the decrease in pO_2 . A subsequent increase in pO_2 , due to the rapid cell proliferation following treatment, eventually results in a significant amount of hypoxia.

This study demonstrated that ^{19}F MRI can assess tumor oxygen status non-invasively with a sufficiently spatial resolution to detect dynamic changes in tissue oxygen status in response to chemotherapy. Examination of the pO_2 maps and histograms demonstrate the need for the spatial resolution provided by ^{19}F EPI to monitor oxygen tension in tumors. The large variability of pO_2 between the slices through the tumor, as well as the changes occurring over the time course of treatment, are difficult to capture using modalities with coarser spatial resolution (e.g., oxygen electrodes). Other methods, such as nuclear

medicine and positron emission tomography, which might be able to reproduce the same resolution, are invasive and cannot be used to monitor the time course over an extended time period. Multiple slice ^{19}F IR-EPI should be a powerful tool for the non-invasive assessment of tumor oxygen status and for the guidance of chemo- or radiation therapy.

Chapter 7

Summary

Summary

The first study involved the transfer of the porous media theory to biological systems. Structural properties provide the connecting bridge between the two systems. The porous media theory has its origin in the investigation of pore space in rocks and sediments. In such systems there are interconnected or enclosed pore spaces surrounded by solid matter. Measurements of the diffusion coefficient allow the geometry of this space to be probed and the extraction of the surface-area to volume ratio as well as the tortuosity. While the surface-area to volume ratio provides information of the structural geometry, the tortuosity provides information regarding the connectivity of the pore space. In biological tissue there are similar structures. Although the restricting barriers are not impenetrable as in the case of porous media, water molecules in biological tissue still experience similar restrictions from the cell membranes and organelles. Nevertheless, the tortuosity in biological systems must be redefined and combined with the connectivity of the cell space and the permeability of the cell membranes since diffusing water molecules can cross cell boundaries. The application of porous media theory to biological systems was already shown by Dr. Latour during his stay at WPI. New in the present research is the use of the return-to-the-origin (RTO) probability, which is based on the porous media theory.

Application of the RTO probability to measure structural changes as they occur in response to tissue necrosis was the first project. Chapter 3 shows that the RTO-enhancement, R , decreases with increasing tumor size. Therefore, R , should be inversely correlated to an increasing amount of necrosis, since tumors become increasingly necrotic

as they grow larger. The findings of the first study were presented at the 5th Scientific Meeting of the International Society of Magnetic Resonance in Medicine in Vancouver. The next phase of the project was to extend the spectroscopy experiments to imaging. Measuring diffusion with high gradients resulted in two major problems: The increase in echo time necessary to accommodate the image acquisition and the reduced signal due to smaller volume. The development of the RTO imaging method was a compromise between the need for high k values and a good signal-to-noise ratio. The first attempts were very encouraging and presented at the IEEE 24th Northeastern Biomedical Engineering Conference in Hershey, Pennsylvania. Comparison with the histological sections in a follow-up study showed that in spite of the good preliminary results, the ADC and RTO-enhancement maps showed only general agreement in their major features. This is most likely a result of the large slice thickness as compared to previous studies. A thinner slice thickness would result in better agreement but needs to be demonstrated and addressed in a future study. The mean of both the ADC and the RTO-enhancement maps agreed well with the necrotic tissue fraction determined by histology.

The chemotherapy study involved the characterization of RIF-1 tumors in response to administration of 5-Fluorouracil. Tumor growth curves were acquired for characterization of the response to different doses of the drug. The purpose of the study was to determine if the ADC and the RTO probability were sensitive enough to detect early changes in tumor tissue structure in response to therapeutic intervention. This could provide a useful tool in the guidance of therapy and avoid prolonged exposure to chemotherapeutic agents if the neoplasm is not responding well to treatment.

The study of the influence of finite pulse width on the measured diffusion coefficient tried to answer some of the problems arising when limited gradient strength is compensated for by increasing the gradient duration. As diffusion measurements on clinical MRI scanner become more prevalent, many of the instruments will not have the required gradient strength for diffusion measurements using short pulse widths. Instead, the signal attenuation achieved by increasing the gradient duration is closer to a constant gradient experiment diffusion experiment, which makes the results of such experiments more difficult to interpret. Even though the differences in the measured diffusion coefficient, $D(t)$, could be demonstrated in this study, future studies will have to be conducted to find quantitative and mathematical expressions to account for deviations from classical NMR diffusion theory.

The last experiment in this series was the mapping of tissue oxygen tension in response to chemotherapy. Previous studies required a large slice thickness to compensate for the small fluorine signal arising from the injected PFC. Optimization of the complete process, from the PFC injection to improvements in the data acquisition methodology, allowed us to reduce the slice thickness to 1 mm. In the original incarnation of this study, a single slice with a thickness of 3 mm was used. After a conversation with Dr. Fitzgerald, who pointed out the significance to assess the oxygen status at a higher resolution, and the acceptable signal levels obtained at 1 mm slice thickness, the protocol was reevaluated. Oxygen maps acquired in the study illustrate the changes in tissue oxygen tension in response to therapeutic intervention. The results should demonstrate that ^{19}F MRI of PFC's in tumors is a powerful tool for non-invasive monitoring of cancer

therapy. Future studies need to further refine the use of ^{19}F MRI and its application in the support of cancer therapy.

Bibliography

Bibliography

Abragam A, The Principles of Nuclear Magnetism, 2nd ed. London, Oxford University Press, 1992.

Aiken NR, McGovern KA, Ng CE, Wehrle JP, Glickson JD, ^{31}P NMR Spectroscopic Studies of the Effects of Cyclophosphamide on Perfused RIF-1 Tumor Cells, *Magn. Reson. Med.*, **31**, 241-247, 1994.

Barker BR, Mason RP, Peshock RM, Echo Planar Imaging of Perfluorocarbons, *Magn. Reson. Imag.*, **11**, 1165-1173, 1993.

Barker BR, Mason RP, Bansal N, Peshock RM, Oxygen Tension Mapping with F-19 Echo-Planar MR Imaging of Sequestered Perfluorocarbon, *J. Magn. Reson. Imag.*, **4**, 595-601, 1994.

Barrer RM, Diffusion in Polymers, (Edited by Crank J, Park GS), p. 165, Academic Press, London, 1968.

Bear J, Dynamics of Fluids in Porous Media, pp106ff, Dover, 1988.

Berg HC, Random Walks in Biology, Expanded edition, Princeton, Princeton University Press, 1993.

Blees MH, The Effect of Finite Duration of Gradient Pulses on the Pulsed-Field-Gradient NMR Method for Studying Restricted Diffusion, *J. Magn. Reson. Ser. A*, **109**, 203-209, 1994.

Bloch F, Hansen WW, Packard M, Nuclear Induction, *Phys. Rev.*, **69**, 127, 1946.

Bloch F, Hansen WW, Packard M, Nuclear Induction Experiment, *Phys. Rev.*, **70**, 474-485, 1946.

Bloch F, Nuclear Induction, *Phys. Rev.*, **70**, 461-474, 1946.

Brown JM, Evidence of Acutely Hypoxic Cells in Mouse Tumors and a Possible Mechanism of Reoxygenation, *Br. J. Radiol.*, **52**, 650-656, 1972.

Callaghan PT, Principles of Nuclear Magnetic Resonance Microscopy, Oxford University Press, New York, NY, 405-406, 1991.

Callaghan PT, Coy A, MacGowan D, Packer KJ, Zelayo FO, Diffraction-Like Effects in NMR Diffusion Studies of Fluids in Porous Solids, *Nature*, **351**, 467-469, 1991.

Callaghan PT, Coy A, Halperin TPJ, MacGowan D, Packer KJ, Zelayo FO, Diffusion in Porous Systems and the Influence of Pore Morphology in Pulsed Gradient Spin-Echo Nuclear Magnetic Resonance Studies, *J. Chem. Phys.*, **97**, 651-662, 1992.

Callaghan PT, Coy A, Forde LC, Rofe CJ, Diffusion Relaxation and Edge Enhancement in NMR Microscopy, *J. Magn. Reson. Ser. A*, **101**, 347-350, 1993.

Carr HY, Purcell EM, Effects of Diffusion on Free Precession in Nuclear Magnetic Resonance Experiments, *Phys. Rev.*, **94**, 630-638, 1954.

Ceckler TL, Gibson SL, Hilf R, Brynat RG, *In Situ* Assessment of Tumor Vascularity Using Fluorine NMR Imaging, *Magn. Reson. Med.*, **13**, 133-146, 1990.

Chaplin DJ, Olive PL, Durand RE, Intermittent Blood Flow in Murine Tumor: Radiobiological Effects, *Cancer Res.*, **47**, 597-601, 1987.

Chapman JD, Urtasin RC, The Application in Radiation Therapy of Substances which Modify Cellular Radiation Response, *Cancer*, **40**, 484-488, 1977.

Chapman JD, The Detection and Measurement of Hypoxic Cells in Solid Tumors, *Cancer*, **54**, 2441-2449, 1984.

Crank J, The Mathematics of Diffusion, 2nd ed., Oxford University Press, Oxford, 1975.

Crick F, Diffusion in Embryogenesis, *Nature*, **225**, 420-422, 1970.

Dardzinski BJ, Sotak CH, *In Vivo* Oxygenation Mapping with Inversion-Recovery Echo-Planar Imaging and ^{19}F Relaxometry of Perfluorocarbon Emulsion, *J. Magn. Reson. Imag.*, **3(P)**, 157-158, 1993a.

Dardzinski BJ, Sotak CH, *In Vivo* Tumor Oxygenation Mapping Using Inversion-Recovery Echo-Planar Imaging and ^{19}F Relaxometry of Perfluorocarbon Emulsions, *Proc. 12th SMRM 12th Annual Meeting*, New York, NY, p. 405, 1993b.

Dardzinski BJ, Sotak CH, Evaluating Changes in Murine Tumor Oxygenation in Response to Nicotinamide by Using F-19 Echo-Planar Imaging and Spectroscopy, *J. Magn. Reson. Imag.*, **4(P)**, 55, 1994.

Demsar F, Roberts TPL, Schwickert HC, Shames DM, van Dijke CF, Mann JS, Saeed M, Brasch RC, A MRI Spatial Mapping Technique for Microvascular Permeability and Tissue Blood Volume Based on Macromolecular Contrast Agent Distribution, *Magn. Reson. Med.*, **37**, 236-242, 1996.

Eidelberg D, Johnson G, Barnes D, Tofts PS, Delphy D, Plummer D, McDonald WI, ¹⁹F NMR Imaging of Blood Oxygenation in the Brain, *Magn. Reson. Med.*, **6**, 344-352, 1988a.

Eidelberg D, Johnson D, Tofts PS, Dobbin J, Crockard HA, Plummer D, ¹⁹F Imaging of Cerebral Blood Oxygenation in Experimental Middle Cerebral Artery Occlusion: Preliminary Results, *J. Cereb. Blood Flow Metab.*, **8**, 276-281, 1988b.

Fiennes AGTW, Growth Rate of Human Tumor Xenografts Measured in Nude Mice by *In Vivo* Cast Modelling, *Br. J. Surg.*, **75**, 23-24, 1988.

Euhus DM, Hudd C, LaRegina MC, Johnson FE, Tumor Measurements in the Nude Mouse, *J. Surg. Oncol.*, **31**, 229-234, 1986.

Gallez B, Bacic G, Goda F, Jiang J, O'Hara JA, Dunn JF, Swartz HM, Use of Nitroxides for Assessing Perfusion, Oxygenation and Viability of Tissue: *In Vivo* EPR and MRI Studies, *Magn. Reson. Med.*, **35**, 97-106, 1996.

Garrecht BM, Chapman JD, The Labeling of EMT-6 Tumors in BALB/c Mice with ¹⁴C-Misonidazole, *Br. J. Radiol.*, **56**, 745-753, 1983.

Gray LH, Conger AD, Ebert M, Hornsey S, Scott OCA, Concentration of Oxygen Dissolved in Tissue at Time of Irradiation as a Factor in Radiotherapy, *Br. J. Radiol.*, **26**, 638-648, 1953.

Grunewald WA, Luebbers DW, Cryophotometry as a Method for Analyzing the Intracapillary HbO₂ Saturation of Organs under Different O₂ Supply Conditions, *Adv. Exp. Med. Biol.*, **75**, 55-64, 1976.

Guichard M, Courdi A, Malaise EP, Experimental Data on the Radiobiology of Solid Tumors, *Eur. J. Radiother.*, **1**, 171-191, 1980.

Hahn EL, Spin Echoes, *Phys. Rev.*, **80**, 580-594, 1950.

Haus JW, Kehr, KW, Diffusion in Regular and Disordered Lattices, *Phys. Rep.*, **150**, 263-406, 1987.

Helmer KG, Dardzinski BJ, Sotak CH, Time-Dependent Diffusion in RIF-1 Tumors: *In Vivo* Extraction of Geometrical Parameters and Identification of Necrosis, *Second Meeting Society of Magn. Reson.*, San Francisco, CA, August, 1994.

Helmer KG, Dardzinski BJ, Sotak CH, The Application of Porous Media Theory to the Investigation of Time-Dependent Diffusion in *In Vivo* Systems, *NMR in Biomed.*, **8**, 297-306, 1995.

Helmer KG, Meiler M, Sotak CH, The Return-to-the-Origin Probability as an Indicator of Necrosis in RIF-1 Tumors, *Proc. ISMRM 5th Scientific Meeting*, Vancouver, p. 495, 1997.

Helmer KG, Meiler M, Hürlimann MD, Sotak CH, Experimental Determination of Finite Pulse Width Effects in Diffusion Coefficient Measurements, Abstract, 38th *ENC*, Orlando, FL, 1997.

Helmer KG, personal communication, 1999.

Hees PS, Sotak CH, Assessment of Changes in Murine Tumor Oxygenation in Response to Nicotinamide Using ^{19}F NMR Relaxometry of a Perfluorocarbon Emulsion, *Magn. Reson. Med.*, **29**, 303-310, 1993.

Horsman MR, Brown JM, Hirst VK, Lemmon MJ, Wood PJ, Dumphy EP, Overgaard J, Mechanism of Action of the Selective Tumor Radiosensitizer Nicotinamide, *Int. J. Radiat. Oncol. Biol. Phys.*, **15**, 685-690, 1988.

Houchens DP, Ovejera AA, The Nude Mouse in Oncology Research, Chapter 8,11, edited by Bowen E, Winogard B, CRC Press, Boca Raton, 1991.

Hürlimann MD, Helmer KG, DeSwiet TM, Sen PN, Sotak CH, Spin Echoes in a Constant Gradient and in the Presence of Simple Restrictions, *J. Magn. Reson. Ser. A*, **113**, 260-264, 1995.

Hyslop WB, Lauterbur PC, Effects of Restricted Diffusion on Microscopic NMR Imaging, *J. Magn. Reson.*, **94**, 501-510, 1991.

Jain RK, Transport of Molecules in the Tumor Interstitium: A Review, *Cancer Res.*, **47**, 3039-3051, 1987.

Jain RK, Determinants of Tumor Blood Flow: A Review, *Cancer Res.*, **48**, 2641-2658, 1988.

Jain RK, 1996 Whitaker Lecture: Delivery of Molecules, Particles, and Cells to Solid Tumors, *Annals of Biomed. Eng.*, **24**, 4457-4473, 1996.

Johnson DL, Plona TJ, Scala C, Pasierb F, Kojima H, Tortuosity and Acoustic Slow Waves, *Phys. Rev. Lett.*, **49**, 1840-1844, 1982.

Joseph PM, A Spin Echo Chemical Shift MR Imaging Technique, *J. Comput. Assist. Tomogr.*, **9**, 651-658, 1985a.

Joseph PM, Yuasa Y, Kundel HL, Mukherji B, Sloviter HA, Magnetic Resonance Imaging of Fluorine in Rats Infused with Artificial Blood, *Invest. Radiol.*, **20**, 504-509, 1985b.

Kamm YJL, Heerschap A, Rosenbusch G, Rietjens IMCM, Vervoort J, Wagner DJT, 5-Fluorouracil Metabolite Pattern in Viable and Necrotic Tumor Areas of Murine Colon Carcinoma Detected by ¹⁹F NMR Spectroscopy, *Magn. Reson. Med.*, **36**, 445-450, 1996.

Kim S-G, Ackerman JH, Quantitative Determination of Tumor Blood Flow and Perfusion via Deuterium Nuclear Magnetic Resonance Spectroscopy in Mice, *Cancer Res.*, **48**, 3449-3453, 1988.

Kärger J, Kocirik M, Zikanova A, Molecular Transport Through Assemblages of Microporous Particles, *J. Colloid and Interface Sci.*, **84**, 240-249, 1981.

Kärger J, Pfeifer H, Heink W, Principles and Application of Self-Diffusion Measurements by Nuclear Magnetic Resonance, *Adv. Magn. Reson.*, **12**, 1-89, 1988.

Latour LL, Li L, Sotak CH, Improved PFG Stimulated-Echo Method for the Measurement of Diffusion in Inhomogeneous Fields, *J. Magn. Reson. Ser. B*, **101**, 72-77, 1993a.

Latour LL, Mitra PP, Kleinberg RL, Sotak CH, Time-Dependent Diffusion Coefficient of Fluids in Porous Media as a Probe of Surface-to-Volume Ratio, *J. Magn. Reson. A*, **101**, 342-346, 1993b.

Latour LL, Svoboda K, Mitra PP, Sotak CH, Time-Dependent Diffusion of Water in Biological Model System, *Proc. Natl. Acad. Sci. USA*, **91**, 1229-1233, 1994.

Lauterbur PC, Image Formation by Induced Local Interactions: Examples Employing Nuclear Magnetic Resonance, *Nature*, **242**, 190-191, 1973.

Le D, Mason RP, Hunjan S, Constantinescu, A, Barker BR, Antich PP, Regional Tumor Oxygen Dynamics: ^{19}F PBSR EPI of Hexafluorobenzene, *Magn. Reson. Imag.*, **15**, 971-981, 1997.

LeBihan D, Turner R, Moonen CTW, Pekar J, Imaging of Diffusion and Microcirculation with Gradient Sensitization: Design, Strategy, and Significance, *J. Magn. Reson. Imag.*, **1**, 7-28, 1991.

Less JR, Skalak TC, Sevick EM, Jain RK, Microvascular Architecture in a Mammary Carcinoma: Branching Patterns and Vessel Dimensions, *Cancer Res.*, **51**, 265-273, 1991.

Li, S, Wehrle JP, Glickson JD, Kumar N, Braunschweiger PG, Tumor Bioenergetics and Blood Flow in RIF-1 Murine Tumors Treated with 5-Fluorouracil, *Magn. Reson. Med.*, **22**, 47-56, 1991.

Longmaid HA, Adams DF, Neirincks RD, Harrison CG, Brunner P, Seltzer SE, Davis MA, Neuringer L, Geyer RP, *In Vivo* ^{19}F Imaging of the Liver, Tumor, and Abscess in Rats: Preliminary Results, *Invest. Radiol.*, **20**, 141-145, 1985.

Mansfield P, Grannell PK, "Diffraction" and Microscopy in Solids and Liquids by NMR, *Phys. Rev. B*, **12**, 3618, 1975.

Mansfield P, Multi-Planar Image Formation Using NMR Spin Echoes, *J. Chem. Phys. C. Solid State Phys.*, **10**, L55-58, 1977.

Mason RP, Antich PP, Babcock EE, Gerberich JL, Nunnally RL, Perfluorocarbon Imaging *In Vivo*: A ^{19}F MRI Study in Tumor-Bearing Mice, *Magn. Reson. Imag.*, **7**, 475-485, 1989.

Mason RP, Nunnally RL, Antich PP, Tissue Oxygenation: A Novel Determination Using ^{19}F Surface Coil NMR Spectroscopy of Sequestered Perfluorocarbon Emulsion, *Magn. Reson. Med.*, **18**, 71-79, 1991.

Mason RP, Rodbumrung W, Antich PP, Hexafluorobenzene: A Sensitive ^{19}F NMR Indicator of Tumor Oxygenation, *NMR Biomed.*, **9**, 125-134, 1996.

McFarland E, Koutcher HA, Rosen BR, Teicher B, Brady TJ, *In Vivo* ^{19}F NMR Imaging, *J. Comput. Assist. Tomogr.*, **9**, 8-15, 1985.

Meiler M, Helmer KG, Sotak CH, Return-to-the-Origin Probability Imaging as Indicator of Local Necrosis, *Proc. IEEE 24th Annual Northeastern Bioengineering Conference*, Hershey, PA, p. 72, 1998.

Mitra PP, Sen PN, Schwartz LM, Le Doussal P, Diffusion Propagator as a Probe of the Structure of Porous Media, *Phys. Rev. Lett.*, **68**, 3555-3558, 1992.

Mitra PP, Sen PN, Schwartz LM, Le Doussal P, Short-time Behavior of the Diffusion Coefficient as a Geometrical Probe of Porous Media, *Phys. Rev. Lett.*, **68**, 3555-3558, 1992.

Mitra PP, Halperin BI, Effects of Finite Gradient-Pulse Widths in Pulsed-Field-Gradient Diffusion Measurements, *J. Magn Reson. Ser. A*, **113**, 94-101, 1995a.

Mitra PP, Latour LL, Kleinberg RL, Sotak CH, Pulsed-Filed Gradient NMR Measurements of Restricted Diffusion and the Return-to-the-Origin Probability, *J. Magn. Reson.*, **114**, 47-58, 1995b.

Morris PG, Nuclear Magnetic Resonance Imaging in Medicine and Biology, 1st ed., Oxford University Press, Oxford, 1986.

Moseley ME, Cohen Y, Mintorovitch J, Chileuitt L, Shimizu H, Kucharczyk J, Wendland MF, Weinstein PR, Early Detection of Regional Cerebral Ischemia in Cats: Comparison of Diffusion and T_2 -Weighted MRI and Spectroscopy, *Magn. Reson. Med.*, **14**, 330-346, 1990.

Moulder JE, Rockwell S, Hypoxic Fractions of Solid Tumor: Experimental Techniques, Methods of Analysis, and a Survey of Existing Data, *Int. J. Radiat. Oncol. Biol. Phys.*, **10**, 695-712, 1984.

Murday JS, Cotts RM, Self-Diffusion Coefficient of Liquid Lithium, *J. Chem. Phys.*, **48**, 4938-4945, 1968.

Neuman CH, Spin Echo of Spins Diffusing in a Bounded Medium, *J. Chem. Phys.*, **60**, 4508-4511, 1974.

Ng TC, Evanochko WT, Hiramoto RN, ^{31}P NMR Spectroscopy of *In Vivo* Tumors, *J. Magn. Reson.*, **49**, 271-286, 1982.

Nicholson C, Rice ME, Diffusion of Ions and Transmitters in the Brain Cell Microenvironment, In: Volume Transmissions in the Brain: Novel Mechanisms for Neural Transmission, edited by Fuxe K, Agnati LF, Raven Press Ltd., New York, 1991.

Olive PL, Durand RE, Fluorescent Nitroheterocycles for Identifying Hypoxic Cells, *Cancer Res.*, **43**, 3276-3280, 1983.

Olive PL, Viske C, Martin AA, Trotter J, Measurement of Oxygen Diffusion Distance in Tumor Cubes Using a Fluorescent Hypoxia Probe, *Int. J. Radiat. Oncol. Biol. Phys.*, **22**, 3997-4002, 1992.

Patan S, Munn LL, Jain RK, Intussusceptive Microvascular Growth in Solid Tumors: A Novel Mechanism of Tumor Angiogenesis, *Microvasc. Res.*, **51**, 260-272, 1996.

Price SW, Kuchel PW, Effects of Nonrectangular Field Gradient Pulses in the Stejskal and Tanner (Diffusion) Pulse Sequence, *J. Magn. Reson.*, **94**, 133-139, 1991.

Purcell EM, Torrey HC, Pound RV, Resonance Absorption by Nuclear Magnetic Moments in a Solid, *Phys. Rev.* **69**, 37-38, 1946.

Pütz B, Barsky D, Schulten K, Edge Enhancement by Diffusion in Microscopic Magnetic Resonance Imaging, *J. Magn. Reson.*, **97**, 27-53, 1992.

Ratner AV, Sotak CH, Muller H, Hurd R, Young SW, ^{19}F Magnetic Resonance Imaging of the Reticuloendothelial System, *Magn. Reson. Med.*, **5**, 548-554, 1987.

Ratner AV, Muller HH, Simpson BB, Johnson DE, Hurd R, Sotak CH, Young SW, Detection of Tumors with ^{19}F Magnetic Resonance Imaging, *Invest. Radiol.*, **23**, 361-364, 1988.

Robertson B, Spin-Echo Decay of Spins Diffusing in a Bounded Region, *Phys. Rev.*, **151**, 273-277, 1966.

Rockwell S, Use of a Perfluorochemical Emulsion to Improve Oxygenation in Solid Tumor, *Int. J. Radiat. Oncol. Biol. Phys.*, **11**, 97-103, 1985.

Rockwell S, Mate TP, Irvin C, Nierenburg M, Reactions of Tumors and Normal Tissue in Mice to Irradiation in the Presence and Absence of Perfluorochemical Emulsion, *Int. J. Radiat. Oncol. Biol. Phys.*, **12**, 1315-1318, 1986.

Salib N, Brown MA, Clinical MR Spectroscopy First Principles, 1st ed. New York, Wiley-Liss, 1998.

Shackney SE, McCormack GW, Cuchural GJ, Growth Rate Patterns of Solid Tumors and their Relation to Responsiveness to Therapy, *Ann. Intern. Med.*, **89**, 107-121, 1978.

Sijens PE, Baldwin NJ, Ng TC, Multinuclear MR Investigation of Metabolic Response of the Murine RIF-1 Tumor to 5-Fluorouracil Chemotherapy, *Magn. Reson. Med.*, **19**, 373-385, 1991.

Smith RC, Lange RC, Understanding Magnetic Resonance Imaging, 1st ed., Boca Raton, CRC Press, 1998.

Song WS, Zhang WL, Pence DM, Lee I, Levitt SH, Increased Radiosensitivity of Tumors by Perfluorochemicals and Carbogen, *Int. J. Radiat. Oncol. Biol. Phys.*, **11**, 1833-1836, 1985.

Sotak CH, Dardzinski BJ, Hees PS, Kaufman RJ, Study of Biodistribution and Dose Response of Perfluoro-15-Crown-5-Ether in Tumor-Bearing C3H Mice Using ¹⁹F Magnetic Resonance Imaging, *Proc. SMRM 12th Annual Meeting*, New York, NY, p. 983, 1993a.

Sotak CH, Hees PS, Huang HN, Hung MH, Krespan CG, Raynolds S, A New Perfluorocarbon for Use in Fluorine-19 Magnetic Resonance Imaging and Spectroscopy, *Magn. Reson. Med.*, **29**, 188-195, 1993b.

Sotak CH, Dardzinski BJ, Kaufman RJ, Characterization of Perfluoro-15-Crown-5-Ether for Use in ¹⁹F Magnetic Resonance Imaging and Spectroscopy, *Proc. SMRM 12th Annual Meeting*, New York, NY, p. 243, 1993c.

Sotak CH, Hees PS, Huang HN, Hung MH, Krespan CG, Raynolds S, Use of PTBD for Murine Tumor Detection with ^{19}F MR Imaging on a 1.5 T Clinical Instrument, *J. Magn. Reson. Imag.*, **1**,163, 1991.

Spang-Thomson M, Nielsen A, Visfeldt, Growth Curves of Three Human Malignant Tumors Transplanted to Nude Mice, *Expl. Cell Biol.*, **48**, 138-154, 1980.

Steen RG, Response of Solid Tumors to Chemotherapy Monitored in Vivo ^{31}P Nuclear Magnetic Resonance Spectroscopy: A Review, *Cancer Res.*, **49**, 4075-4085, 1989.

Stejskal EO, Use of Spin Echoes in a Pulsed Magnetic-Field Gradient to Study Anisotropic Restricted Diffusion and Flow, *J. Chem. Phys.*, **43**, 3597-3603, 1965.

Stejskal EO, Tanner JE, Spin Diffusion Measurements: Spin Echoes in the Presence of Time-Dependent Field Gradient, *J. Chem. Phys.*, **42**, 288-292, 1965.

Stoller SD, Happer W, Dyson FJ, Transverse Spin Relaxation in Inhomogeneous Magnetic Fields, *Phys. Rev. A*, **44**, 7459-7477, 1991.

Swiet TM, Sen PN, Decay of Nuclear Magnetization by Bounded Diffusion in a Constant Field Gradient, *J. Chem. Phys.*, **100**, 5597-5604, 1994.

Tanner JE, Use of the Stimulated Echo in NMR Diffusion Studies, *J. Chem. Phys.*, **52**, 2523-2526, 1970.

Tanner JE, Stejskal EO, Restricted Self-Diffusion of Protons in Colloidal Systems by the Pulsed-Gradient, Spin-Echo Method, *J. Chem. Phys.*, **49**, 1768-1777, 1968.

Tanner JE, Stejskal EO, Transient Diffusion in a System Partitioned by Permeable Barriers. Application to NMR Measurements with Pulsed-Field Gradient, *J. Chem. Phys.*, **69**, 1748-1754, 1978.

Thomas SR, Clark LC, Ackerman JL, Pratt RG, Hoffman RE, Busse LJ, Kinsey RA, Samaratinga RC, MR Imaging of Lung Using Liquid Perfluorocarbons, *J. Comp. Assist. Tomogr.*, **10**, 1-9, 1986.

Thomlinson RH, Gray LH, The Histological Structure of Some Human Lung Cancers and the Possible Implications for Radiotherapy, *Brit. J. Cancer*, **9**, 539-549, 1955.

Tomayko MM, Reynolds CP, Determination of Subcutaneous Tumor Size in Athymic (Nude) Mice, *Cancer Chemother. Pharmacol.*, **24**, 148-154, 1989.

Torres-Filho IP, Leuning M, Yuan F, Intaglietta M, Jain RK, Noninvasive Measurement of Microvascular and Interstitial Oxygen Profiles in a Human Tumor in SCID Mice, *Proc. Natl. Acad. Sci. USA*, **91**, 2081-2085, 1994.

Torrey HC, Bloch Equations with Diffusion Terms, *Phys. Rev.*, **104**, 563-565, 1956.

Twentyman PR, Brown JM, Gray JW, Franko AJ, Scoles MA, Kallman RF, A New Mouse Tumor Model System (RIF-1) for Comparison of End-Point Studies, *JNCI*, **64**, 595-604, 1980.

Vaupel P, Hypoxia in Neoplastic Tissue, *Microvas. Res.*, **13**, 399-408, 1977.

Wang LZ, Caprihan A, Fukushima E, The Narrow-Pulse Criterion for Pulsed-Gradient Spin-Echo Diffusion Measurements, *J. Magn. Reson. Ser. A*, **117**, 209-219, 1995.

Wayne RC, Cotts RM, Nuclear-Magnetic-Resonance Study of Self-Diffusion in a Bounded Medium, *Phys. Rev.*, **151**, 264-272, 1966.

Woessner DE, NMR Spin-Echo Self-Diffusion Measurements on Fluids Undergoing Restricted Diffusion, *J. Chem. Phys.*, **67**, 1365-1367, 1963.

Wyllie AH, Kerr JFR, Currie AR, Cell Death: The Significance of Apoptosis, *International Review of Cytology*, **68**, 251-306, 1980.

Wyllie AH, Cell Death: A New Classification Separating Apoptosis from Necrosis, in *Cell Death in Biology and Pathology*, ed. by Bowen ID and Lockshin RA, Chapman and Hall, New York, 9-34, 1981.

Zhao M, Pipe JG, Evelhoch JL, Early Detection of Treatment Response by Diffusion-Weighted H-NMR Spectroscopy in a Murine Tumor *In Vivo*, *Brit. J. Cancer*, **73**, 61-64, 1995.

Zhao M, Pipe JG, Bonnett J, Evelhoch JL, Early Detection of Response to Cyclophosphamide Chemotherapy by Diffusion Weighted ¹H NMR Spectroscopy in Murine RIF-1 Tumors *in Vivo*, *Proc. ISMRM 4th Scientific Meeting*, New York, NY, p. 1333, 1996a.

Zhao M, Evelhoch JL, Detection of Response to 5-Fluorouracil by Diffusion-Weighted H-NMR Spectroscopy in Murine Tumors *In Vivo*, *Proc. ISMRM 4th Scientific Meeting*, New York, NY, p. 1118, 1996b.

Zientara GP, Freed JH, Spin-Echoes for Diffusion in Bounded, Heterogeneous Media: A Numerical Study, *J. Chem. Phys.*, **72**, 1285-1292, 1985.

Appendix

9.0 Curriculum Vitae

Michael Meiler

Biomedical Engineering Department
Worcester Polytechnic Institute
100 Institute Road
Worcester, MA 01609
Ph: (508) 831 - 5676
Fax: (508) 831 - 5441
meiler@wpi.edu

6 Berkshire Street #3
Worcester, MA 01609
Ph: (508) 753 - 2490

Education

Worcester Polytechnic Institute, Worcester, MA

- Ph.D. biomedical Engineering 1999

Worcester Polytechnic Institute, Worcester, MA

- M.E. Biomedical Engineering 1996

German Air Defense School, El Paso, TX 1992

Universität der Bundeswehr München

- Dipl. Ing. univ. Electrical Engineering 1991

German Air Force Academy, Fürstenfeldbruck, Bavaria 1987

Experience

Research Assistant, Worcester Polytechnic Institute, Biomedical Engineering Department, Worcester, MA. January 1996 - present. Measurement of the apparent diffusion coefficient and the return-to-the-origin probability in tumors to differentiate between necrotic and viable tissue. Conducted ^{19}F measurements of intravenously administered perfluorocarbon to measure oxygen tension in murine tumors. Design of nuclear magnetic resonance (NMR) spectroscopy and imaging experiments as well as NMR pulse sequences. Data analysis and custom coding of data analysis software in C and IDL (Interactive Data Language). Construction of NMR RF coils (Solenoid, Surface, Birdcage, Saddle, Double-tuned, double coil) with and without shields for different applications. Design and construction of biomedical instrumentation and brain electrodes to measure physiological signals generated by spreading depression waves in rat brain. Tumor inoculation, drug preparation and administration. NMR system maintenance and cryogen fills.

System Administrator, Worcester Polytechnic Institute Biomedical Engineering Department, NMR Research Group, Worcester, MA, August 1995 - present. Responsible for maintenance of PC's, computer software and hardware. Installation and maintenance of network.

Teaching Assistant, Worcester Polytechnic Institute, Biomedical Engineering Department, Worcester, MA. Spring Semester. Responsible for laboratory classes and animal care in small animal surgery. Assisting students during in-class surgery.

Martial Arts Instructor, Volkshochschule Landshut, Landshut, Germany 1994. Teaching of weaponless self defense.

Tactical Control Officer, German Air Force, 1992 - 1995. Combat team leader of NATO assigned surface-to-air missile air defense unit. Responsible for deployment, tactic, security and training.

Intern, Heiden Electronics München, July 1989. Responsible for prototyping, technical documentation, design and preparation for serial production.

Intern, German Telekom, München, July 1988 - August 1988. Planning and implementation of radio telecommunication links, mobile phone systems and equipment.

**Awards
and Recognitions**

Reward for extraordinary duty 1991, German Air Force.

**Professional
Association**

International Society for Magnetic Resonance in Medicine

**Extra Curricular
Activities**

Student representative in faculty committee 1988-1990. Representing the interests of students in faculty related policies such as curriculum, grading procedures and employment. Creation of new curriculum for EE.

Student Council 1988-1990. Representing the interests of EE students at University.

Subcommittee for education 1988-1990. Representing the interests of EE students in the design of a new curriculum.

Chairman for Public Relations, 1985-1986, Soccer Club, Blau-Weiß Freiburg 1911 e.V., Freiburg, Germany.

Soccer Coach, 1984-1986, Blau-Weiß Freiburg 1911 e.V., Freiburg, Germany.

Assistant Soccer Coach, 1983-1984, Blau-Weiß Freiburg 1911 e.V., Freiburg, Germany.

Referee, German Soccer Association (DFB) 1983-1986

Special Skills

Programming Skills: Fortran, Basic, Pascal, C, Assembler Code (Intel 80x86), IDL (Interactive Data Language), APPL (Advanced Pulse Programming Language) , PSpice.

Computer Systems: Hewlett Packard HP-UX, Silicon Graphics IRIX, Apple Macintosh, MS-DOS and Windows.

Languages: German (fluent), English (fluent), French (School knowledge), Spanish (intermediate)

- Personal Interests** Traveling
 Martial Arts (Jiu Jitsu, Bo Jitsu)
 Scuba Diving (SSI Dive Control Specialist)
 Soccer
- Publications** Takano, K., Carano, R., Tatlisumak, T., Meiler, M., Sotak, C. H., Kleiner, H., Fisher, M., The Efficacy of Intra-Arterial and Intravenous Pro-Urokinase in an Embolic Stroke Model Evaluated by Diffusion-Perfusion Magnetic Resonance Imaging, *Neurology*, **50**, 870-875, 1998.
- Tatlisumak, T., Takano, K., Meiler, M., Fisher, M., A Glycine Antagonist, ZD9379, Reduces Infarct Size and Number of Spreading Depressions in Rats with Middle Cerebral Artery Occlusion, *Stroke*, **29**, 190-195, 1998.
- Presentations** "Experimental Determination of Finite Pulse Width Effects in Diffusion Coefficient Measurements," Karl G. Helmer, Michael Meiler, Martin D. Hürlimann, and Christopher H. Sotak, Abstract, Poster Presented at the 38th Experimental NMR Spectroscopy Conference, Orlando, Florida, March, 1997.
- "The Return-to-the-Origin Probability as an Indicator of Necrosis in RIF-1 Tumors," K. G. Helmer, M. Meiler, and C. H. Sotak, Abstract, Oral Presentation at the Fifth Scientific Meeting of the International Society of Magnetic Resonance in Medicine, Vancouver, British Columbia, Canada, April, 1997; also published in *Proc. Int. Soc. Magn. Reson. Med.* **1**, 494 (1997).
- "Evaluating Anti-Ischemic Effects of Non-Selective Cation Channel Blocker, LOE 908 MS, by Diffusion and Perfusion MRI With Post Mortem Analysis," R. A. D. Carano, K. Takano, M. R. Meiler, T. Tatlisumak, K. G. Helmer, U. Pschorn, M. Fisher, and C. H. Sotak, Abstract, Oral Presentation at the Fifth Scientific Meeting of the International Society of Magnetic Resonance in Medicine, Vancouver, British Columbia, Canada, April, 1997; also published in *Proc. Int. Soc. Magn. Reson. Med.* **1**, 400 (1997).
- "The Efficacy of Intra-arterial and Intravenous Pro-urokinase in an Embolic Stroke Model," Kentaro Takano, Richard A. D. Carano, Turgut Tatlisumak, Michael Meiler, Christopher H. Sotak, Hollis D. Kleinert, and Marc Fisher, Abstract, Poster Presented at the 49th Annual Meeting of the American Academy of Neurology, Boston, Massachusetts, April, 1997; also published in *Neurology* **48**, A408 (1997).
- "Glycine Site Antagonism Reduces Number of Spreading Depressions and Infarct Size in Rats," T. Tatlisumak, K. Takano, M. Meiler and M. Fisher, Abstract, Poster Presented at the 23rd International Joint Conference on Stroke and Cerebral Circulation, Orlando, Florida, February, 1998; also published in *Stroke* **29**, 331 (1998).
- "Return-to-the-Origin Probability Imaging as Indicator of Local Necrosis," M. Meiler, K. G. Helmer, C. H. Sotak, Abstract, Oral Presentation at the IEEE 24th Northeastern Bioengineering Conference, Hershey, Pennsylvania, April, 1998; also published in *Proc. IEEE 24th Northeastern Bioeng. Conf.*, 72-73 (1998).

"The Use of pO_2 and Diffusion Measurements For Characterizing Treatment Response in RIF-1 Tumors," K. G. Helmer, S. Han, M. Meiler, and C. H. Sotak, Syllabus, Oral Presentation at the Workshop on Magnetic Resonance in Experimental and Clinical Cancer Research, St. Louis, Missouri, November, 1998.

"Return-to-the-Origin Probability and ADC Mapping as Indicators of Efficacy of Chemotherapy in RIF-1 Tumors," M. R. Meiler, K. G. Helmer, C. H. Sotak, Abstract, Poster Presented at the Seventh Scientific Meeting of the International Society of Magnetic Resonance in Medicine, Philadelphia, Pennsylvania, May, 1999; also published in *Proc. Int. Soc. Magn. Reson. Med.* **2**, 1378 (1999).

"Comparison of the Return-to-the-Origin Probability and Apparent Diffusion Coefficient of Water to Map Murine Tumor Necrosis," M. R. Meiler, K. G. Helmer, C. H. Sotak, Abstract, Poster Presented at the Seventh Scientific Meeting of the International Society of Magnetic Resonance in Medicine, Philadelphia, Pennsylvania, May, 1999; also published in *Proc. Int. Soc. Magn. Reson. Med.* **2**, 1379 (1999).